Hierarchical Macroporous Polymers: Synthesis and Characterisation

Ling Ching Wong

A dissertation submitted to Imperial College London
for the degree of
Doctor of Philosophy

Department of Chemical Engineering
Imperial College London
South Kensington Campus
SW7 2AZ
London UK

2013

Declaration

Except where explicitly stated, this dissertation is a description of my own work, carried out under the supervision of Professor Alexander Bismarck in the Department of Chemical Engineering, Imperial College London. The material presented herewith is original and has not been submitted for a degree at this or any other university.

Ling Ching Wong

Abstract

This thesis describes the production of two types of hierarchical macroporous polymers using the emulsion templating technique. The first are those with a **hierarchy of macroporous**, defined as the efficient packing of pores with multi-modal pore size distributions. The second are macroporous polymers containing a **hierarchical particulate network,** defined by an interconnected particle network within the polymer matrix.

In the first section of the thesis, macroporous hierarchy was achieved using 3 different methods. In the first method, the properties of surfactant stabilised high internal phase emulsion (HIPE) were optimised by varying selected emulsification parameters such as the surfactant concentration and stirring rate. The Finite Element Method (FEM) was subsequently used to qualitatively compare and validate the effect of pore hierarchy on the Young's modulus of macroporous polymers. It was believed that the hierarchical arrangement of macropores facilitated the load transfer during compression, which improved its mechanical properties.

The second method involved the use of a mixed surfactant and particle emulsifier system to prepare w/o HIPEs. The mixture of surfactants and particles in the emulsion produced synergistic effects which resulted in a hierarchical macroporous arrangement after polymerisation. The hierarchical porous materials prepared using this method showed high gas permeabilities while maintaining high crush strengths and Young's moduli compared to 'conventional' poly(merised)HIPEs. The improvement in mechanical strength despite the high interconnectivity was attributed to the efficient packing of macropores in a hierarchical configuration.

The third approach was to mechanically-froth viscous air in w/o emulsion templates. A bio-based monomer, acrylated epoxidised soyabean oil (AESO) was chosen as a component of the continuous phase of the emulsion for its high viscosity and ability to trap air bubbles during mechanical frothing. Medium Internal Phase Emulsions (MIPEs) containing varying concentrations of AESO were mechanically frothed to incorporate air bubbles, prior to polymerisation. This was found to generate a multi-modal distribution of droplets and air bubbles which polymerised into hierarchical foams with high porosities of up to 81%.

In the second section of the thesis, a hierarchical particulate network within the polymer matrix of a porous material was produced using Pickering HIPEs stabilised by varying the concentrations of thermally reduced graphene oxide (rGO) flakes. Macroporous nanocomposites containing 0.006 vol.% of rGO had a conductivity of $1.2\ 10^{-5}\ Sm^{-1}$, demonstrating the presence of an interconnected, conducting rGO network within the polymer matrix. The rGO-network created an additional level of hierarchy in these macroporous materials which also improved the overall mechanical properties (viscoelastic properties, Young's modulus and crush strength).

Table of Contents

Abstract 3
Table of Contents 5
Acknowledgements 8
List of Publications 10
Oral Presentations at Conferences 11
Poster Presentations at Conferences 14
Awards 15
List of Figures 16
List of Tables 21
1 Introduction 22
1.1 Motivations and Objectives of This Project 25
1.2 Structure of This Thesis 26
2 Background 28
2.1 Introduction to Emulsions 28
2.2 The Emulsification Process 29
2.3 Classification of Emulsions 32
2.3.1 Continuous Phase 32
2.3.2 Internal Phase Volume Ratio 34
2.4 Emulsifiers 37
2.4.1 Surfactants 37
2.4.2 Particles 44
2.4.3 Combining Surfactants and Particles 53
2.5 Introduction to Emulsion Templating 56
2.5.1 Polymerised High Internal Phase Emulsions (PolyHIPEs) 56
2.5.2 Polymerised-Pickering HIPEs (Poly-Pickering HIPEs) 59
2.5.3 Hierarchical PolyHIPEs 62
3 Hierarchical Polymerised High Internal Phase Emulsions Synthesised from Surfactant-Stabilised Emulsion Templates 65
3.1 Summary 65
3.2 Introduction 66
3.3 Experimental 69
3.3.1 Materials 69
3.3.2 HIPE Preparation 69

3.3.3 PolyHIPE Preparation 70
3.3.4 Characterisation of PolyHIPEs 70
3.3.5 Simulated Porous Microstructures and Determination of Young's Modulus Using Finite Element Method (FEM) 74
3.4 Results and Discussion 75
3.5 Conclusions 92
4 Macroporous Polymers with Hierarchical Pore Structure from Emulsion Templates Stabilised by Both Particles and Surfactants 93
4.1 Summary 93
4.2 Introduction 94
4.3 Experimental 96
4.3.1 Preparation of HIPEs and PolyHIPEs 96
4.3.2 Characterisation of PolyHIPEs 96
4.4 Results and Discussion 97
4.5 Conclusions 105
5 Air in Water-in-oil Emulsion Templates: Developing Highly Porous Greener Hierarchical Macroporous Nanocomposite Foams 107
5.1 Summary 107
5.2 Introduction 108
5.3 Experimental 111
5.3.1 Materials 111
5.3.2 Preparation of Polymer Foams Using Emulsion Templates 111
5.3.3 Preparation of Polymer Foams by Mechanically Frothing Emulsion Templates from 5.3.2 112
5.3.4 Characterisation of Polymer Foams 113
5.4 Results and Discussion 114
5.5 Conclusions 125
6 Nanocomposite Macroporous Polymers and Beads Synthesised from Emulsion Templates Stabilised by Chemically Modified Graphene 126
6.1 Summary 126
6.2 Introduction 127
6.3 Experimental 130
6.3.1 Processing of Chemically Modified Graphene (CMG) Flakes 130
6.3.2 Preparation of Nanocomposites Beads and Macroporous Polymers 131
6.3.3 Characterisation of Nanocomposite Beads and Macroporous Polymers 133

6.4 Results and Discussion 134
6.5 Conclusions 147
7 Conclusions and Suggestions for Future Work 149
7.1 Summary of Findings 149
7.1.1 Hierarchical PolyHIPEs Synthesised from Surfactant-Stabilised Emulsion Templates 149
7.1.2 Macroporous Polymers with Hierarchical Pore Structure from Emulsion Templates Stabilised by Both Particles and Surfactants 150
7.1.3 Air in Water-in-oil Emulsion Templates: Developing Highly Porous Greener Hierarchical Macroporous Nanocomposite Foams 151
7.1.4 Nanocomposite Macroporous Polymers and Beads Synthesised from Emulsion Templates Stabilised by Chemically Modified Graphene 152
7.2 Future work 153
7.2.1 Optimising Hierarchical PolyHIPEs Synthesised from Surfactant-Stabilised Emulsion Templates 153
7.2.2 Further Characterisation of Hierarchical Macroporous Polymers from Emulsion Templates Stabilised by Particles and Surfactants 154
7.2.3 Developing Highly Porous Hierarchical Macroporous Nanocomposites by Mechanically Frothing Viscous Emulsions 155
7.2.4 Graphene Oxide Hierarchical Macroporous Nanocomposites 156
Bibliography 157
Appendices 169

Acknowledgements

I would first like to express my gratitude and appreciation to my supervisor Professor Alexander Bismarck for the guidance he has provided throughout my PhD. His enthusiasm and zany approach to science has shaped my own attitude to research. I am also deeply appreciative to Dr Angelika Menner who has been a mentor to me, providing incredible insight and advice at every step of my PhD.

I would like to thank the UK Engineering and Physical Science Research Council's (EPSRC) contribution to the Challenging Engineering Award for funding this project (EP/E007538/1) and the Rector's Award of Imperial College London for providing my scholarship.

I would also like to acknowledge and thank the following collaborators for their contributions and fulfilling discussions:

Dr Pedro Baiz Villafranca (Department of Aeronautics, Imperial College London), for generating the 2D porous geometries and developing the FEM code used in the simulation study in Chapter 3.

Dr Alejandro Vílchez Villalba (Institut de Química Avançada de Catalunya, Barcelona, Spain) for facilitating the preparation of thin sections for TEM presented in Chapter 4.

Dr Suelen Barg (Centre for Advanced Structural Ceramics, Department of Materials, Imperial College London) for providing the graphene oxide used to prepare the nanocomposites and for assisting in the measurement of conductivity of the nanocomposite macroporous foams described in Chapter 6.

My PhD would not have been as enjoyable without the helping hands from my colleagues and friends from the charismatic Polymers and Composites Engineering (PaCE) group, past and present, many of whom have also put in effort to edit this thesis. In particular Dr Vivian Ikem, who passed her knowledge of poly-Pickering HIPEs to me; Dr Koon-yang Lee, for great brainstorming sessions and who also measured the viscoelastic properties of the bio-based foams in Chapter 5; Thanks also to Dr John Hodgkinson for his wisdom and insightful take on the mechanical properties of my materials; Office and lab mates Nadine Graeber, John Jiang, Dr Edyta Lam, Dr Dan Cegla, Dr Jonny Blaker, Dr Anthony Abbott, Bernice Oh, Jing Li, Hele Diao and Michael Tebboth, for their amusing antics which have created many fond memories for me; Dr Siti Rosminah Shamsuddin, for her invaluable friendship and kindness. My gratefulness also extends to Dr George Duo Wang from the Surfaces and Particle Engineering Lab for his insight on various colloid characterisation techniques.

I would like to thank the staff from the Department of Chemical Engineering, especially Susi Underwood, who has been a constant source of support from the early beginnings of my PhD. Thanks also to Patricia Carry, Sarah Payne, Nam Ly, Keith Walker, Ben Kristnah, Richard Wallington and Severine Toson, all who have helped me in one way or another. Not forgetting Dr Mahmoud Akandi from the Department of Materials and Dr Ruth Brooker from the Department of Mechanical Engineering who helped me conquer the challenges associated with SEM and TEM.

Lastly, I would like to express my greatest appreciation to Mum and Dad, for always encouraging me to strive for the best and for bringing me up to know the value of hard work and perseverance. I would also like to thank Cumarran, for supporting me throughout this journey.

List of Publications

Wong, L.L.C., Ikem, V.O., Menner, A., Bismarck, A., "Macroporous Polymers with Hierarchical Pore Structure from Emulsion Templates Stabilised by Both Particles and Surfactants", Macromolecular Rapid Communication, **2011**, 32 (19), pp 1563-1568

Lee, K.Y., Wong, L.L.C., Blaker, J.J., Hodgkinson, J., Bismarck, A., "Air templated Bio-based Macroporous Polymer Nanocomposites" Green Chemistry. **2011**, 13, pp 3117-3123.

Wong, L.L.C., Menner, A., Baiz, P., Bismarck, A., "Hierarchical Open Porous PolyHIPEs Synthesised from Surfactant Stabilised Emulsion Templates" Langmuir, **2013**, 29 (20), pp 5052-5961.

Wong, L.L.C., Barg, S., Pereira, P., Menner, A., Goki, E., Chowalla, M., Bismarck, A., Saiz, E., "Nanocomposite Macroporous Polymers and Beads Synthesised from Emulsion Templates Stabilised by Chemically Modified Graphene" **2013** *Manuscript Submitted*

Wong, L.L.C., Lee, K.Y., Menner, A., Bismarck, A., "Mechanically Frothed Water-in-Oil Emulsion Templates: Developing Highly Porous Bio-based Hierarchical Macroporous Nanocomposite Foams" **2013** *Manuscript Submitted*

Oral Presentations at Conferences

Wong, L.L.C., Barg, S., Saiz, E., Menner, A., Bismarck, A., "Graphene Oxide Macroporous Polmyer Foam Nanocomposites Synthesised via Emulsion Templating", 245th ACS National Meeting, 7th – 11th April 2013, New Orleans, Louisiana, USA.

Wong, L.L.C., Menner, A., Bismarck, A., "Creating Highly Porous Gradient Polymer Nanocomposites by Layering Emulsion Templates", 245th ACS National Meeting, 7th – 11th April 2013, New Orleans, Louisiana, USA.

Wong, L.L.C., Barg, S., Saiz, E., Menner, A., Bismarck, A., "Towards Conductive Macroporous Polymer Foams Synthesised via Graphene Oxide Stabilised Emulsion Templates for Biological Applications", 6th International Conference on Bioengineering and Nanotechnology (ICBN), 24th – 27th June 2012, Berkeley, California, USA.

Wong, L.L.C., Menner, A., Bismarck, A., "Porous Materials: Synthesis and Application in Industry", British Federation for Women Graduates Research Presentations Day, 19th May 2012, London, United Kingdom.

Wong, L.L.C., Menner, A., Bismarck, A., "Hierarchical Polymer Foams Synthesised by Emulsion Templating", Imperial College Chemical Engineering PhD Symposium, 30th March 2012, London, United Kingdom.

Lee, K.Y., Wong, L.L.C, Blaker, J.J., Hodgkinson, J.M., Bismarck, A., "Air-Templated Nanocellulose Reinforced Macroporous Foams", AIChE Annual Meeting, 16th – 21st October 2011, Minneapolis, Minnesota, USA.

Wong, L.L.C, Lee, K.Y., Menner, A., Bismarck, A., "Mechanically Frothing High Internal Phase Emulsions: Developing Hierarchical Macroporous Nanocomposites the Green Way", 19th Annual BioEnvironmental Polymers Society (BEPS) Meeting, 28th – 30th September 2011, Vienna, Austria.

Wong, L.L.C., Bismarck, A., "Emulsion Templated Porous Materials", Electrochemical Array Printing Workshop, 26th August 2011, Paris, France.

Graeber, N., Lee, K.Y., Wong, L.L.C., Menner, A., Bismarck, A., "Renewable Open Macroporous Nanocomposites via Emulsion Templating", International Conference on Materials for Advanced Technologies (ICMAT), 26th June – 1st July 2011, Singapore.

Wong, L.L.C., Ikem, V.O., Menner, A., Bismarck, A., "Hierarchical Macroporous Polymers Synthesised from Nanoparticle and Surfactant Stabilised Emulsion Templates", International Conference on Materials for Advanced Technologies (ICMAT), 26th June – 1st July 2011, Singapore.

Wong, L.L.C., Menner, A., Bismarck, A., "Hierarchical Macroporous Polymers via Emulsion Templating", 241st ACS National Meeting and Exposition, 27th – 31st March 2011, Anaheim, California, USA.

Wong, L.L.C., Barg, S., Saiz, E., Chowalla, M., Menner, A., "Graphene Oxide-Polymer Composites via Emulsion Polymerization" Materials Research Society (MRS) Fall Meeting, 29th November – 3rd December 2010, Boston, USA.

Wong, L.L.C., Menner, A., Bismarck, A., "Developing Hierarchical Macroporous Polymers the 'Green' Way", 18th Annual BioEnvironmental Polymer Society (BEPS) Meeting, 13th – 16th October 2010, Toronto, Canada.

Wong, L.L.C., Ikem, V.O, Menner, A., Bismarck, A., "Macroporous Polymers Synthesised with Mixed Emulsion Templates", MACRO 2010, 43rd IUPAC World Polymer Congress, 11th – 16th July 2010, Glasgow United Kingdom.

Poster Presentations at Conferences

Wong, L.L.C., Menner, A., Bismarck, A., "The Hype about Hierarchical PolyHIPEs" Imperial College Graduate School Poster Competition, 13th July 2012, London, United Kingdom.

Wong, L.L.C., Graeber, N., Menner, A., Bismarck, A., "Open Porous Polymer Foams Synthesised from Emulsion Templates Stabilised by Low Surfactant Concentrations" International Conference on Materials for Advanced Technologies (ICMAT), 26th June – 1st July 2011, Singapore.

Wong, L.L.C., Ikem, V.O., Menner, A., Bismarck, A., "Unique Microstructures in Poly-Pickering HIPEs Stabilised by Functionalised Nanoparticles: Synthesis and Applications" Imperial College Chemical Engineering PhD Symposium, 30th March 2010, London, United Kingdom.

Awards

AIChE Student Award 2012, 6th International Conference on Bioengineering and Nanotechnology (ICBN), 24th – 27th June 2012, Berkeley, California, USA.

Student Prize (First for Student Votes, Second for Academic and Industrial Panel), Imperial College Chemical Engineering PhD Student Symposium 2012, Imperial College London, UK

IChemE Particle Technology Subject Group Travel Award 2010, MACRO 2010, 43rd IUPAC World Polymer Congress, 11th – 16th July 2010, Glasgow United Kingdom.

Rectors Award 2009, Imperial College London, UK.

List of Figures

Figure 1-1: Micrograph images of softwood (left) with monodispersed cells versus hardwood (right) with a hierarchical cell structure or mixture of smaller and larger cells arranged in an optimised pattern to improve the overall mechanical strength (adapted from Wiedenhoeft et al.[13])....23
Figure 2-1: Schematic representing the process of emulsification and droplet stabilisation, adapted from Karbstein.[15]....29
Figure 2-2: Diagram summarising the mechanisms governing the destabilisation of emulsions. Adapted from Bismarck.[16]....30
Figure 2-3: Schematic representation of o/w (left) and w/o (right) emulsions....33
Figure 2-4: Diagrams representing the shape and packing of dispersed phase droplets in a (a) Dilute emulsion (b) Concentrated emulsion (c) HIPE with deformed droplets, each droplet is represented by a hexagon.[16]....35
Figure 2-5: Diagram of an ideal HIPE represented by monodispersed spheres (left). In reality, HIPE droplets are polydispersed (right).[16]....35
Figure 2-6: General representation of a surfactant molecule consisting of the polar, hydrophilic head and a hydrophobic tail.....37
Figure 2-7: Examples of cationic surfactants....39
Figure 2-8: Examples of anionic surfactants....39
Figure 2-9: Examples of nonionic surfactants....40
Figure 2-10: Examples of amphoteric surfactants....40
Figure 2-11: Representative schematic of micelle and reverse micelle (hydrophilic heads in the 'core')....41
Figure 2-12: Representative curve for defining the CMC according to the sudden change in physical properties (such as osmotic pressure, turbidity, surface tension etc.) of the surfactant solution with increasing concentration....41
Figure 2-13: Schematic of particle orientation and its effect on the curvature of the oil-water interface[42]....46
Figure 2-14: Chemical structure of oleic acid....47
Figure 2-15: E vs contact angle relationship for small particles adsorbed at the oil water interface (image taken from Binks et al.[40])....49
Figure 2-16: Sketch of liquid bridge geometry used for the analysis of capillary forces for coalescence between two partially wetted particles.[56]....50

Figure 2-17: Summary of the steric stabilisation mechanisms present in particle-stabilised emulsions including particle bilayer (a), bridging monolayer (b) and capillary attraction due to the menisci around each particle (c).[57] 52
Figure 2-18: SEM of conventional polyHIPE (left)[38] and the terminology used to describe polyHIPE structure (right)[79] 57
Figure 2-19: Schematic of pore throat preparation as proposed by Menner et al. (Adapted from Bismarck[16]) 59
Figure 2-20: SEM of polystyrene-divinylbenzene poly-Pickering-HIPE (left) and higher magnification of the pore walls (right) 60
Figure 2-21: Field-emission SEM image of poly-Pickering HIPE monoliths with poly(divinylbenzene)[85] 61
Figure 2-22: Image of Pickering polyHIPE with a partial open pore (image taken from Menner et al.[79]) 62
Figure 2-23: SEM images of poly (4-vinylbenzene chloride- divinylbenzene) polyHIPEs showing the largely mono-modal pore size distribution (left) and at higher magnification, a 'roughened' polymer wall due to hypercrosslinking (right) which increases the surface area.[94] 64
Figure 3-1: Schematic representing FEM analysis 75
Figure 3-2: Optical micrograph of a HIPE stabilised with 1 w/vol.% stirred for 10 min 77
Figure 3-3: Optical micrograph of a HIPE stabilised with 1 w/vol.% stirred for 30 s 77
Figure 3-4: SEM micrographs of polyHIPEs synthesised from emulsion templates stabilised with surfactant concentrations ranging from 1 w/vol.% (DS1), 2 w/vol.% (DS2), 5 w/vol.% (DS5), 10 w/vol.% (DS10) and 20 w/vol.% (DS20). SEM images are representative of the pore morphology across the entire polymer monolith. 81
Figure 3-5: Pore size distribution of DS1 to DS20. 82
Figure 3-6: Frequency of occurrence of pore throat sizes for DS1 to DS20. A GaussAmp function is fitted to them to calculate the mean pore throat size. 84
Figure 3-7: Summary of Young's modulus and crush strength of (hierarchial) poly(styrene-co-divinylbenzene)HIPEs. 87
Figure 3-8: Porous geometries generated to describe DS1 to DS20 (each side of the square corresponds to 100 µm) 90

Figure 3-9: Qualitative comparison between normalised Young's moduli obtained from compressing 2D porous geometries (Geometries 1 to 5) generated to represent HIPE templates with varying concentrations of surfactant (DS1 to DS20).....91
Figure 4-1: SEM of hierarchical macroporous polymers. A: Closed-cell poly-Pickering-HIPE M1. B: M3 with hierarchical structure consisting of distinctly open and predominantly closed-cell pores. C: M5 with conventional polyHIPE structure of small pores and numerous interconnecting pore throats. D: M6 with hierarchical structure consisting of distinctly open and predominantly closed-cell pores. Note that M3 is representative for M2 – M4 and M6 is the representative image for M6 – M7. 100
Figure 4-2: TEM of sections taken from hierarchical macroporous polymers. A: M1, B: M3, C: M5, D: M6. 100
Figure 5-1: Representative SEMs of Series I and II from emulsion templated porous materials before (left) and after (right) mechanical frothing. 120
Figure 5-2: Representative curves of the storage modulus (black) and tanδ (red) with respect to temperature of A1 (top) to A3 (bottom) subjected to oscillations at a constant frequency of 1 Hz. 122
Figure 5-3: Representative graphs for the mass loss (%) with increasing temperature for A1 (top) to A3 (bottom) in nitrogen. 124
Figure 6-1: Schematic summarizing the fabrication procedure for nanocomposite beads and macroporous polymers. 131
Figure 6-2: SEM of GO-P(S-co-DVB) nanocomposites beads synthesised by polymerising o/w emulsions containing 40 vol.% of internal phase (monomers) dispersed in 0.4 mg/ml GO suspensions. Well-dispersed GO flakes, clearly seen on the surface of the beads, are indicated with an arrow. 135
Figure 6-3: Comparing rGO stabilised HIPEs at different concentrations. HIPEs stabilised by 0.1 mg/ml rGO dispersed in the organic phase (top) showed rapid droplet coalescence within 30 s of preparation while HIPEs prepared with 1.2 mg/ml rGO dispersed in the organic phase (bottom) remained stable for at least 30 days on the bench, representative of the behaviour shown by all other HIPEs prepared in this series.....137
Figure 6-4: SEM of macroporous rGO-P(S-co-DVB) nanocomposite synthesised by the polymerisation of 75 vol.% w/o HIPEs stabilised by 1.2 mg/ml rGO. The

nanocomposite macroporous polymer pore throats and the well-dispersed rGO flakes covering the internal surface of the macroporous polymer are indicated with an arrow. 139
Figure 6-5: Average pore sizes of macroporous rGO-P(S-co-DVB) nanocomposites as function of rGO content. d_{10}, d_{50} and d_{90} correspond to the pore diameter at a cumulative size percentage of 10, 50 and 90% (number distribution), respectively. 140
Figure 6-6: Crush strength and Young's modulus of macroporous rGO-P(S-co-DVB) nanocomposites as function of rGO concentration in the organic phase. 141
Figure 6-7: SEM of macroporous rGO-P(S-co-DVB) nanocomposite synthesised by the polymerisation of 75 vol.% w/o HIPEs stabilised by 5 mg/ml rGO. 143
Figure 6-8: Storage modulus of macroporous rGO-P(S-co-DVB) nanocomposites as function of rGO concentration (with regards to organic phase) obtained from dynamic mechanical analysis at constant temperature of 30°C. 145
Figure 6-9: Conductivity of macroporous rGO-P(S-co-DVB) nanocomposites σ as a function of rGO volume fraction ϕ_c (with respect to the total volume of the macroporous nanocomposites). The solid line is the fit of experimental data to the conductivity equation (inserted equation in Figure 6-9),[202] where σ_c is the conductivity of the filler, ϕ_c is the percolation threshold and t percolation exponent. The fitted parameters are: ϕ_c=0.005 vol.%, σ_c=0.020, t=0.7. rGO volume fraction in the macroporous polymers (vol.%) are calculated using the value of 2.2 g/cm^3 as the density of rGO.[161] 146
Figure A0-1: Left: Macroporous polymer prepared using 0.75 w/vol.% surfactant stabilised emulsion template with pore size gradient. Right: SEM showing different pore size distributions taken from corresponding areas of the macroporous polymer sample on the left, a result of sedimentation at the low surfactant concentration of 0.75 w/vol.%. 169
Figure A0-2: Optical micrograph of HIPE used to prepare DS5 (5 w/vol.% surfactant) fresh after emulsification (top) and a day later (bottom). The negligible change in droplet size in the emulsion after a day showed that the effects of droplet coalescence on the final hierarchical structure were small. 170
Figure A0-3: Image of control sample 0 (above) after drying using convection oven in relation to the size of the Falcon tube (below) used for polymerisation. 171

Figure A0-4: DMTA profile of pure polyAESO showing a peak in tan δ at approximately 50°C 171
Figure A0-5: Photos of A3 before and after drying using convection oven (left top and bottom) v.s. modified freeze drying (right top and bottom). Shrinkage is halved and cracking is reduced by using a different drying protocol. 172
Figure A0-6: Representative curves of the Dynamic Mechanical behaviour (Storage modulus and Tan Delta vs T) of A1 (top) to A3 (bottom) with respect to increasing temperature, subjected to constant frequency oscillations. 174

List of Tables

Table 2-1 Summary of some commonly surfactants and their HLB number[34].....43
Table 2-2 Water solubility of surfactants in relation to the HLB range[35].....43
Table 3-1: Summary of surface area, average pore throat diameter and gas permeability of DS1 to DS20.....86
Table 4-1: Summary of the porosity (P), skeletal density (ρ_{SD}), gas permeability (k), crush strength (σ) and Young's modulus (E) of macroporous polymers synthesised from emulsion templates stabilised simultaneously by various particle (c_p) and surfactant concentrations (c_s): 99
Table 4-2: Summary of x_1, x_{T1} and N_1, which are the average pore size, average pore throat size and number of pore throats in the smaller pores typical for conventional polyHIPEs and x_2, x_{T2} and N_2 which are the average pore size, average pore throat size and number of pore throats per bigger pore typical for poly-Pickering HIPEs. .99
Table 5-1: Summary of composition of emulsion templates used, including the concentration of emulsifying particles (C_p) before (Series I) and after (Series II) mechanical frothing.....116
Table 5-2: Summary of porosity (P), skeletal density (ρ_S) and envelope density (ρ_E) measured before (Series I) and after (Series II) mechanical frothing. 117
Table 6-1: Summary of porosity and densities of macroporous rGO-P(S-co-DVB) nanocomposites and control samples 1 and 2. The emulsifier was dispersed in a 1:1 St:DVB solution (25 vol.%) with 1 mol% AIBN and emulsified with 5 g/L of aqueous electrolyte (75 vol.% for rGO and 80 vol.% for the controls). All emulsifier concentrations quoted are with respect to the organic monomer volume. 138
Table A0-1: Table summarising fitting parameters for pore throat distribution curves (Figure 3-6) 170

1 Introduction

'Macropores', defined under IUPAC standards as pores greater than 50 nm in size,[1] impart distinctive characteristics to bulk polymers such as porosity, permeability or buoyancy (depending on their interconnectivity), low density and weight. These traits make macroporous polymers an important class of materials that are widely used in numerous consumer products and engineering applications. Depending on the method(s) used to fabricate macroporous polymers, they can be interconnected or permeable to gases and could possess high surface areas due to their convoluted internal pore architectures. As a result of their unique properties, applications for macroporous polymers range from membranes for separation,[2] catalyst supports,[3] to scaffolds for tissue engineering and cell culture.[4] They are also attractive for specialty applications in composites, for example, in high performance sandwich composite structures such as Rohacell® and Divinycell. There are a variety of methods available to produce macroporous polymers such as gas foaming,[5] thermally induced phase separation (TIPS)[6] and the use of super critical carbon dioxide.[7] However, finding a production method which allows control over the interconnectivity (open or closed-cell), porosity, pore size and arrangement simultaneously remains a realistic challenge in the community. A method which could potentially overcome some of these constraints is emulsion templating. This novel technique has already proven itself to be versatile and robust, allowing the user flexibility to impart control over the final porous structure and to create bespoke shapes depending on the intended function.[8]

High porosity, permeability and mechanical integrity are important design elements considered during the production of synthetic porous materials using emulsion

templating. However, porosity and permeability are mutually exclusive to mechanical strength, which is known to decrease exponentially with an increase in porosity and/or permeability.[9] This is why the superior mechanical properties of naturally occurring porous materials such as wood, coral and spongy bone,[10] which are strong despite their high porosity (50 – 90%) and low density (approximately 1.5 g/cm^3) is intriguing.[11] On closer inspection, it is apparent that these natural porous materials have high load bearing strength[12] because they consist of pores that have different sizes or a multi-modal pore size distribution, arranged optimally to enhance its overall mechanical properties.[10] An example of this hierarchical porous structure is exemplified in hardwoods (which have a hierarchical arrangement of pores), distinguishing it from softwoods (which are not hierarchical and possess a monomodal pore size distribution) (Figure 1-1).

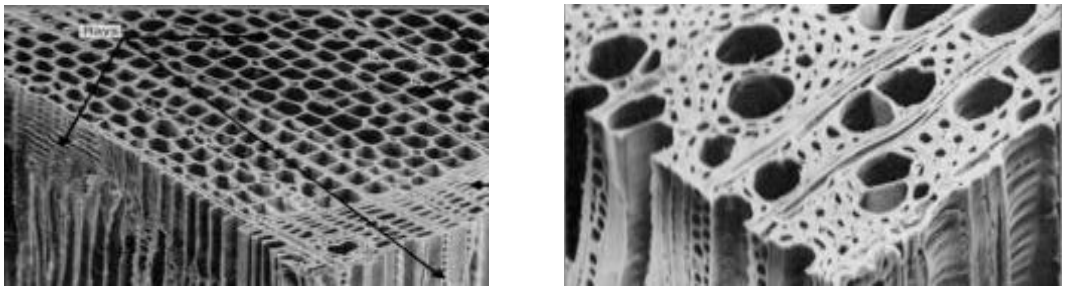

Figure 1-1: Micrograph images of softwood (left) with monodispersed cells versus hardwood (right) with a hierarchical cell structure or mixture of smaller and larger cells arranged in an optimised pattern to improve the overall mechanical strength (adapted from Wiedenhoeft et al.[13])

Driven by this naturally occurring phenomenon, a biomimetic approach – i.e. learning from the hierarchical arrangement of strong porous materials that exist in nature, such as hardwood, was taken. It was hypothesised that introducing hierarchical arrangement to synthetic porous polymers would also result in improved physical properties, such as compressive strength and stiffness, without compromising porosity. This is the idea that motivated us to reinvent traditional

emulsion templating techniques to develop new methods to produce synthetic porous materials which mimic the hierarchical structure of natural porous materials. This was approached strategically, first creating a **hierarchy of macropores**, by:

(i) Tuning emulsification parameters such as the stirring rate and surfactant concentration in order to generate multi-modal pore size distributions.

(ii) Combining surfactants and particles in a mixed emulsifier system to stabilise HIPE templates which polymerise to form macroporous structures with the characteristics of both polyHIPEs and poly-Pickering HIPEs.

(iii) Using a foamed emulsion, i.e. an air in water-in-oil, template system to produce new multi-modal porous structures.

The second approach was to formulate materials with a **hierarchical particulate network,** defined by an interconnected particulate network within the polymer matrix. This was carried out by:

(i) Using 2D graphene oxide flakes, acting both as emulsifiers as well as nano-reinforcements, to produce conductive macroporous nanocomposites.

Synthetic hierarchical macroporous polymers are anticipated to be desirable for many practical uses where high porosity and mechanical integrity are both imperative. These include the porous core of sandwich materials used for insulation purposes, solid supports for catalytic reactions, separating adsorbents and porous electrodes for thin film batteries.

1.1 Motivations and Objectives of This Project

The main aim of the project is to create macroporous polymers with hierarchical structures, achieved either by (i) producing a hierarchical arrangement of macropores or; (ii) creating an interconnected particulate network by emulsion templating.

The specific objectives of the project are to:

1. Establish reproducible experimental protocols and optimised process parameters for the formulation of hierarchical macroporous polymers by adapting and optimising 'classical' methods of emulsion templating at a 'laboratory-scale', for this purpose.
2. Prove that the analogy of hierarchical porous materials in nature is applicable to synthetic porous materials, by showing that hierarchical macroporous polymers outperform conventional emulsion templated macroporous polymers.
3. Demonstrate qualitatively, using a simulation study, the influence of macroporous hierarchy on the Young's modulus of hierarchical macroporous polymers compared to conventional emulsion templated ones.
4. Devise a new procedure to formulate hierarchical emulsion templates with high porosities using a bio-based monomer.
5. Create an interconnected particle hierarchy using nano-particulate emulsifiers to create a interconnected network within the polymer matrix of a macroporous polymer.

1.2 Structure of This Thesis

This thesis is divided into 7 chapters. The introduction (Chapter 1) provides a broad overview of the entire thesis and elucidates the motivation and objectives for this research. In this chapter, the hypothesis for the research is stated and the strategy for proving the hypothesis is also outlined. Chapter 2 provides relevant background information and the governing principles of emulsions, emulsifiers and emulsion templating. This chapter also summarises important literature necessary to set the context for the rest of the work. It is from here that the thesis is divided into two main sections following the strategy decided for this research. The first section, made up of Chapter 3 to 5, each an independent publication, describes novel methods to synthesise macroporous polymers with a **hierarchy of macroporous**. Subsequently, the second section, consisting of Chapter 6, also a standalone publication, describes a method to introduce a further level of hierarchy in the polymer matrix in the form of a **hierarchical particulate network**.

The first section starts with Chapter 3, which introduces a method to produce hierarchical macroporous polymers by optimising emulsification parameters such as the stirring rate and emulsifier concentration of surfactant-stabilised emulsion templates. Following this, Chapter 4 describes the use of both surfactants and particles in synergy to stabilise emulsions to create a hierarchical arrangement of pores. By combining open and closed pore structures found in conventional surfactant stabilised and particle stabilised emulsion templates respectively, a hybrid structure was created and shown to have a positive influence on the physical properties of the resulting hierarchical porous polymers. After studying hierarchical macroporous structures produced using emulsion templates stabilised by surfactants and a combination of surfactants and particles, a new method to generate hierarchy

in emulsion templates was conceptualised and executed in Chapter 5. This chapter describes a novel method of producing hierarchical macroporous structures by polymerising mechanically frothed bio-based, particle-stabilised emulsion templates with medium internal phase volumes.

Having studied three different ways to produce hierarchy at the macroporous level in section one, the second section of the thesis, Chapter 6, describes a method to produce a further level of hierarchy in the form of an interconnected particle network within the polymer matrix of macroporous polymers. Graphene oxide flakes (also referred to as ‘particles’) were used as particulate emulsifiers and polymer nanofillers simultaneously. Conductivity of the final macroporous materials indicated the presence of an interconnected network of graphene oxide flakes throughout the polymer matrix.

After validating the hypothesis proposed through the analysis and discussion of results obtained from these four independent studies, conclusions and recommendations for further work are summarised in Chapter 7.

2 Background

2.1 Introduction to Emulsions

Emulsions are classically defined as dispersions of droplets of one liquid (known as the dispersed or internal phase) in another liquid (known as the continuous phase) with which it is not miscible[1] (IUPAC 1972). Since they are dispersions, emulsions are also considered as colloidal systems, although emulsion droplets often exceed the colloidal size limit of 1000 nm. Emulsions are thermodynamically unstable mixtures, a concept that can be understood by considering the change in the Gibbs free energy during the dispersion of one liquid in another liquid, given by:

$$\Delta G = \gamma \Delta A - T\Delta S$$

Equation 2-1[14]

Where ΔG = Change in Gibbs free energy (J); γ = Surface or interfacial tension (N/m); ΔA = increment of area (m^2); T = Temperature (K); ΔS = Change in entropy (J/K)

The dispersion process generates new interfaces, producing very high interfacial energies (γ) and an increment in area (ΔA). Considering that the change in entropy resulting from the breaking up of droplets from its constituent phases is relatively small, the overall ΔG is greater than zero since $\gamma \Delta A \gg T\Delta S$. This translates to a large thermodynamic driving force for the emulsion to separate into its original constituent phases. Although this means that emulsions are inherently thermodynamically unstable, kinetic stability can still be promoted by the addition of an emulsifier. The emulsifier, by adsorbing at the interface between the two liquid

phases, reduces the overall interfacial tension in the system and thus slows down the rate of emulsion destabilisation. Emulsifiers can be surface active agents (surfactants), particulate emulsifiers (also known as Pickering emulsifiers), or a combination of both surfactants and particulate emulsifiers, details of which will be described in later sections of this thesis.

2.2 The Emulsification Process

The process of emulsification is aptly summarised in Figure 2-1, where mechanical energy is input to an 'emulsion system' comprising the continuous phase, the dispersed phase and an emulsifier. The dispersed phase is mechanically broken into individual droplets, generating many interfaces where the emulsifier adsorbs. Depending on the total free energy of the system, the dispersed phase droplets would (i) come together and undergo liquid film rupture, coalescing to form larger, more stable droplets, increasing the ΔA or (ii) continue to exist as small, stable droplets if adsorption of the emulsifier has sufficiently lowered the γ. Both effects cause $\gamma \Delta A < T \Delta S$ and a reduction in the total free energy of the system, forming a (kinetically) stable emulsion.

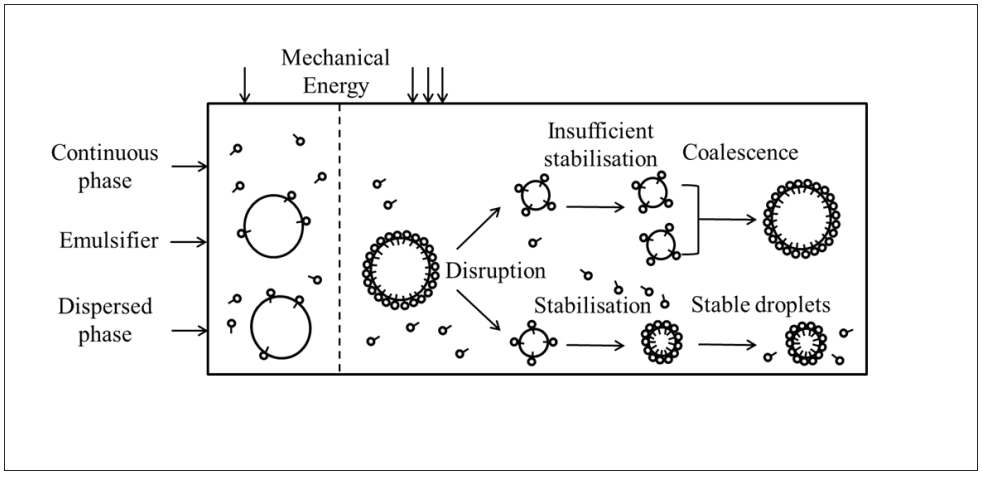

Figure 2-1: Schematic representing the process of emulsification and droplet stabilisation, adapted from Karbstein.[15]

Although emulsions can be kinetically stable, over time, they will destabilise by undergoing mechanisms schematically described in Figure 2-2:. These include:

(i) Creaming, when dispersed droplets of one phase (oil) separate from the emulsion due to large enough differences in densities. Occurs in o/w emulsions.

(ii) Flocculation, when individual droplets aggregate with one another due to Brownian motion or electrostatic interactions.

(iii) Sedimentation which is essentially the 'opposite' of creaming, when droplets sink due to the effects of gravity. Occurs in w/o emulsions.

(iv) Coalescence, which is the rupture of the liquid film that separates each dispersed phase droplet from the next. Since processes (i) to (iii) have brought dispersed phase droplets closer to each other, coalescence is more likely to occur. Droplet coalescence results in the production of a separate oil layer or destabilisation of the emulsion.

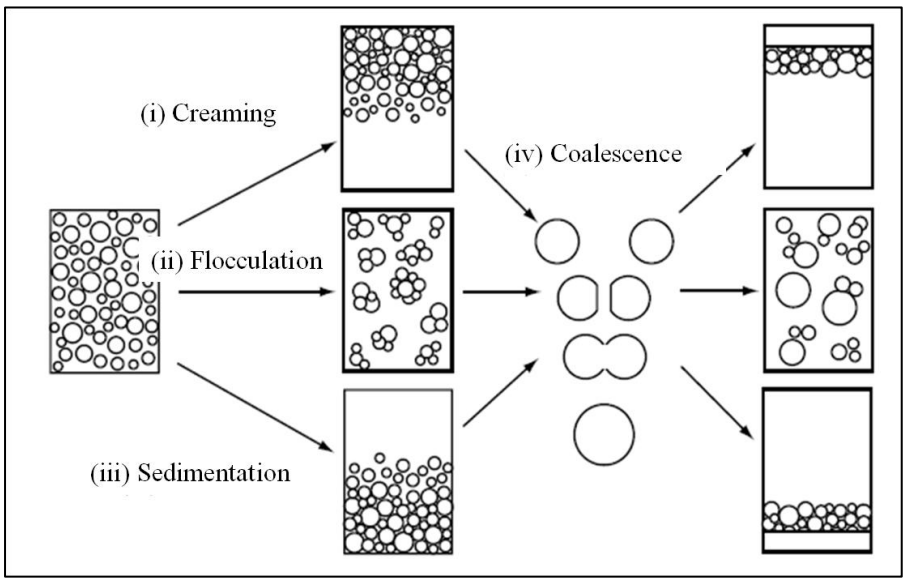

Figure 2-2: Diagram summarising the mechanisms governing the destabilisation of emulsions. Adapted from Bismarck.[16]

An additional effect to those represented in Figure 2-2: is the growth of larger droplets at the expense of smaller droplets or the coarsening of small droplets over time, a process termed Ostwald ripening. Ostwald ripening occurs when dispersed phase molecules diffuse from ‘smaller’ dispersed phase droplets to the ‘larger’ ones through the continuous phase, driven by the pressure difference between the inside and outside of a curved interface, as shown by the Laplace equation (Equation 2-2),

$$\Delta \mathrm{p} = \frac{2\gamma}{r}$$

Equation 2-2

Where $\Delta \mathrm{p}$ is the pressure difference between the inside and outside of a curved interface, also known as the Laplace pressure, γ is the interfacial tension and r is the radius of the curvature of the interface. From this relationship (Equation 2-2), it can be inferred that the greater the radius of the curvature, the lower the pressure difference and hence the free energy of the system. The rate of Ostwald ripening is dependent on the solubility of the dispersed phase in the continuous phase, governed by a relationship based on the Kelvin equation (Equation 2-3),

$$\ln\left[\frac{s}{s_\infty}\right] = \frac{2\gamma V_m}{rRT}$$

Equation 2-3

Where s and s_∞ are the solubilities of the dispersed phase in the continuous phase for the bulk liquid and droplets with radius r respectively, γ is the interfacial tension between the two liquid phases and V_m is the molar volume of the dispersed phase, R and T refer to the gas constant and the temperature for the system.

Over time, the coarsening of droplets due to Ostwald ripening manifests as droplet coalescence, contributing to the destabilisation of an emulsion. The rate of Ostwald ripening can be circumvented by adding electrolytes such as calcium chloride dihydrate to the dispersed aqueous phase in a w/o emulsion. This lowers the solubility of the dispersed aqueous phase in the continuous oil phase,[17] reducing the rate of Ostwald ripening and hence coalescence.

It is important to note that the destabilisation processes described hence far are all happening simultaneously. However, the properties of the emulsion dictate which destabilisation mechanism dominates. For example, when two phases in an emulsion are extremely immiscible or when the continuous phase is very viscous compared to the dispersed phase, emulsion destabilisation will likely be dominated by the coalescence due to phenomena (i) to (ii) in Figure 2-2:.

2.3 Classification of Emulsions

There are many ways of classifying emulsions. They can be categorised according to type (oil in water, water in oil or multiple phase systems etc.), application (drugs, cosmetics, food, industrial processes etc.) and according to droplet sizes (micro verses macro emulsions). This section deals with two such main categories of emulsions which helps to contextualise the emulsion types discussed in this thesis.

2.3.1 Continuous Phase

Emulsions are most often classified according to the dispersed or continuous phase. Usually one phase is an organic or oil phase (such as decane or cyclohexane), often non-polar in nature while the other is an aqueous phase which is polar (such as a calcium chloride aqueous solution). Emulsions of aqueous droplets dispersed in a continuous oil phase are known as water in oil emulsions or w/o (Figure 2-3 left).

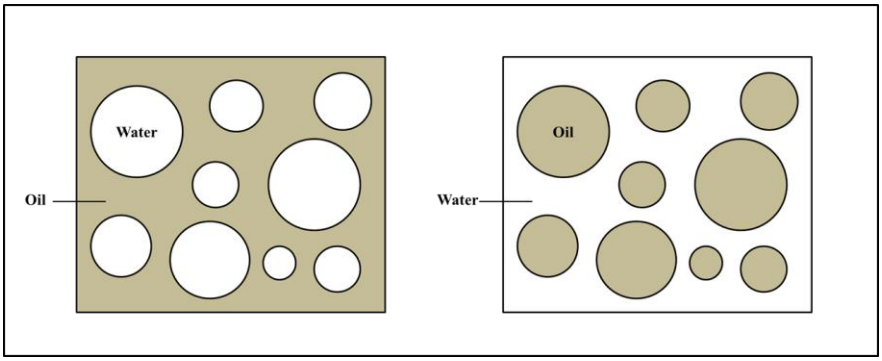

Figure 2-3: Schematic representation of o/w (left) and w/o (right) emulsions

Some examples of w/o emulsions are butter, margarine and certain salad dressings with a 'greasier' formulation. When the emulsion consists of droplets of oil dispersed in a continuous aqueous phase (Figure 2-3 right), it is referred to as oil in water emulsions or o/w. Some examples are milk, low-fat mayonnaise and certain face lotions which have a more watery texture.

The type of emulsion formed can be determined using different methods such as a 'drop test' which involves dropping a small amount of the emulsion into water observing how it behaves macroscopically. If the emulsion mixes well with water and turns the solution cloudy, the emulsion is o/w. The same cloudy effect would be seen when w/o emulsions are dropped into an oil phase. Another method to test the type of emulsion formed involves the use of an oil-based dye such as Sudan Red, which is added to the emulsion. If the continuous phase is oil (w/o emulsion), the dye quickly spreads, colouring the emulsion. However, if the emulsion is o/w, the colour from the dye will not transfer.

The type (o/w or w/o) of emulsion that forms is dependent on various parameters. These include the volume ratio of each phase, the nature of the emulsifier, the miscibility of the two phases and the rate and order of mixing the components in the emulsion system. Bancroft's rule is a rule of thumb used when predicting the type of

emulsion that may form. The rule states that the type of emulsion (o/w or w/o) formed should be such that the internal phase is the one of higher solubility.[18]

This thesis is focused on the preparation of macroporous polymers using oil-soluble monomers, thus, reference is often made to w/o emulsions, where the continuous phase consists of the monomer solution (usually a mixture of styrene and the cross-linker divinylbenzene), emulsifier and a free radical initiator and the dispersed phase is made up of an aqueous salt solution.

2.3.2 Internal Phase Volume Ratio

Emulsions can also be classified according to the internal phase volume ratio. When the internal phase volume used is below 30 vol.% with respect to the total emulsion volume, they are known as Low Internal Phase Emulsions or LIPEs. Between 30 to 74 vol.% with respect to the total emulsion volume, they are known as Medium Internal Phase Emulsions or MIPEs. High internal phase emulsions or HIPEs, are defined as emulsions with greater than 74.05 vol.% internal phase with respect to the total emulsion volume.[19] This specific percentage corresponds to the maximum packing fraction of uniformly distributed, perfect and rigid spheres (representing dispersed phase droplets). As the internal phase volume fraction increases past 74.05 vol.%, the dispersed phase droplets compress causing areas where neighbouring droplets are in close contact with each other to thin out and flatten. The perfect spherical shape becomes lost and droplets become more polyhedral in shape. A 2D representation of the shape and packing of emulsion droplets as the concentration of the dispersed phase increases is represented in Figure 2-4.

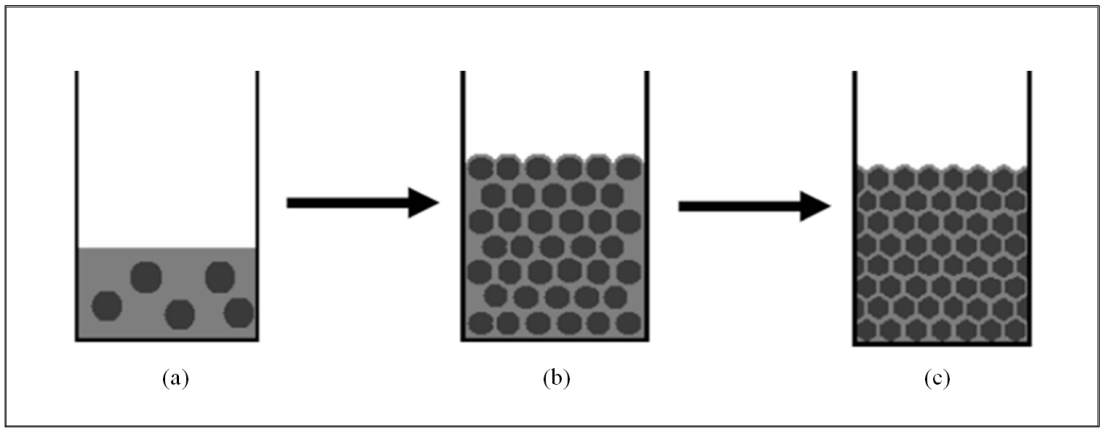

Figure 2-4: Diagrams representing the shape and packing of dispersed phase droplets in a (a) Dilute emulsion (b) Concentrated emulsion (c) HIPE with deformed droplets, each droplet is represented by a hexagon.[16]

In reality, HIPEs can hold a much greater internal phase volume, sometimes as high as 99 vol.%. This is due to the imperfect shapes and non-uniform sizes of real emulsion droplets and the arrangement of smaller droplets squeezed in the interstitial spaces between larger droplets, as seen in Figure 2-5 (right). The properties of these highly concentrated emulsion systems have been studied in detail, particularly by Lissant[19] and Princen.[20, 21]

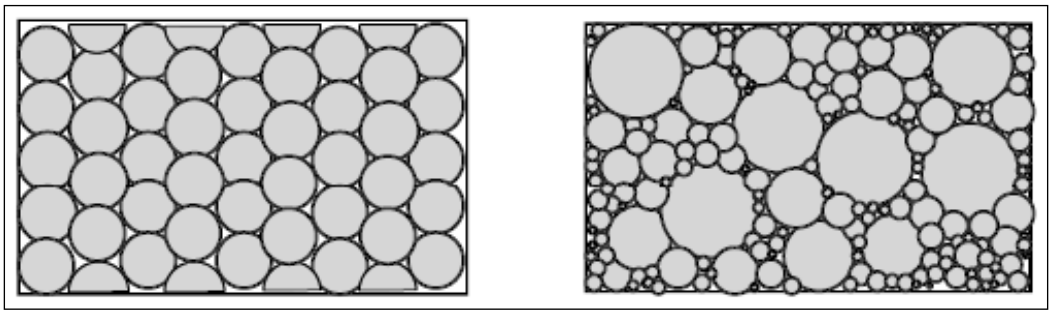

Figure 2-5: Diagram of an ideal HIPE represented by monodispersed spheres (left). In reality, HIPE droplets are polydispersed (right).[16]

Concentrated emulsions often have a polydispersed droplet size distribution, usually modelled with mathematical and empirical relationships used to describe other colloidal systems such as sprays or atomised droplets. These include the Nukiyama-Tanasawa equation, the Rosin-Rammler equation[22, 23] and the lognormal probability

distribution function.[24] Although each of these models have limitations, an adaptation of the lognormal distribution, described in Equation 2-4, gave arguably the most satisfactory fit for concentrated emulsion systems prepared using mechanical stirring.[25, 26] Having said that, it was apparent from the studies published on this topic that no one distribution function can be applied across all emulsion systems. This is indicative of the sensitivity of emulsion droplet sizes to variations in emulsification parameters (stirring rate, concentration and type of emulsifier used etc.) from one emulsion system to the next. It remains that any model used would have to be 'optimised' using an iterative process of experimental data fitting before it can serve as a predictive tool to determine the droplet distribution in a concentrated emulsion system. This discussion on the choice of distribution function to accurately fit a droplet size distribution has implications in later parts of this thesis where the pore size distribution (assumed to have the same distribution as the droplet size distribution of the emulsion template used to prepare it[27]) was found to be fitted well by a variation of the lognormal function (Equation 2-4) as a starting point.

$$p = \frac{1}{\Delta R\sqrt{2\pi}} exp\left[\frac{lnR - ln\bar{R}}{2\Delta R^2}\right]$$

Equation 2-4[28]

Where p is the probability distribution function for a log-normal distribution, R is the droplet radius, $\bar{R}$ is the mean droplet radius and $\Delta R = (R - \bar{R})$

The unique consistency and high viscosity of most HIPEs make it a favourable choice for formulations such as paints, cosmetics and food products. HIPEs have also been lauded as a possible vehicle for drug delivery in pharmaceuticals[29] and a solution to challenging engineering problems, such as in enhanced petroleum recovery.[30] One of the up and coming applications of HIPEs is the preparation of

macroporous polymers via a versatile technique called emulsion templating which will be discussed in Section 2.5.

2.4 Emulsifiers

The type of emulsifier used has implications on the properties of the final emulsion formulation. In this section, surfactants and particulate emulsifiers as well as the synergistic effects when both these emulsifiers are combined are described, with a focus on reported mechanisms for emulsion stabilisation or destabilisation.

2.4.1 Surfactants

2.4.1.1 Properties and Examples of Surfactants

Surfactants are surface active agents which adsorb at interfaces (and surfaces) due to its amphiphilic molecular structure, i.e., each molecule has both a polar, hydrophilic 'head' and a non-polar, hydrophobic 'tail', represented in Figure 2-6. When surfactants are allowed to equilibrate in an oil-water dispersion, the hydrophilic 'head' tends to associate with the water phase and the hydrophobic 'tail' with the oil phase. This adsorption effect lowers the high interfacial tension created in the dispersion which in turn lowers the Gibbs free energy (Equation 2-1), making it energetically favourable to form stable emulsions.

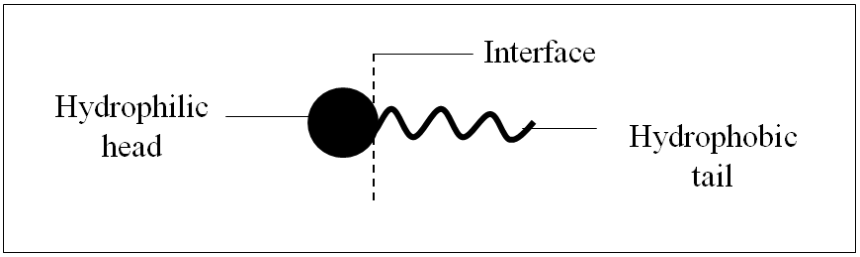

Figure 2-6: General representation of a surfactant molecule consisting of the polar, hydrophilic head and a hydrophobic tail.

Surfactants are often classified based on the molecular structure of their hydrophilic head group as they often have different properties and hence applications. Hydrophilic head groups can be ionic (anionic or cationic), non-ionic (usually polymeric), amphoteric or Zwitterioninc (usually phospolipids) while the hydrophobic tail is a long hydrocarbon chain in a straight or branched configuration. Ionic surfactants can be cationic salts, characterised by a positively-charged head group (Figure 2-7) and are commonly used in fabric softening formulations. Anionic surfactants are identifiable by a negatively charged head group and a long hydrocarbon chain as the lipophilic group. They are commonly found in dishwashing liquids, shampoos and laundry detergents (Figure 2-8).

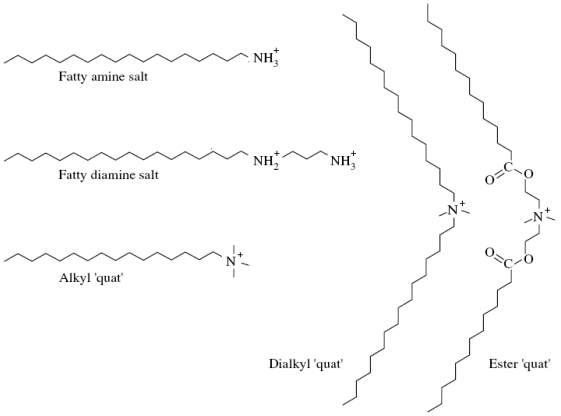

Figure 2-7: Examples of cationic surfactants

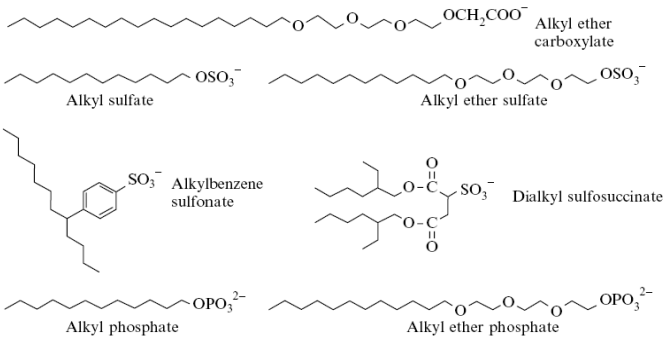

Figure 2-8: Examples of anionic surfactants

Non-ionic surfactants are uncharged but have a polar headgroup which is usually a polyhydric alcohol or ethylene oxide and the lipophilic group which is usually a fatty acid or a fatty alcohol (Figure 2-9). Examples of non-ionic surfactants include commercially available, non-ionic ones such as SPAN™ and TWEEN™ families which are biocompatible sorbitan derivatives. They are usually components of kitchen grease removers and other household cleaners.

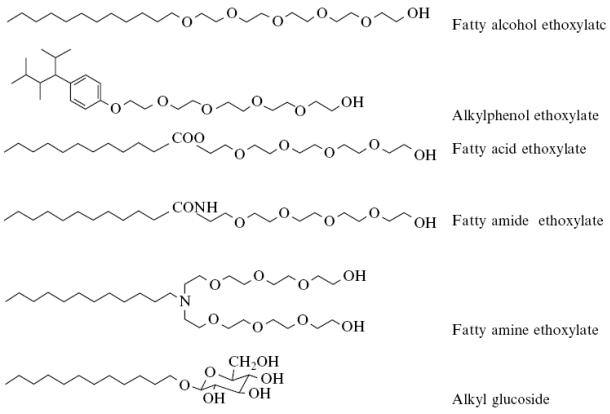

Figure 2-9: Examples of nonionic surfactants

Amphoteric or Zwitterionic surfactants have headgroups that contain both positive and negative charges and are commonly lipids (Figure 2-10). They are frequently used in cosmetics, shampoos and handwash products.

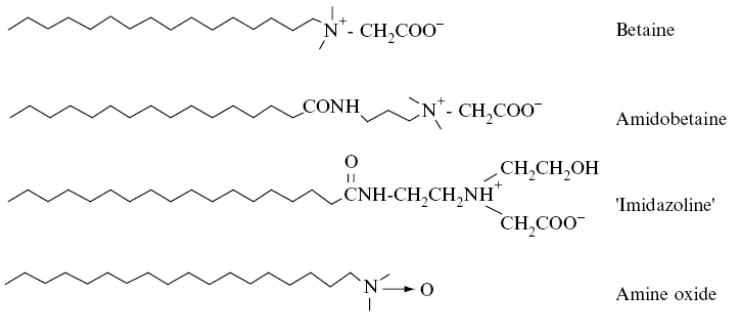

Figure 2-10: Examples of amphoteric surfactants

2.4.1.2 Stabilisation Mechanisms in Surfactant Stabilised Emulsions

Depending on the nature and concentration of the surfactant and other external factors such as temperature, presence of electrolytes etc., surfactants self-assemble to form structures known as micelles. These structures, represented in Figure 2-11, start to form after the critical micelle concentration (CMC). The CMC is detectable by an abrupt change in properties (surface or interfacial tension, turbidity, conductivity,

refractive increment etc.) with increasing surfactant concentration of the surfactant solution[31] (represented in Figure 2-12). It usually lies in the very dilute range of 0.001 to 0.005 wt.%[31]

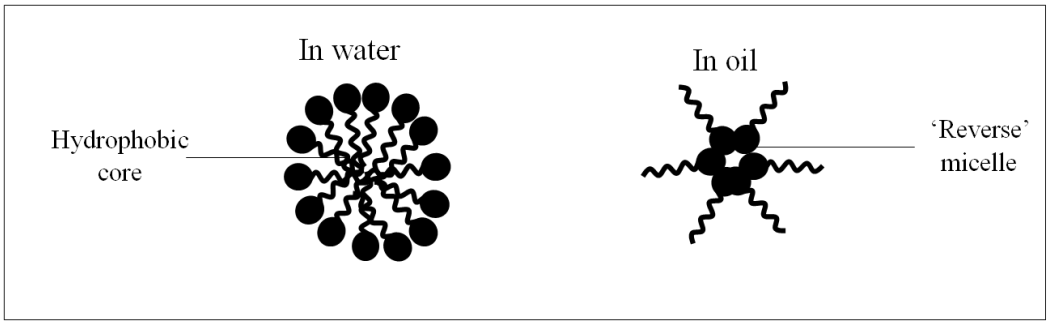

Figure 2-11: Representative schematic of micelle and reverse micelle (hydrophilic heads in the 'core')

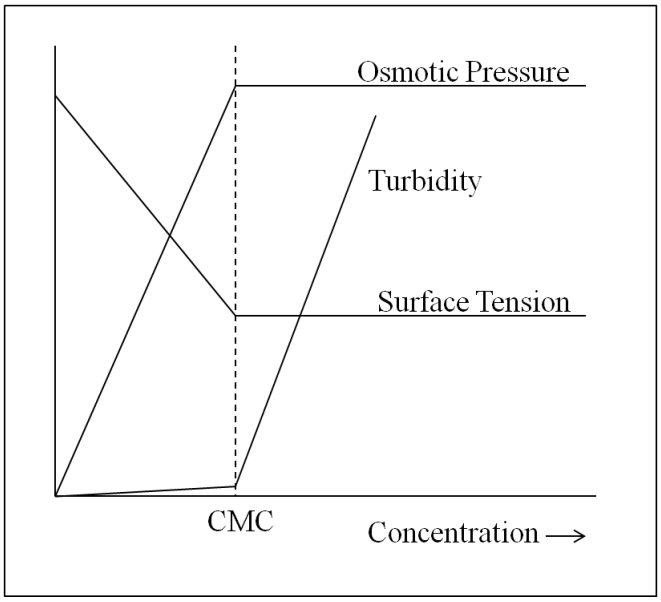

Figure 2-12: Representative curve for defining the CMC according to the sudden change in physical properties (such as osmotic pressure, turbidity, surface tension etc.) of the surfactant solution with increasing concentration.

During emulsification, many interfaces are generated due to the input of mechanical energy. Surfactants will adsorb at the oil-water interface of droplets in emulsions and serve to reduce the interfacial tension thereby promoting emulsion stability. At the same time, surfactants also prevent droplet (re)coalescence by the Gibbs-Marangoni

effect.[32] This occurs when two emulsion droplets approach one another, attracting surfactants to the droplet surface during their progress. When the droplets are at their closest, the surfactant available for adsorption in the continuous phase solution (the surface excess) reduces to a minimum. This creates a gradient in the interfacial tension between the droplets, which causes a flow of liquid towards the site of higher interfacial tension. This movement of liquid causes the droplets to move apart from each other, preventing coalescence and promoting emulsion stability. Furthermore, if surfactants themselves impart characteristics to the droplet surface dependent on their properties (ionic, non-ionic etc.). This also encourages repulsive interactions which contribute to overall emulsion stability.

2.4.1.3 Surfactant Selection

There are a few heuristics used to decide what surfactant, or in some cases, blend of surfactants to use when preparing emulsions. The determination of the hydrophilic-lipophilic balance (HLB) was one of the first methods introduced by Griffin in 1949.[33] The HLB is a dimensionless number which can be calculated for a surfactant at 20°C using Equation 2-5. It quantifies the influence of both the hydrophobic and hydrophilic portions of the surfactant based on its chemical structure and is only applicable to non-ionic surfactants.

$$HLB = 20\frac{M_H}{M_H + M_L}$$

Equation 2-5

Where M_H refers to the molecular weight of hydrophilic portion and M_L is the molecular weight of lipophilic portion.

When two or more surfactants are blended together, the HLB is determined using Equation 2-6.

$$HLB_{mixture} = \sum X_i HLB_i$$

Equation 2-6

Where $HLB_{mixture}$ is the HLB of the surfactant mixture, X_i is the mass fraction of component i and HLB_i is the HLB of component i.

Generally, w/o emulsifiers have a low HLB of 3 – 8 while o/w emulsifies have a higher HLB in the range of 8 – 18. Ionic surfactants have very high HLB values in excess of 20. The HLB for surfactants commonly used in the emulsion templating community and reported in this thesis are summarised in Table 2-1.

Table 2-1 Summary of some commonly surfactants and their HLB number[34]

Surfactant	HLB
Oleic acid	1
Sorbitan monooleate (SPAN™ 80)	4
Hypermer ™ 2296	4.9
Hypermer ™ 246SF	6
Sorbitan monolaurate (SPAN™ 20)	9
Polyoxyethylene sorbitan monooleate (TWEEN™ 80)	15
Sodium Dodecyl Sulfate (SDS)	40

As per Bancrofts' rule, the solubility of surfactants in water (Table 2-2), when used together with the HLB range, also provides useful insight for the type of emulsions expected for certain proprietary surfactants or surfactant blends for which the exact molecular structure is unknown.

Table 2-2 Water solubility of surfactants in relation to the HLB range[35]

Behaviour in Water	HLB Range	Type of Emulsifier
No dispersibility	1 – 4	w/o emulsifier
Poor dispersion	3 – 6	
Milky dispersion after vigorous agitation	6 – 8	
Stable milky dispersion	8 – 10	Wetting agent
From translucent to clear	10 – 13	o/w emulsifier
Clear Solution	13+	

Although the HLB is deemed a quick guide for selecting an emulsifier, experience has shown that it should be considered with caution. In reality, external factors such as impurities in the oil phase, electrolytes in the water phase and the presence of co-surfactants or other additives present in the surfactant all have an effect on the type of emulsions that form. Other external factors such as temperatures, oil to water ratios and stirring rates etc., also affect the type of emulsion that forms, in addition to the choice of surfactant. Hence, it is common practice in this research group to test a range of surfactants (or mixtures of different surfactants) at the required conditions before deciding on the best suited one for any emulsion system studied.

In this report, two commercially available low HLB non-ionic polymeric surfactants were used to prepare w/o HIPEs. They are Hypermer™ 2296 and Hypermer™ B246SF, specialty surfactants used to aid steric stabilisation and curb the aggregation of asphaltene molecules in oilfield operations. Since the Hypermer 'family' of surfactants are propriety products of Croda International PLC, information on the exact chemical composition and structure of these surfactants is limited. However, Croda has revealed that Hypermer™ 2296 is a blend of a sorbitan ester (hydrophobic portion) and a polyisobutenyl succinic anhydride (PIBSA) based derivative (hydrophilic portion). Whilst Hypemer™ B246SF is a polymeric stabiliser consisting of hydrophobic polyhydroxy fatty acid and hydrophilic poly(ethylene glycol) blocks.

2.4.2 Particles

Another class of emulsifiers are solid colloidal particles. Emulsions stabilised by particles are known as particle-stabilised, Ramsden or Pickering emulsions, named after the two scientists who discovered them.[36, 37] Particulate emulsifiers have

generated much interest, mostly driven by the cheaper unit cost of particles compared to surfactants but more importantly, the immense stability of particle-stabilised emulsions. This stability creates a great potential for use in industrial applications where emulsions are subjected extreme physical conditions (temperature and pH) such as in oil recovery operations[38] and pharmaceutical applications.[39]

2.4.2.1 Particle Stabilisation mechanisms

2.4.2.1.1 Particle Adsorption at the Interface

The wettability of the particles at the oil-water interface is used to characterise its hydrophobicity or tendency to like the oil or water phase, analogous to the HLB of a surfactant.[40] Wettability is quantified by the contact angle (θ) between particles and the oil-water interface and is generally considered a key descriptive property for particulate emulsifier behaviour.[41] The contact angle is related to the interfacial tensions in an oil-water-solid system by the Youngs' equation (Equation 2-7).

$$cos\theta = \frac{\gamma_{os} - \gamma_{sw}}{\gamma_{ow}}$$

Equation 2-7

Where θ = contact angle of particle at the oil-water interface, $\gamma_{os}, \gamma_{sw}, \gamma_{ow}$ = interfacial tension between the oil-solid, solid-water and oil-water phases respectively.

When particles adsorb at the interface, a certain curvature is adopted based on its contact angle as seen in Figure 2-13. When θ < 90° (measured with respect to the water phase), particles are preferentially 'wetted' by the water phase or more hydrophilic and likely to stabilise o/w emulsions. When θ > 90° particles are

preferentially ‘wetted’ by the oil phase or more hydrophobic and hence more likely to stabilise w/o emulsions.

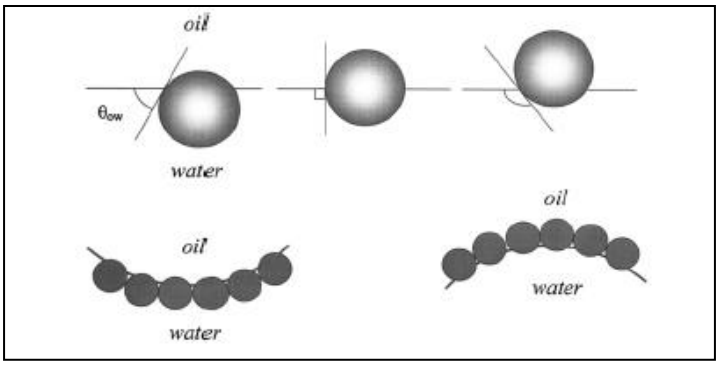

Figure 2-13: Schematic of particle orientation and its effect on the curvature of the oil-water interface[42]

Different types of particles have been tested for their ability to stabilise emulsions. Silica[43], titania,[44, 45] laponite clay,[46] polystyrene latex[47] and carbon particles[48] are examples of particles which have been reported to stabilise emulsions prepared from oils such as alkanes, silicones, alcohols and esters with water. Depending on the type of emulsion intended, particles are chosen based on their commercial availability, size and surface properties. Arguably, the most extensively investigated particulate emulsifier by far is silica, mainly for its commercial availability but also for its well-known surface chemistry. The silica surface consists of silanol groups (SiOH, $Si(OH)_2$ etc.) which can be manipulated to varying degrees of hydrophobicity by chemical modification, for example. Silanes (alkylaminosilanes and alkylchorosilanes etc.) react with the hydrophilic –OH groups on the silica surface forming hydrophobic Si-O-Si bonds, thereby changing its wettability. Depending on the concentration and time of exposure to these silane substrates, the degree of modification and hence the surface hydrophobicity can be controlled.[49, 50]

Another method to modify the silica particle surface is by adsorption (physisorption or chemisorption).[51] This involves the adsorption of reagents on the surface of silica particles via physical interactions such as van der Waals, hydrophobic interactions or chemical interactions such as hydrogen bonding which changes the wettability of the particle surface. One approach is to adsorb cationic surfactants such as cetyltrimethylammonium bromide (CTAB) onto silica. The positively charged polar CTAB 'head' associates with the surface of the silica particles, exposing a hydrophobic tail which improves the dispersion state of silica and reduces agglomeration.[51] Oleic acid is another reagent used to increase the hydrophobicity of silica particles since it is an amphiphilic molecule due to its hydrophilic, polar head and a hydrophobic, hydrocarbon tail (Figure 2-14).[38, 44, 45, 52] In solution, the polar head group of oleic acid adsorbs to the hydroxyl groups on the surface of silica, leaving the hydrophobic tail 'exposed' increasing the hydrophobicity of the otherwise hydrophilic silica surface by the attachment of long alkyl chain. Evidence exists for hydrogen bonding of oleic acid to free SiOH groups on the surface of silica but also physisorption of oleic acid caused by dipole-dipole interactions.[53]

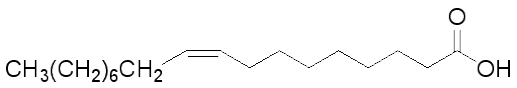

Figure 2-14: Chemical structure of oleic acid

In the case of nanoparticles that are small enough such that the effects of gravity are negligible, the free energy gained by losing an area of liquid-liquid interface due to the adsorption of a spherical particle at the interface is calculated by a relationship between the free energy gained from adsorption of a particle and the contact angle of the particle at the interface, proposed by Koretsky and Kruglyakov (Equation 2-8).[54]

$$E=\pi r^2 \gamma_{ow}(1 \pm \cos\theta)^2$$

Equation 2-8

Where E = free energy gained, r = effective particle diameter, γ_{ow} = interfacial tension between the oil (o) and water (w) phase, θ = contact angle of particle at the oil-water interface. The choice of sign inside the brackets is determined by the preferential removal of the particle into the oil (+) or water (-) phase.

Taking fumed silica particles with a radius of 10^{-8} m as an example, for particles with a contact angle of 90° (perpendicular to the toluene-water interface with an interfacial tension of 0.036 Nm^{-1}), the adsorption energy barrier reaches a maximum of almost 3000 kT (Figure 2-15). A large energy input is necessary to dislodge these particles from the interface. Thus, adsorption is considered almost irreversible and emulsions prepared using these particles with contact angles at or near 90° will remain stable over a relatively long time compared to surfactants. If particles with a contact angle of between 0° and 20° or 160° and 180°, the energy required to dislodge them from the interface is much lower, below 10 kT, making them thermodynamically less stable.

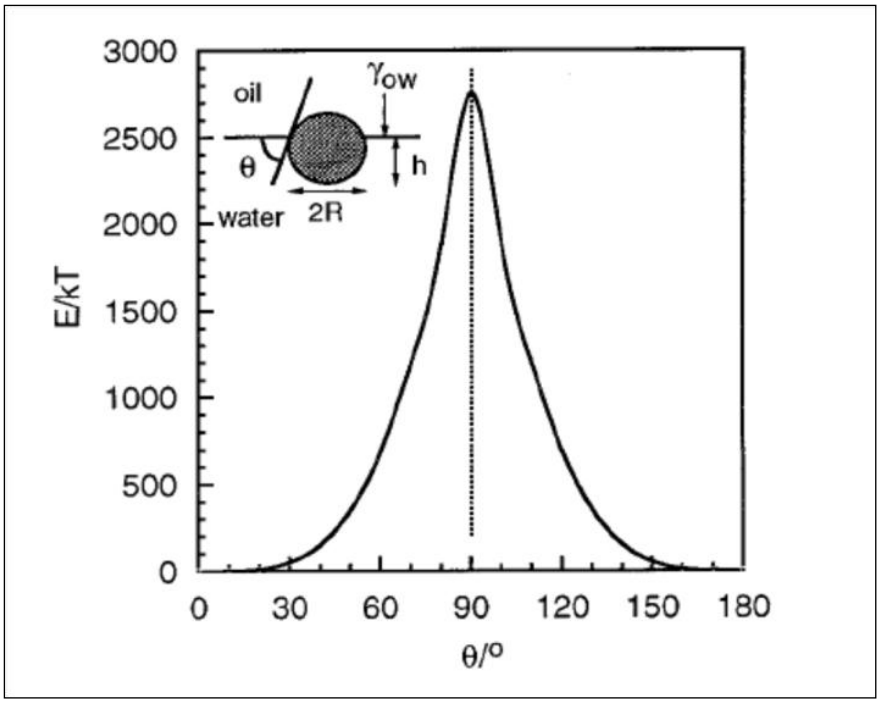

Figure 2-15: E vs contact angle relationship for small particles adsorbed at the oil water interface (image taken from Binks et al.[40])

2.4.2.1.2 Capillary Forces

A geometric analysis carried out by Megias-Alguacil et al.[55, 56] considered both the capillary and van der Waals forces between uncharged colloidal particles linked by a liquid bridge. The study concluded that capillary forces are the dominant stabilisation force most of the time but the van der Waals force becomes noticeable when the distance between the particles is very small. Capillary forces can be described by Equation 2-9 which is derived from the analysis of Figure 2-16.

$$F_{cap} = \{-2\pi\gamma\ Rsin(\alpha+\theta)\} - \left\{\pi\gamma R^2 sin^2\alpha\left(\frac{1}{L}-\frac{1}{\rho}\right)\right\}$$

Equation 2-9[56]

The first component of the equation (indicated by {} on the left) refers to the surface tension at the wetting perimeter of the particles and the second component (indicated by {} on the right) is essentially a version of the Laplace-Young equation describing

the pressure drop across the gas-liquid interface with respect to the wetted particle area

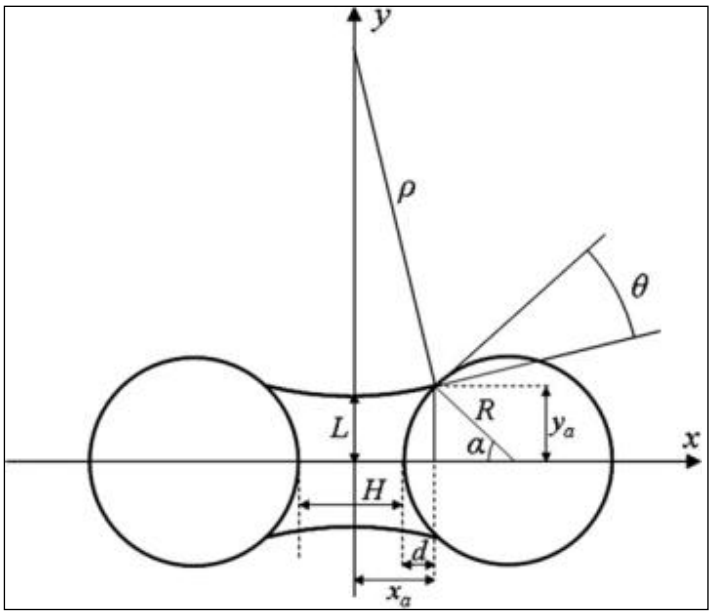

Figure 2-16: Sketch of liquid bridge geometry used for the analysis of capillary forces for coalescence between two partially wetted particles.[56]

Where R = solid particle's radius, α = half-filling angle, θ = wetting angle, ρ = density of the liquid, L = the principal radius of the liquid meniscus, H = surface to surface distance between the solid particles, d = wetted portion of each hemisphere, h = distance between elements of integration used in the calculation of the van der Waals force, r = radius, x_a, y_a = coordinates of the contact point between the solid and liquid profile, γ = interfacial tension between the oil and water phases.

This mathematical relationship demonstrates the effect of capillary forces on the stability of the dispersion system. It also highlights the implication of particle wettability (quantified by the contact angle) on the relatively energy of dispersed particle systems. However, this theory cannot be considered in isolation since in reality, particles are never statically located at the interface but their location depends on the flow and drainage of fluid in the system. Furthermore, the theory

considers the particle-interface interaction but does not take into consideration the significance of inter-particulate interactions such as stabilisation by the electric double layer, dipole dipole repulsion and van der Waals attractions.

2.4.2.1.3 Particle Networks

Particles are known to stabilise emulsions by adsorbing at the droplet interface, creating as a physical barrier to prevent droplet coalescence. At particle concentrations high enough to cover droplets with dense (concentrated) particle monolayers (Figure 2-17a), steric stabilisation dominates since these layers create a 'shell' of particles which hinder droplet coalescence. It was also postulated that at higher particle concentrations, inter-droplet particle networks form, affecting the viscosity of the continuous phase, thus increasing the stability of the emulsion. At lower particle concentrations, an alternative stabilisation mechanism is bridging stabilisation where a bridging monolayer of particles exists between adjacent emulsion droplets (Figure 2-17b). The strong capillary attraction caused by the menisci between particles (Figure 2-17c) stabilises the thin liquid film between the emulsion droplets, thus preventing coalescence. This also explains why emulsions are stable even at dilute particle concentrations when droplet coverage is sparse.

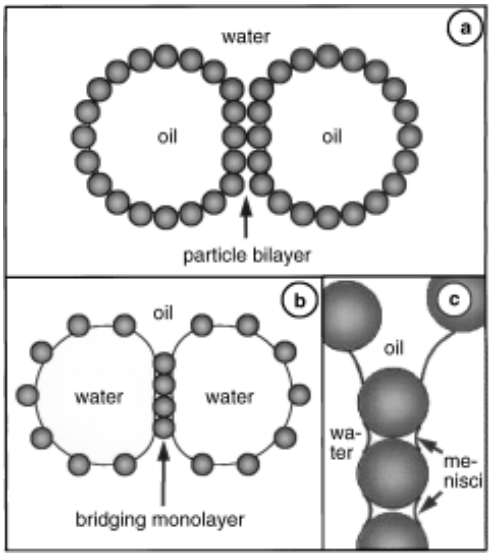

Figure 2-17: Summary of the steric stabilisation mechanisms present in particle-stabilised emulsions including particle bilayer (a), bridging monolayer (b) and capillary attraction due to the menisci around each particle (c).[57]

In comparison to surfactant systems, certain particles do not have much effect on the interfacial tension of oil-water systems. This was first observed by Vignati et al.,[58] who noted that varying the hydrophobicity and concentration of silica particles on iso-octane-water and octanol-water systems had no influence on the interfacial tension. This was later affirmed by Drelich et al.,[59] who observed the same effect using hydrophobic silica particles in a paraffin oil-water system. These reports are in contrast to the theoretical study by Levine et al.,[60] who proposed a strong dependence of interfacial tension on the particle concentration based on the hydrophobicity of the particles. Levine's study was validated by the work of Glaser et al.[61] using amphiphilic particles (Janus particles) which appeared to lower the interfacial tension for n-hexane/water systems. More recently, Kim et al.[62] reported on the behaviour of graphite oxide particles in a toluene-water system and observed a decrease in interfacial tension as the particle concentration increased, at various pHs. From these two schools of thought on the effect of particles on the interfacial tension, it is apparent that the influence of particles on the interfacial tension is

largely dependent on its size, shape and surface chemistry. The more particles resemble amphiphilic surfactant molecules chemically, the more likely they are to have an effect on reducing the interfacial tension when adsorbed at the oil-water interface.

2.4.3 Combining Surfactants and Particles

Another category of emulsions are those stabilised by both surfactant and particulate emulsifiers. The mixing of both particles and surfactants is an important topic in industry since many emulsion formulations available commercially contain both these components.[63] Thus there is continual interest on maintaining the balance between the advantages that surfactants and particulate emulsifiers bring to the emulsion system while controlling emulsion destabilisation and separation by understanding the interactions between surfactant and particles. Generally, surfactants and particle still act as they would in their respective emulsion systems (eg. amphiphilic surfactants adsorb at the oil-water interface to reduce interfacial tension; Particles adsorb almost irreversibly at the oil-water interface and create a mechanical barrier again droplet coalescence). However, since the number of components in the emulsion has increased, the emulsion system is more complex and interactions between particulate and surfactant emulsifiers exert an important effect which has proven to be synergistic or antagonistic, depending on a number of factors which will be revealed in this section.

Weakly aggregated or flocculated particles are formed by the addition and adsorption of surfactants onto the surface of particles or the presence of a salt and proven to be more effective emulsifiers compared to isolated particles. In the first case, addition of a surfactant or polymer was shown by Hassander et al. [64] to encourage the aggregation of Ludox type silica particles. This aggregation of

particles encouraged them to adsorb in a favourable configuration at the oil-water interface, improving the stabilisation of o/w emulsions. In the latter case, the presence of salt in solution is said to be crucial for the formation and stability of particle-stabilised emulsions, as shown in studies by Ashby and Binks et al.,[46] Binks and Lumsdon et al.[43] and Yang et al.[46] In these studies, the addition of salt lowered the zeta potential of the particles, favouring weak particle flocculation which also enhanced emulsion stabilisation. Evidence also exists for the orientation of the particles into a three-dimensional network in the continuous phase due to the addition of salt. This network promotes emulsion stability by increasing the continuous phase viscosity and preventing the coalescence of droplets.

Binks and Rodrigues et al.,[65] performed a systematic study on dodecane-water emulsions stabilised by a cationic surfactant, CTAB, and hydrophilic silica particles exclusively, then mixed the two to study the effects on the type and stability of the final emulsion formed. It was found that a mixture of both surfactant and particulate emulsifiers worked best to stabilise emulsions when there was sufficient surfactant adsorbed on the surface of the particles, causing them to become more hydrophobic. An additional effect of mixing surfactants and particulate emulsifiers in this case was the promotion of particle flocculation which enhanced emulsion stability. In an extension of this idea of enhanced flocculation, Binks and Rodrigues et al. experimented with chargeless alumina-coated silica and an oppositely charged surfactant, anionic SDS, was used together to form stable emulsion droplets. The reasons for this are due to adsorption of the surfactants on the improved flocculation and/or changing the wettability of the particles so they adhere better at the oil-water interface.

Another method was to modify the wettability of a particle, promoting its adsorption at the oil-water interface, therefore encouraging emulsification. This was demonstrated in another study by Binks et al.[66] who found that using both the cationic surfactant CTAB to the hydrophobicity of silica nanoparticles at various pHs. Wang et al.[67] found that adding the lipophilic non-ionic surfactant Span 80 together with Laponite particles improved the long-term stability of emulsions by rendering the particles more hydrophobic which aids in the formation of a three-dimensional network of particle aggregates among emulsion droplets. However, some researchers have also discovered that mixing both surfactant and particle emulsifiers could also destabilise emulsions. Vashisth et al.[68] studied the influence of anionic SDS on the stability of o/w emulsions initially stabilised by partially hydrophobised silica. As the SDS concentration increased above the CMC, particles were displaced from the interface and therefore destabilised. In another study, Drelich et al.[59] also showed that the addition of the surfactant Span 80 to a silica-stabilised w/o emulsion served to displace particles from the interface, destabilising the emulsion. It is also worth mentioning that the order of addition of emulsifier as well as the choice of the phase in which the emulsifier is dispersed into are important factor for the final emulsion stabilisation. Eskandar et al.[69] discovered that the order of adding particles (and phase the particles are added into) had affected the stability of the final emulsion. In particular, he noted that smaller droplet size distribution and stable emulsions were observed for initially surfactant-stabilised emulsions when particles were first added to the oil phase. Whitby et al.[70] also reported that the phase where the surfactant is present is also crucial for emulsion stability. This was attributed to the influence of the surfactant on the extent of particle flocculation which in turn affects the stability of emulsions formed.

2.5 Introduction to Emulsion Templating

There are numerous ways of preparing porous materials but emulsion templating is arguably one of the most versatile and flexible methods to produce bespoke materials for use in advanced scientific materials.[29] In general, the method involves the formation of a w/o emulsion using a continuous (oil phase) containing monomers and a suitable initiator emulsified with a dispersed (aqueous) phase. At the gel point of polymerisation, the continuous phase polymerises 'around' the dispersed aqueous droplets. After polymerisation is complete, the aqueous phase is removed, resulting in a final solid porous structure. Since the dispersed aqueous droplets act as a template for the final porous structure, the process is termed 'emulsion templating'. Different 'types of emulsions could be used in this technique. For example, o/w emulsion templates prepared using oil soluble monomers polymerise to yield beads,[71, 72] water soluble monomers in an o/w emulsion template polymerise to produce hydrophilic porous polymers,[73, 74] low and medium internal phase emulsions (<74 vol.% internal phase dispersed in oil soluble monomers) polymerise to produce porous polymers with lower porosities[75, 76] etc. The focus of this thesis is on the production of hierarchical, highly porous materials achieved by polymerising high internal phase w/o emulsion templates which can be stabilised by surfactants, particulate emulsifiers or a combination of both.

2.5.1 Polymerised High Internal Phase Emulsions (PolyHIPEs)

In the 1980s, polymerised HIPEs or 'polyHIPEs' was patented by Barby and Haq from Unilever PLC.[77] W/o emulsions (an aqueous salt solution dispersed in styrene and divinylbenzene in the oil phase) stabilised by the non-ionic surfactant Span 80 were polymerised to form solid polymers. The terminology used to describe polyHIPE structure is still inconsistent within the community,[78] with some

investigators referring to pores as ‘cells’ or ‘voids’ and pore throats as ‘windows’, ‘interconnects’ or ‘interconnecting holes’. For clarity, a labeled SEM of a typical polyHIPE structure is presented in Figure 2-18 (right) to demonstrate the terminology that will be used throughout this thesis.

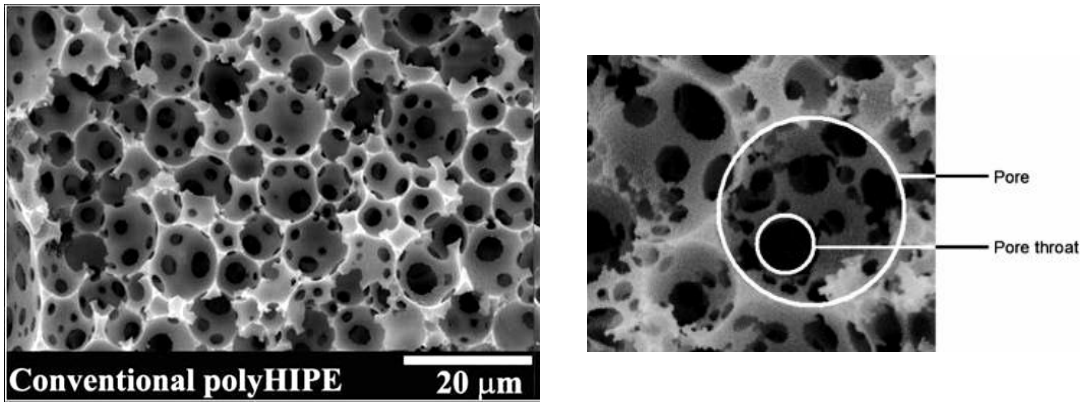

Figure 2-18: SEM of conventional polyHIPE (left)[38] and the terminology used to describe polyHIPE structure (right)[79]

Generally, polyHIPEs have the same porosity as the internal phase volume used to prepare them which can sometimes be as high as 97%[80, 81] It has also been shown that the interconnectivity of the polyHIPE (open or closed cell) is dependent on the surfactant concentration used to prepare the emulsion templates.[81-83] Closed cell porous polymers were synthesised from templates prepared with lower than 5 wt.% of surfactants and open cell or interconnected above 7 wt.%.[83] regardless of the ratio of internal phase used. PolyHIPE pore sizes range from 5 – 100 μm, generaaly, and the interconnecting pore throats are often about a third the size of the pore.[8] A number of studies aimed at investigating the parameters which affect the average pore and pore throat size in polyHIPEs exist in literature. Some suggest that varying the concentration of crosslinking DVB or surfactant in the organic phase has an effect on the average pore and pore throat size.[82] Others point towards the effect of varying the electrolyte concentration on the emulsion and hence final porous

structure.[17] In principle, it remains that these parameters contribute to the stability of the emulsion which dictates the structure of the emulsion at the gel point of polymerisation, hence affecting the final porous structure.

The mechanism for the formation of pore throats remains an on-going discussion in the polyHIPE community. Barby and Haq[77] stated that since surfactants are non-polymerisable and insoluble in the aqueous phase, they aggregate in the polymer phase while the HIPE polymerises, resulting in weakened areas of the polymer film which succumb to mechanical stress and break, forming pore throats. Williams and Wrobleski[83] were the first to observe the relationship between surfactant concentration and the open or close celled nature of the resulting polyHIPE. Increasing surfactant concentrations led to the reduction of emulsion droplet sizes, which made the liquid monomer films that separate adjacent emulsion droplets thinner. When monomers are converted to polymer chains during curing, volume contraction occurs, producing pore throats between adjacent droplets. Cameron et al.[80] investigated the hypothesis of pore throat formation via volume contraction in an insightful cryo-SEM study. Liquid nitrogen frozen sections of HIPE were polymerised over different times and were imaged. The pore throat sizes were then analysed with respect to polymerisation time. It was observed that pore throats form at the gel point of polymerisation, agreeing with the postulate that pore throats form due to volume contraction during the conversion of monomers to polymer. However, the study does not explain the absence of pore throats in polyHIPEs synthesised from emulsion templates stabilised by low surfactant concentrations of <5%. An alternative explanation from Menner et al.,[79] is represented in Figure 2-19. The study proposed that the emulsion phase separates as the solubility of surfactant in the organic phase decreased with polymerisation. Since surfactants aggregate at the oil-

water interface between neighbouring droplets, the separation of the surfactant from the polymerising continuous phase resulted in weakened areas in the solid polymer film.[84] Mechanical rupture of this thin and weakened polymer film is more likely to occur during post-polymerisation processing, which resulted in the formation of pore throats. This mechanism also accounts for why the size of the pore throats decrease with decreasing surfactant concentration.

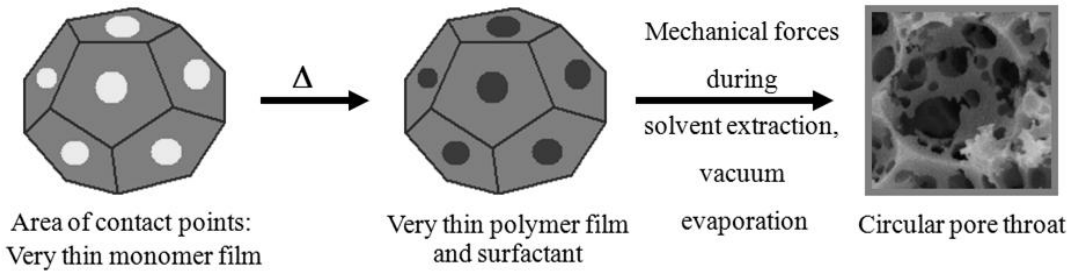

Figure 2-19: Schematic of pore throat preparation as proposed by Menner et al. (Adapted from Bismarck[16])

The presence of interconnecting pore throats makes polyHIPEs open cell and permeable to gases and non-wetting liquids.[76] However, pore throats are essentially gaps or holes in the pore walls, a feature that reduces the load bearing capabilities of the polyHIPEs and negatively affects its mechanical strength. This limits the applicability of polyHIPEs in industry to a large extent. Therefore the challenge still exists to improve the mechanical properties of polyHIPEs without compromising on its high porosity and interconnectivity.

2.5.2 Polymerised-Pickering HIPEs (Poly-Pickering HIPEs)

When Pickering HIPEs are polymerised, poly-Pickering HIPEs are obtained. Poly-Pickering HIPEs are distinguishable from polyHIPEs by their larger average pore size distribution and the lack of interconnecting pore throats, making them closed cell (Figure 2-20, left). In addition to the stability of particle-stabilised emulsion

templates, particulate emulsifiers also double up as reinforcements to the polymer matrix, improving its mechanical properties. A close-up of a pore wall of a typical poly-Pickering HIPE shows particles located at the pore wall (Figure 2-20 right).

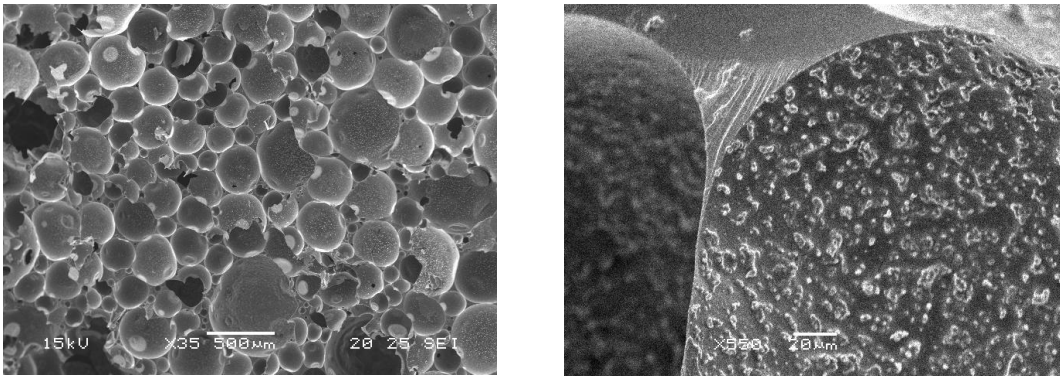

Figure 2-20: SEM of polystyrene-divinylbenzene poly-Pickering-HIPE (left) and higher magnification of the pore walls (right)

Menner et al.[45] first described the successful synthesis of poly-Pickering MIPEs from carbon nanotubes (CNTs). The study described the ability of CNTs to act as 'surfactant-like' particles stabilising the oil-water interfaces in the emulsion during polymerisation. Not only did the presence of CNTs mechanically reinforce the polymer foams, they also imparted conductivity to the materials, creating additional functionality. Colver et al.[85] then reported on the use of Pickering HIPEs stabilised by microgel particles as templates for the production of highly porous poly-Pickering HIPEs. In his study, emulsion templates were centrifuged to 'force' sedimentation of Pickering medium internal phase emulsions (MIPEs) with an original internal phase volume ratio of less than 0.5. The continuous phase that was separated (supernatant) was discarded and the remaining emulsion phase (sediment) polymerised. Although resulting materials were closed cell, the occasional interconnecting pore throats was observed (Figure 2-21), which was attributed to the breakage of the fragile polymer film connecting two adjacent pores.

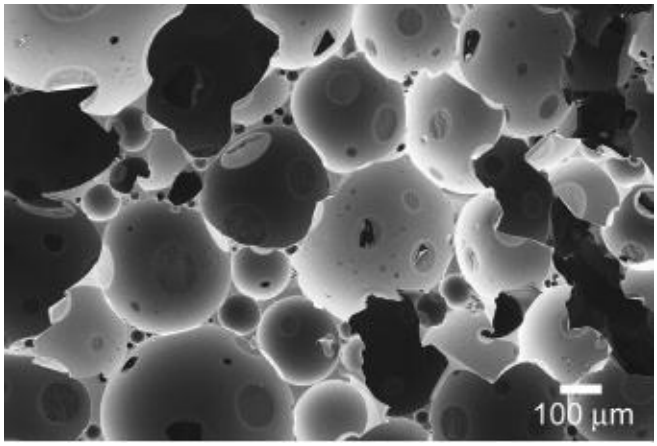

Figure 2-21: Field-emission SEM image of poly-Pickering HIPE monoliths with poly(divinylbenzene)[85]

Menner et al. [45] then reported on the production of poly-Pickering HIPEs directly by polymerising Pickering HIPEs stabilised by low concentrations of titania nanoparticles functionalised with oleic acid (2.5 wt.%). Resulting poly-Pickering HIPEs had larger average pore sizes ranging from 100 – 400 µm[52] when compared with conventional polyHIPEs. There were also no pore throats, rendering them impermeable to gases.

The preparation of poly-Pickering-HIPEs also provided insight into the mechanism behind pore throat formation. In an earlier study, Menner et al.[79] observed a small number of pore throats in SEM images of purely particle stabilised emulsion templated poly-Pickering-HIPEs in addition to what appeared as thinner films covering potential pore throat 'sites' on the pore walls (Figure 2-22). This suggests that although varying the surfactant concentration appeared to affect the size of the pore throats, surfactants are not vital for pore throat formation.

Other studies have since been published on the synthesis of poly-Pickering HIPEs with the aim of imparting additional functionalities to the macroporous polymers via the use of specific particles. Besides the poly-pickering HIPEs produced from

inorganic particles such as CNT, modified titania and silica mentioned earlier, other noticeable ones include the production of poly-Pickering (o/w) HIPEs using polymer nanoparticles such as poly(styrene-methyl methacrylate-acrylic acid) and poly(urethane urea) nanoparticles [86, 87] and magnetic poly-Pickering HIPEs using iron oxide nanoparticles.[88, 89]

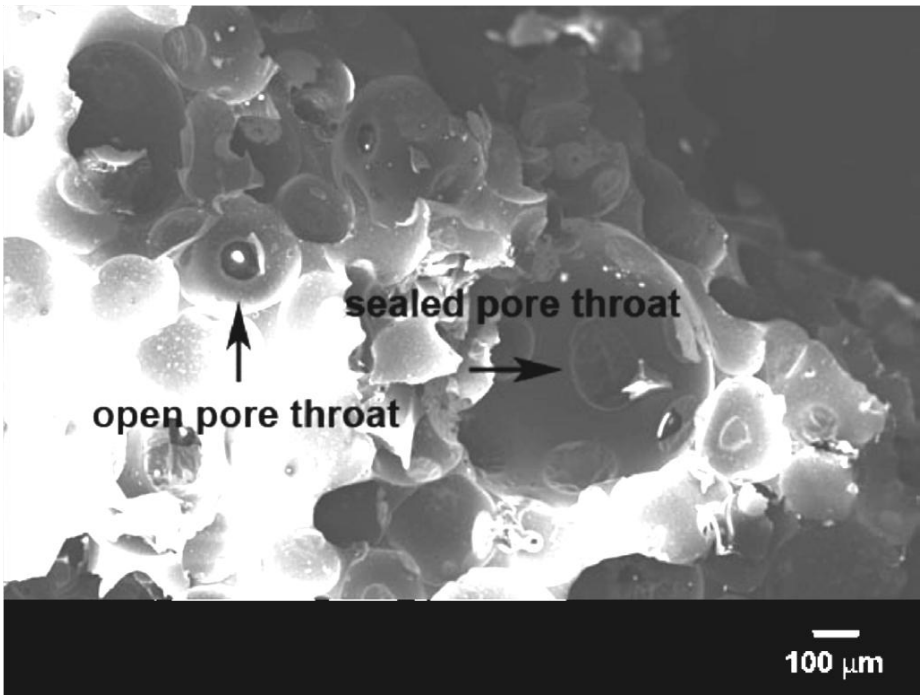

Figure 2-22: Image of Pickering polyHIPE with a partial open pore (image taken from Menner et al.[79])

2.5.3 Hierarchical PolyHIPEs

Currently, the different methods used to synthesise hierarchical polyHIPEs can be summarised into two main strategies: Firstly, using a silica or carbon-containing dispersed phase to prepare a polyHIPE, followed by drying then calcination at temperatures exceeding 600°C. Sintering silica or carbon at such high temperatures promotes a condensation reaction to produce powder-like solids with very high surface areas. This can be seen in work by Zhang et al,[90] where porous polyacrylamide (PAM)/silica composite beads of about 1.5mm in diameter were

prepared via sedimentation polymerisation of o/w/o HIPEs. The beads were immersed in inorganic precursor solutions for a period of time, then filtered, washed and dried. They were then calcined to obtain a silica 'skeleton' which had very high surface areas and large macropores of about 10μm, on average. The method was also applied to transition metal oxide beads such as alumina and titania beads. Following a similar principle, Li et al.[91] used poly (N-isopropylacrylamide) or PNIPM-based microgel particle to stabilise HIPEs containing silica nanoparticles. The oil and water components were removed via freeze-drying resulting in a porous material which were consolidated by calcination at temperatures up to 1400°C. Besides achieving the conventional polyHIPE pore size of (10 – 30 μm) and pore throats (3 – 5 μm), the microgel particles initiated the formation of nanosized (80nm) pores across the pore walls, creating a hierarchy of pores across three length scales. In another study, Gross et al.[92] produced hierarchical macroporous foams with mesoporous carbon xerogels using emulsion templates which contained silicon oil as the internal phase and a resorcinol-formaldehyde precursor solution as the continuous (external) phase. The precursor solution was cured to obtain a gel which was dried, and underwent solvent exchange to remove water. Finally, it was pyrolysed to obtain the hierarchical product of foams with mesopores with an average of 5 – 8nm diameter and macropores with an average of 0.7 – 2.1 μm interconnected by macropores with an average diameter of 0.18 – 0.53 μm.

The second strategy for creating hierarchical polyHIPEs involves the use of a 'double templating' technique where two colloidal templates with different dimensions are used in synergy to produce hierarchically organised materials. This was presented by Carn et al.,[93] who produced a porous inorganic monolith using a direct emulsion template to generate a macro-scale pore structure and a micellular

template at the nano-scale to produce pores of a much smaller size range. Whilst Schwab et al.[94] induced swelling in polyHIPE precursors, then hypercrosslinked the resulting polymeric network, producing a secondary micro- structure in the pore walls. This massively increased the BET surface area, which when superimposed with the macro- structure of the polymeric monolith, produced a hierarchical poyHIPE structure.

The production of hierarchical pores in the macro- range via emulsion templating is a topic that has not been explored hence far. As described before, current work on hierarchical porous polymers is focused on achieving high surface areas by manipulating synthesis conditions to produce secondary pores in the nano- range in addition to pores in the micro- and macro- range. This creates a rougher texture in the walls of the porous polymer, as seen in Figure 2-23. Also this increases the surface area by two to three orders of magnitude. The highly convoluted pore wall has drawbacks as resulting materials are delicate and unable to withstand much mechanical stress. An alternative definition of hierarchy proposes considers the arrangement of pores in natural porous materials. It is believed that a hierarchical macroporous arrangement is believed to improve the resulting physical properties of macroporous polymers.

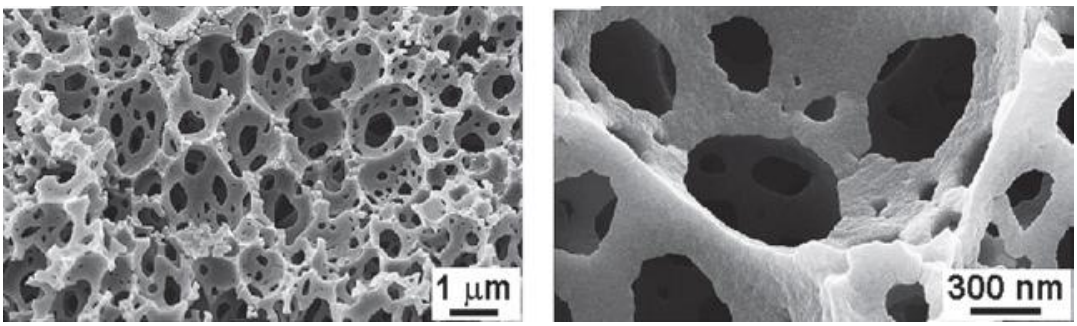

Figure 2-23: SEM images of poly (4-vinylbenzene chloride- divinylbenzene) polyHIPEs showing the largely mono-modal pore size distribution (left) and at higher magnification, a 'roughened' polymer wall due to hypercrosslinking (right) which increases the surface area.[94]

3 Hierarchical Polymerised High Internal Phase Emulsions Synthesised from Surfactant-Stabilised Emulsion Templates

3.1 Summary

In building construction, structural elements, such as lattice girders, are positioned specifically to support the main frame of a building. This arrangement provides additional structural hierarchy, facilitating the transfer of load to its foundation while keeping the building weight down. The same concept was applied when synthesising hierarchical open celled macroporous polymers from High Internal Phase Emulsion (HIPE) templates stabilised by varying concentrations of a polymeric non-ionic surfactant. These hierarchical poly(merised)HIPEs have multimodally distributed pores, which are efficiently arranged to enhance the load transfer mechanism in the polymer foam. As a result, hierarchical polyHIPEs produced from HIPEs stabilised by 5 vol.% surfactant showed a 93% improvement in Young's moduli compared to conventional polyHIPEs produced from HIPEs stabilised by 20 vol.% of surfactant with the same porosity of 84%. Finite Element Method (FEM) was used to determine the effect of pore hierarchy on the mechanical performance of porous polymers under small periodic compressions. Results from FEM showed a clear improvement in Young's moduli for simulated hierarchical porous geometries. This methodology could be further adapted as a predictive tool to determine the influence of hierarchy on the mechanical properties of a range of porous materials.

3.2 Introduction

Macroporous polymers are a unique class of materials valued for their high porosities, light weight and low densities. Some methods currently used to produce macroporous polymers include physical or chemical blowing or foaming (frothing),[95-97] solvent casting and particle leaching,[98] thermally induced phased separation (TIPS),[6] the use of super critical fluids (including supercritical carbon dioxide)[99-101] and emulsion templating. Of these methods, emulsion templating is particularly notable for its simplicity and versatility. Since the (liquid) emulsion takes the shape of its casting mould, it is possible to create different forms of macroporous polymers ranging from solid porous monoliths[102] and thin membranes[2] to micrometre-sized beads[103]. Furthermore, pore morphologies of emulsion templated macroporous polymers are tuneable by varying the emulsion composition.[27] Due to their interconnectivity, post polymerisation functionalisation of emulsion templated macroporous polymers is also possible.[104] As a result of these traits, there is growing interest to develop emulsion templated macroporous polymers for various engineering applications. To date, studies have been carried out to explore the use of emulsion templated macroporous polymers as microbioreactors,[105] catalyst supports,[106] ion exchange modules[107] and scaffolds for tissue engineering[108] or setting retarded cements[109, 110] to name just a few. The production of macroporous polymers (using hydrophobic monomers) via emulsion templating involves the use of water-in-oil (w/o) emulsions. W/o HIPE templates consist of an internal phase made up of an aqueous electrolyte solution, dispersed in a continuous phase containing monomer(s) and crosslinker(s), initiator and emulsifier(s), which can be surfactants, particles[52, 85, 111, 112] or a combination of both.[113] Since the arrangement of droplets in the emulsion acts as template for the

final macroporous polymer structure at the gel point of polymerisation, the technique is thus termed emulsion templating.

In this study, high porosity open-celled porous materials were prepared by polymerising HIPEs stabilised solely by surfactants. HIPEs are emulsions that have an internal phase volume of greater than 74 vol.%, a value equal to the maximum packing ratio of monodispersed spheres, after which the aqueous droplets dispersed in the continuous phase are modelled, just before they start to deform.[8, 114, 115] Using a suitable initiator, the monomers in the continuous phase polymerise around the aqueous internal phase droplets. After vacuum drying, a solid, highly porous material called poly(merised)HIPE is produced. Conventionally, polyHIPEs have average pore sizes ranging from 5 to 100 μm interconnected by spherical pore throats that are about a third the size of a pore in diameter.[114-116] Pore throats in the polyHIPEs make them interconnected or open-celled and, therefore, permeable to gases and/or liquids. However, as the size of pore throats (and interconnectivity) increase while porosity and average pore size remain constant, the load bearing capability of highly porous polyHIPEs will also decrease since pore throats are essentially gaps or discrepancies in the pore wall.[117] Therefore, the challenge is to improve the mechanical properties while maintaining the high porosity and interconnectivity of polyHIPEs.

Previous studies aimed at improving the mechanical properties of polyHIPEs include the use of nanofillers[75, 118-121] to reinforce the polymer matrix, thereby improving the crush strength and Young's modulus of resultant macroporous polymer composites. Another approach was the use of alternative monomers that polymerised into tougher, stronger polymers; for instance, hydrophilic 1-vinyl-5-amino [1,2,3,4] tetrazole was polymerised with N, N'-methylenebisacrylamide as a crosslinker using dodecane as the dispersed phase.[122] Poly(dicyclopentadiene), which has a large number of double

bonds, hydroxyl, hydroperoxy groups and carbonyl groups, was used to prepare polyHIPEs with high Young's moduli as the functional groups facilitate covalent and hydrogen bonding to improve the cross-linking density of the polymer.[123] More recently, Luo et al.[117] utilised living radical polymerisation to produce polyHIPEs to increase the homogeneity of styrene polymerisation, which resulted in improved overall mechanical strength of these polyHIPEs.

An alternative strategy to improve the mechanical integrity of polyHIPEs is to mimic the hierarchical structure of naturally occurring strong highly porous materials, such as wood and spongy bone tissue.[10] These natural porous materials consist of structural units which differ in size and are arranged to provide optimal conditions for effective load transfer.[10] Drawing inspiration from this, the term 'hierarchy' in this study refers to a pore structure with a multi-modal pore size distribution, arranged such as to improve the mechanical properties of the final porous product. This definition of hierarchy was first referred to in an earlier study discussing macroporous polymers produced from emulsions stabilised simultaneously by both particles and surfactants, which showed a clear influence of multimodal pore size distribution on mechanical properties.[113] This is in contrast to other reports on 'hierarchical' polyHIPEs, which contain pores in the nanometre range and are, therefore, highly textured with high surface areas. A major drawback of these highly intricate 'hierarchical'-type materials is the inability to withstand much mechanical stress,[90-94] making them too delicate for any real application.

Encouraged by our earlier findings,[113] a methodology to produce new hierarchical polyHIPEs by polymerising HIPE templates solely stabilised by surfactant is presented in this paper. By optimising the surfactant content and the emulsification process, the droplet size distribution of resulting emulsions were controlled to

produce hierarchical polyHIPEs. Since the concept of 'structural hierarchy' is often applied to the architecture of roofs and bridges, which consist of lattice girders positioned strategically to transfer load to the foundation while maintaining a relatively light design,[124] it was further extrapolated that the hierarchical arrangement of pores in our materials would facilitate effective load transfer during compression, improving the crush strength and Young's modulus without compromising interconnectivity. A finite element method (FEM) analysis was used on simulated 2D geometries of hierarchical porous materials to validate the favourable effect of hierarchy on the mechanical properties of porous materials.

3.3 Experimental

3.3.1 Materials

Styrene (≥ 99%), divinylbenzene (DVB; 80 vol.% *m*- and *p*- divinylbenzene) and calcium chloride dihydrate ($CaCl_2 \cdot 2H_2O$) were purchased from Sigma Alrich (Gillingham, UK). The non-ionic polymeric surfactant Hypermer 2296 was kindly supplied by CRODA (Wirral, UK). The free-radical initiator α,α'-azoisobutyronitrile (AIBN) was purchased from Camida (Tipperary, Ireland). Deionised water was used for the preparation of the aqueous phase and for the purification of polyHIPEs. All chemicals were used as received.

3.3.2 HIPE Preparation

The aqueous internal phase (80 vol.% with respect to total emulsion volume, 40 ml) containing $CaCl_2.2H_2O$ (5 g/L, 0.034 M) as electrolyte to suppress Ostwald ripening was added drop wise to the continuous phase consisting of styrene (50 vol.% with respect to total monomer volume, 5 ml) and DVB (50 vol.% with respect to total monomer volume, 5 ml). Various concentrations of surfactant Hypermer 2296 and 1

mol-% of the radical initiator AIBN (with respect to monomers) was also added. Whilst the aqueous phase was being added, the mixture was stirred by a glass paddle rod connected to an overhead stirrer maintained at a constant speed of 500 rpm. After all the aqueous phase had been added, the stirring speed was increased to 2,000 rpm for 30 s (or 5 min where stated) to obtain a homogeneous emulsion. Five emulsions (two of each) containing 0.75 w/vol%, 1 w/vol.% (**DS1**), 2 w/vol.% (**DS2**), 5 w/vol.% (**DS5**), 10 w/vol.% (**DS10**) and 20 w/vol.% (**DS20**) of surfactant with respect to monomer volume were prepared for polymerisation. It was assumed the surfactant was removed during the purification step and, therefore, the volume of surfactant was not taken into consideration for the calculation of the internal phase volume.

3.3.3 PolyHIPE Preparation

Emulsions were transferred immediately after preparation to 50 ml free-standing polypropylene centrifuge tubes (Falcon™ tubes), sealed and polymerised in a convection oven for 24 h at 70°C. The resulting polyHIPEs were removed from their tubes and washed with deionised water followedF by acetone to remove all unreacted monomers, surfactants, residual $CaCl_2.2H_2O$ and other impurities. The polyHIPEs were then dried in a vacuum oven at 100°C to constant weight.

3.3.4 Characterisation of PolyHIPEs

3.3.4.1 Density and Porosity

Helium displacement pycnometry (Accupyc 1330, Micrometrics Ltd, Dunstable UK) was used to measure the matrix or skeletal density (ρ_m) of the polymer foams. The envelope or foam density (ρ_f) was measured using an envelope density analyser

(GeoPyc 1360, Micrometrics Ltd, Dunstable, UK) and the percentage porosity (P) was then calculated using equation:

$$P\ (\%) = \left[1 - \frac{\rho_f}{\rho_m}\right] \cdot 100$$

Equation 3-1

At least six samples from two repeat samples of each of the polyHIPEs **DS1** to **DS20** were analysed to obtain statistically relevant data.

3.3.4.2 Pore Structure, Pore and Pore Throat Dimensions

The microstructure of the polyHIPEs was studied by imaging fracture surfaces using a SEM (Hitachi High Technologies, S3400N VP SEM) at an accelerating voltage of 5 kV. Prior to SEM, approximately 0.5 cm^3 of each dry sample was fixed onto an aluminium stub using a carbon sticker and gold coated at 20 mA for 60 s (Scan Coat Six SEM Sputter Coater, Edwards Ltd., Crawley, UK) to ensure electrical conductivity. Images were taken from fractured surfaces taken from the top, middle and bottom sections of a sample in order to account for the variations in pore morphology due to droplet coalescence and sedimentation. Since the differences in pore and pore throat size distributions for **DS1** to **DS20** are minimal, the pore and pore throat dimensions (at least 250 from each polyHIPE) were analysed using the imaging software ImageJ. The data is processed into frequency distribution curves and when necessary, fitted using the Gauss Amp function (Equation 3-2) to determine the average pore throat size (x_c):

$$y = y_0 + Ae^{-\frac{(x-x_c)^2}{2\omega^2}}$$

Equation 3-2

where x is the pore throat size (μm), y the count, y_0 the offset, x_c the average pore throat size (μm), ω the width of the distribution and A the amplitude of the distribution.

3.3.4.3 Surface Area

Surface areas of the polyHIPEs were determined from nitrogen adsorption isotherms (77K) using the Brunauer-Emmet-Teller (BET) model using a surface area analyser (Micrometrics ASAP 2010, Micromeritics, Dunstable, UK). Prior to gas adsorption, contaminants were removed via a 'degassing' step where approximately 200 mg of each polyHIPE was heated to 110°C in glass sample cells overnight.

3.3.4.4 Gas permeability

A pressure rise technique was used to measure the gas permeability using a custom built system reported earlier.[76] PolyHIPEs characterised using this technique are required to be strong enough to withstand the shear forces exerted by a N_2 pressure difference of up to 1.4 bar required for measurements. PolyHIPEs disks of approximately 15 mm in diameter were cast in sealed samples cells to avoid cross flow around the edges. Gas pressure was kept low on one side of the porous medium while at the other side, a constant higher pressure was maintained. Gas flowed through the pores of the sample from the high to the low pressure side where it was collected in a vessel with a fixed, known volume. The rates of pressure rise were measured and the data points used to determine the viscous permeability of the polyHIPEs using the equation:

$$K = \frac{Q_2 p_2 L}{\Delta p A} = \frac{V\left(\frac{dp_2}{dt}\right)L}{p_1 A} = \frac{k}{\mu} p_m + \frac{4}{3} K_o \sqrt{\frac{8RT}{\pi M}}$$

Equation 3-3

where Q_2 is the volumetric flow rate on low pressure side, p_2 the downstream pressure, L the sample length, A the sample cross sectional area, Δp the pressure difference across sample, V the known vessel volume, T the time; k the viscous permeability; p_m the mean pressure; p_1 the gas inlet pressure; μ the gas viscosity; K_o the Knudsen permeability coefficient; R the gas constant, T the temperature and M is the molar mass of Nitrogen gas. Measurements were performed on two different samples for each polyHIPE and repeated six times per side of each sample.

3.3.4.5 Mechanical Properties

Compression tests were carried out at room temperature using the Lloyds instruments universal testing machine (Lloyds EZ50, Lloyds Instruments Ltd Fareham, UK) equipped with a 50 kN load cell at an extension rate of 1 mm/min. The plates were sprayed with a dry polytetrafluroethylene (PTFE) spray (ROCOL, West Yorkshire, UK). A minimum of five cylindrical pieces with a diameter of 25.3 ± 0.3 mm and height of 10.5 ± 0.4 mm were cut from each formulation. Absolute care was taken to ensure that the sample surfaces were parallel. The samples were compressed until the thickness was reduced to approximately 50% of its original value. The Young's modulus was then determined from the slope of the initial linear elastic region in the stress/strain plot and the crush strength was computed from the maximum compressive strength of the foam sample at the end of the initial linear elastic region, normalised with respect to the cross sectional area.

3.3.5 Simulated Porous Microstructures and Determination of Young's Modulus Using Finite Element Method (FEM)[1]

A simulation study was carried out to investigate the effect of hierarchical pore arrangement on the Young's modulus of macroporous materials. To begin, 2D images representing the porous structures of our polyHIPEs were generated using a packing algorithm developed with the Processing Software Version 2.0 Beta 3. This algorithm was designed to position circles (representing pores) into an illustrative 100 x 100 μm^2 box. Each circle was modelled by a spring-and-dashpot force model considering elastic repulsion forces and a viscous damping force but no frictional forces. Elastic repulsive forces, represented by areas where circles overlapped, were minimised. Using pore size distribution curves obtained for **DS1** to **DS20** determined by SEM image analysis (Section 3.3.4.2) as a reference, twenty randomly generated microstructures with a constant porosity of $80 \pm 1\%$ were analysed for each pore structure (namely Geometry 1 to Geometry 5). These pore geometries (representing the pore structures of polyHIPEs **DS1** to **DS20**) produced using this 'packing algorithm' were then fed into the software Abaqus using Python to script a code that generated output data via the Finite Element Method (FEM). The code was specifically designed to solve two-dimensional (2D) plane strain problems with periodic boundary conditions for a mesh of individual units that make up the pore structures derived earlier. An average Young's modulus of 3.2 GPa and Poisson's ratio of 0.33, both values extracted from literature for (bulk) crosslinked polystyrene[125, 126] were used as input parameter for polymer properties. Using FEM,

[1] This work described in this section and all associated results are mainly the work of a research collaborator, Dr Pedro Baiz Villafranca, Department of Aeronautics Imperial College London.

small periodic compressive displacements were applied to the top edge of each unit, keeping the bottom edge fixed in the vertical direction. Horizontal displacements were allowed, except at the bottom right corner to avoid rigid body motion (Figure 3-1). Nodal degrees of freedom for the right and left edges of each unit were scripted to move by the same amount in the analysis. The total reaction load output from this finite element system was used to compute the overall Young's modulus associated with these pore structures, assuming that they obeyed Hooke's Law, i.e. a linear relation between stress and strain for small strains.

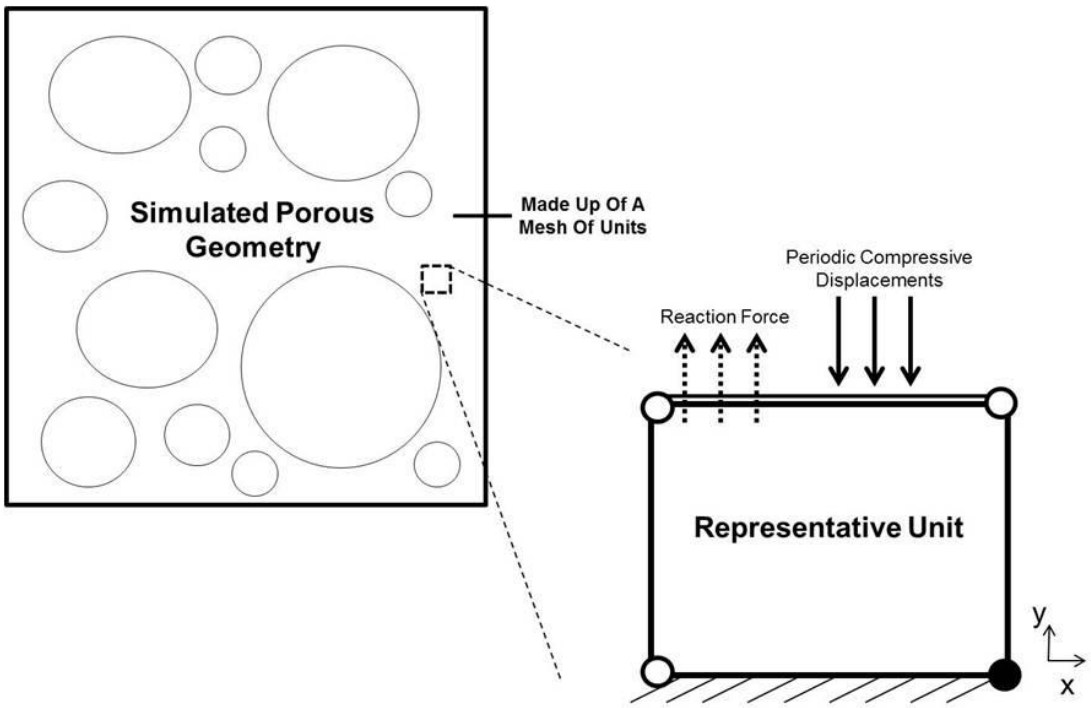

Figure 3-1: Schematic representing FEM analysis

3.4 Results and Discussion

Our group previously showed that HIPEs with an internal phase volume ratio of 74%, prepared with a surfactant concentration of 20 vol.% with respect to monomer volume and a stirring time of 10 min at 2,000 rpm resulted in viscous emulsions, which after polymerisation and purification resulted in polyHIPEs with an average

pore size of 4.9 ± 1.9 μm and a porosity of 82%.[76] It was hypothesised that adjusting the surfactant concentration and the energy input during emulsification, i.e. the stirring time, would influence the droplet size distribution and resulting pore sizes. Thus, to produce pore hierarchy, our strategy was to vary the surfactant concentration and emulsification time independently to investigate how this affected the rate of droplet break up and coalescence. By first keeping the stirring rate constant and the surfactant concentration below 20 vol%, the rate of droplet breakup was expected to be lower and the rate of droplet coalescence higher, resulting in a multi-modal droplet size distribution. It was found that the lowest concentration of surfactant used to prepare homogenous emulsions, which remained stable during polymerisation was 0.75 w/vol.%. These HIPEs polymerised to yield polyHIPE monoliths, which were interconnected by pore throats (Figure A0-1). At this surfactant concentration, emulsion droplets underwent rapid sedimentation resulting in a large pore size gradient, with pores excess of 2 mm (even after stirring for 10 min), making the polyHIPEs unsuitable for mechanical testing. Therefore, emulsions stabilised by 1 w/vol.% surfactant were the next lowest surfactant concentration that produced polyHIPEs that could be successfully cut into intact pieces for mechanical testing. Surfactant concentration was further varied from 1 to 2, 5, 10 and 20 w/vol.% to study its effects on the resulting pore morphology of polyHIPEs.

Optical microscopy images of HIPEs with an internal phase volume ratio of 75% stabilised by 1 w/vol.% surfactant showed a polydisperse droplet distribution when emulsified under said conditions for 10 min (Figure 3-2). When the two phases were emulsified for a shorter period of 30 s, the result was an even broader droplet size distribution (Figure 3-3) as the emulsion consisted of a greater number of droplets, which were much larger than the ones observed in Figure 3-2, interspersed with

smaller droplets. This establishes that besides surfactant concentration, a shorter emulsification time is another factor that further encouraged the formation of emulsions with a very broad droplet size distribution.

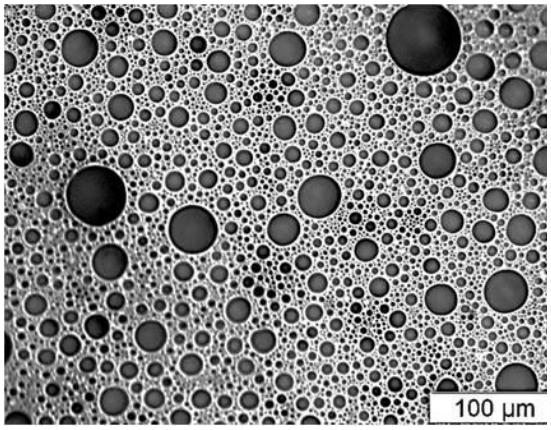

Figure 3-2: Optical micrograph of a HIPE stabilised with 1 w/vol.% stirred for 10 min

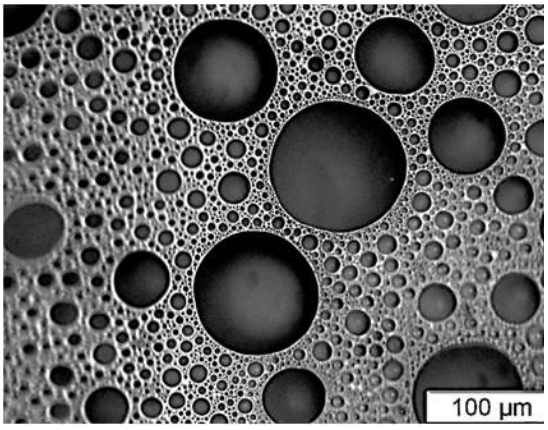

Figure 3-3: Optical micrograph of a HIPE stabilised with 1 w/vol.% stirred for 30 s

These emulsion templates polymerised into white solid macroporous monoliths **DS1**, **DS2**, **DS5**, **DS10** and **DS20**, respectively. The polymerised specimens could be handled without breaking easily but were chalky due to the high crosslinking density; a result of the high DVB content. Skeletal (1.10 ± 0.03 g/cm^3) and envelope (0.18 ± 0.01 g/cm^3) densities were constant for all polyHIPEs despite the increasing surfactant concentration used to stabilise the HIPE templates. This indicated that the parasitic surfactant was removed from the macroporous polymers during post-polymerisation purification and drying. Porosities were constant at 84 ± 1 % since all specimens were prepared from emulsion templates with the same internal phase volume. The average porosity measured was higher than the internal phase volume used (80 vol.%) due to the presence of unreacted monomers.

SEM micrographs representative of the microstructures of polyHIPEs **DS1** to **DS20** are presented in Figure 3-4.

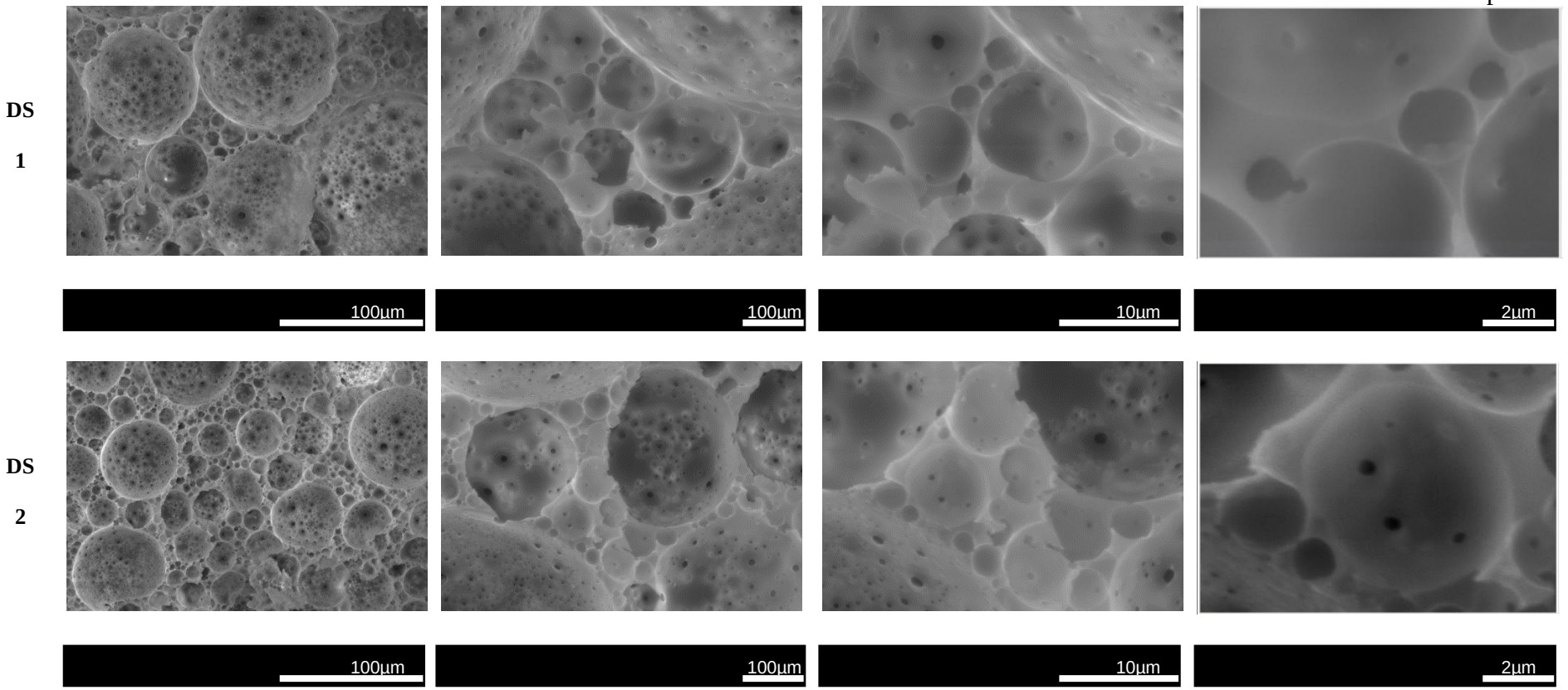
DS
1
100µm
100µm
10µm
2µm
DS
2
100µm
100µm
10µm
2µm

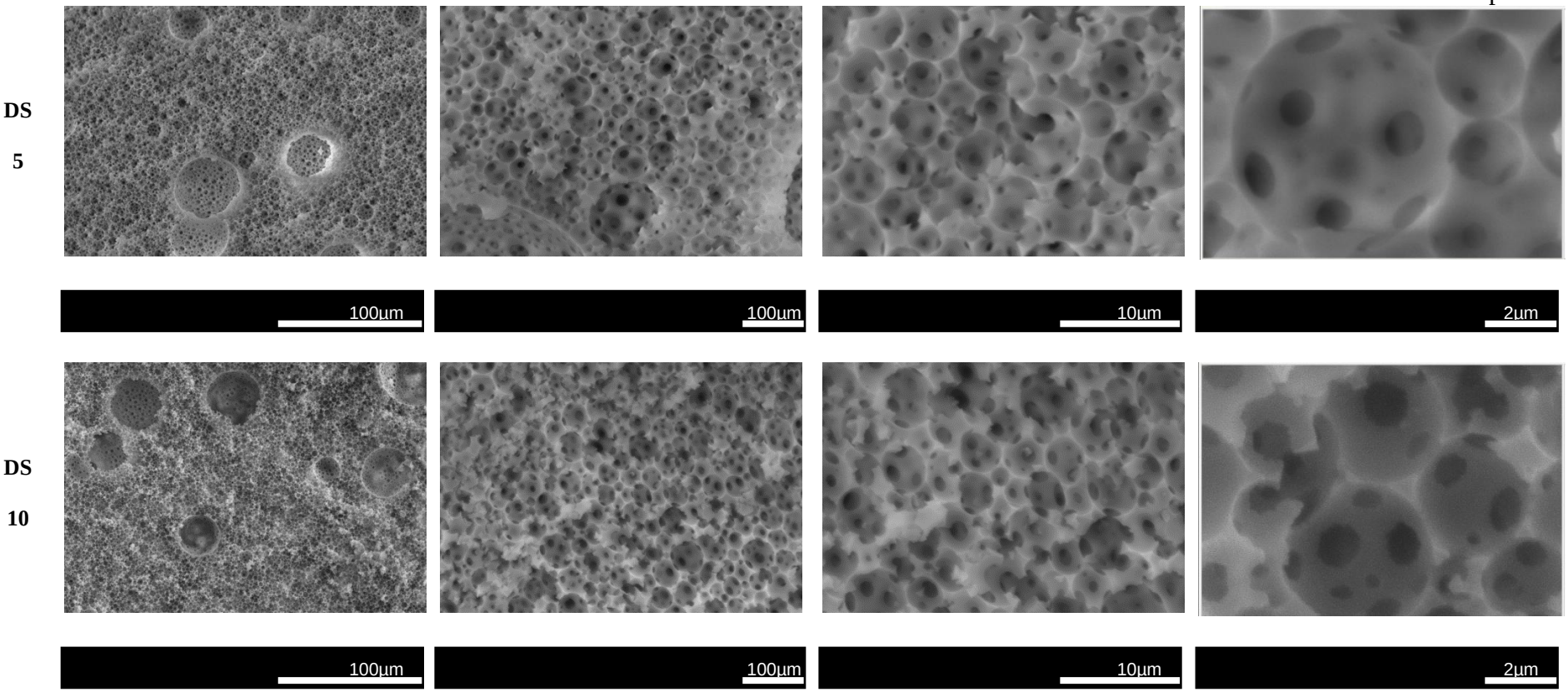
DS
5
100µm
100µm
10µm
2µm
DS
10
100µm
100µm
10µm
2µm

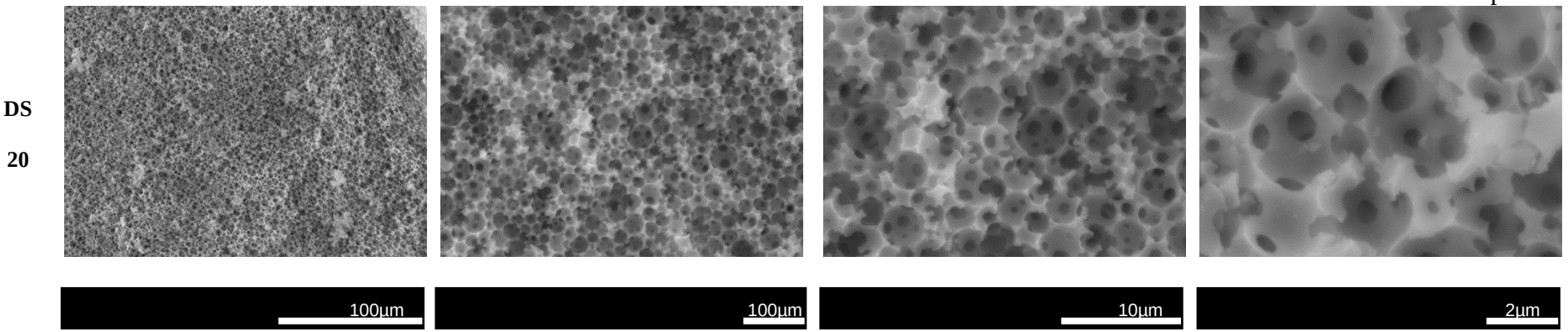

Figure 3-4: SEM micrographs of polyHIPEs synthesised from emulsion templates stabilised with surfactant concentrations ranging from 1 w/vol.% (DS1), 2 w/vol.% (DS2), 5 w/vol.% (DS5), 10 w/vol.% (DS10) and 20 w/vol.% (DS20). SEM images are representative of the pore morphology across the entire polymer monolith.

The pore size distributions of all the macroporous polymers synthesised are presented in Figure 3-5 and the BET surface areas are tabulated in Table 3-1. To clearly visualise any macro-scale hierarchy (defined earlier as macroporous polymer with a multimodal pore size distribution with optimally arranged pores) observed in these structures, Figure 3-4 and Figure 3-5 are discussed together.

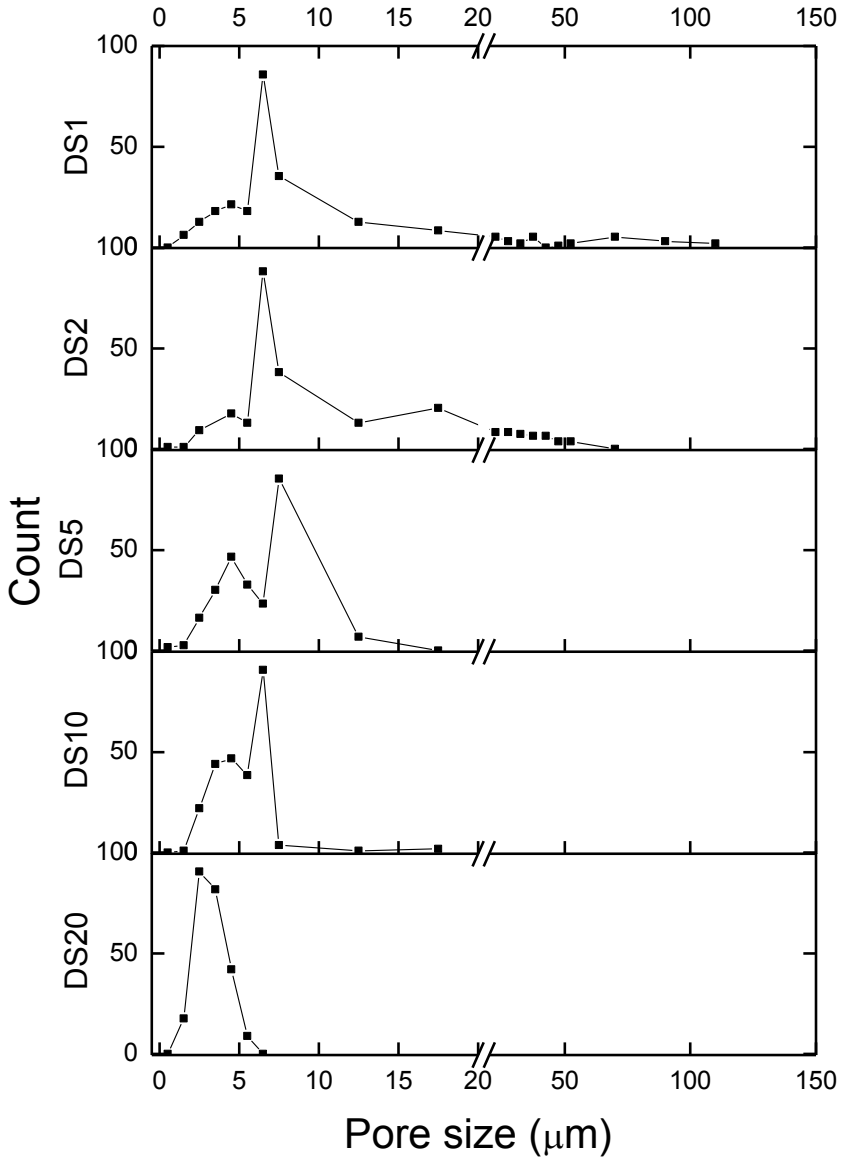

Figure 3-5: Pore size distribution of DS1 to DS20.

The pore size distributions for **DS1** and **DS2** look similar since they both have largest peaks at approximately 6.4 μm. However, **DS1** has a higher proportion of small pores that lie in the range from 0 and 5 μm when compared to **DS2**, which also explains its larger BET surface area when compared to **DS2**. **DS1** also has a generally wider pore size distribution, with a broader, flatter right tail and a peak at approximately 125 μm, which is not seen in **DS2**. In **DS2**, a greater proportion of pores were in the range of 12.5 to 50 μm when compared to **DS1**. In **DS5**, the pore size distribution curve could be described as bimodal, with peaks centred around 4.7 μm and 7.7 μm. The percentage of pores that fall between 0 and 5 μm in **DS5** is at least 20% higher compared to **DS1** and **DS2**, also accounting for its larger BET surface area. **DS10** also has also a bimodal pore size distribution, with a downward shift of peaks (compared to **DS5**) to 4.1 μm and 6.4 μm as the increased surfactant concentration in the HIPE template from which the polyHIPEs were synthesised favours the stabilisation of smaller droplets. This increase in the proportion of smaller droplets also correlates with the increase in BET surface area for **DS10** compared to **DS5**. In contrast to **DS1** to **DS10**, the pore structure observed in **DS20** is that of a typical polyHIPE, with pores that are more uniform in size (Figure 3-4). The pore size distribution for **DS20** is monomodal, with a distinct peak at approximately 2.6 μm (Figure 3-5). Hence **DS20** is not classified as polyHIPE with a hierarchical pore structure. **DS20** also has the largest surface area as it has the smallest pores out of all the samples.

From higher magnification SEM images taken of **DS1** to **DS20** (Figure 3-4), it is apparent that all polyHIPEs synthesised are open celled with pores being interconnected by pore throats. The pore throat distribution curves of **DS1** to **DS20** are presented in Figure 3-6.

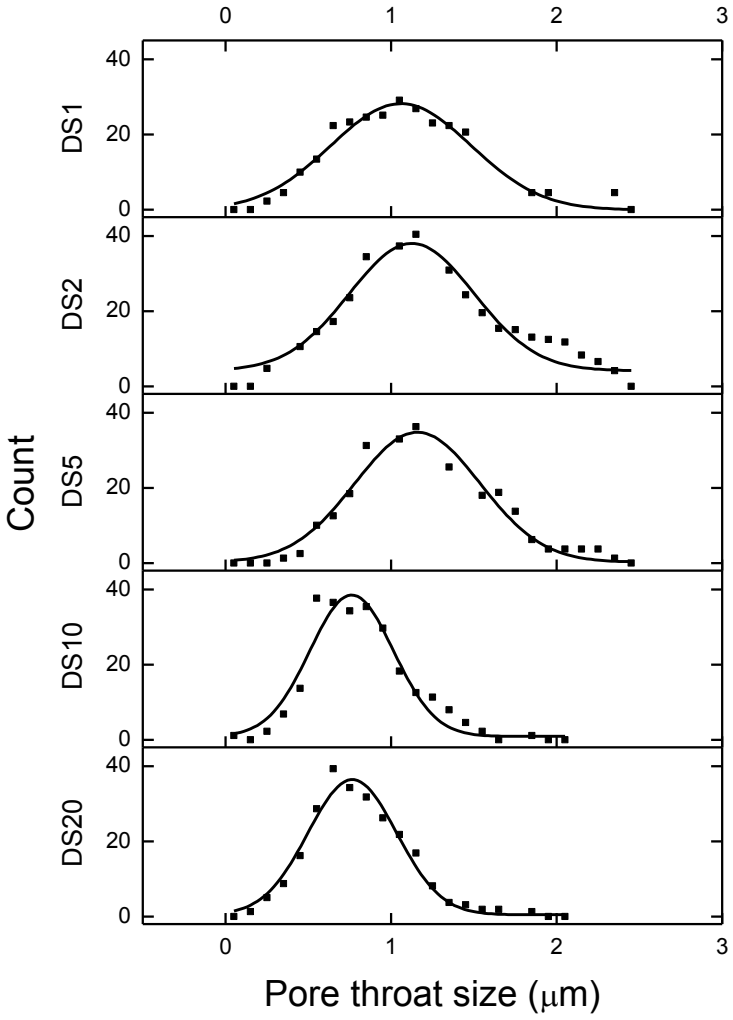

Figure 3-6: Frequency of occurrence of pore throat sizes for DS1 to DS20. A GaussAmp function is fitted to them to calculate the mean pore throat size.

Even though some of the polyHIPEs prepared in this study have a hierarchical pore arrangement, the distribution of the pore throat diameters is monomodal. This does not come as a surprise as all larger pores are always surrounded by smaller pores, which ultimately limits the size of the pore throats. Average pore throat sizes were determined from the GaussAmp fit and summarised in Table 3-1 (parameters used for fitting are tabulated in Table A0-1). Generally, the pore throat size distribution becomes narrower with increasing surfactant concentration used to stabilise the HIPE templates. The average pore throat size increases slightly between **DS1** to **DS5**

before decreasing to its smallest value in **DS10** and **DS20**. Although much is up for dispute on the mechanism for pore throat formation in polyHIPEs, it is believed that as the continuous phase of the surfactant stabilised emulsion polymerises, the solubility of the surfactant in the polymerising organic phase decreases, causing the surfactant to form a separate phase in the polymer-rich monomer phase in the thinned film regions (usually the region found when droplets are pressed together) of the polymerising HIPE. This creates fragile areas in the contact points between the droplets. After polymerisation, these fragile areas break open, leaving behind pore throats.[48] In hierarchical polyHIPEs, the pore throat diameter is limited by the size of the internal phase droplets in the liquid HIPE template that are packed in between larger droplets, as it is more likely for large droplets to come into contact with smaller droplets than with other large droplets. Since the proportion of smaller pores in **DS1** is higher compared to **DS2** (Figure 3-5) the average area of contact between two pores in **DS1** would also be smaller, therefore the average pore throat diameter for **DS1** is smaller than **DS2**. The proportion of smaller pores increased with increasing surfactant concentration used to stabilise the HIPE templates from **DS2** to **DS10** (Figure 3-5), thus the average contact areas between adjacent pores also decreases, resulting in smaller average pore throat diameters. It is worth noting that the average pore throat diameter of **DS10** and **DS20** is almost identical because the size of the smaller pores in **DS10**, which limits the size of pore throats formed, is the same as the average pore size in **DS20**.

Table 3-1: Summary of surface area, average pore throat diameter and gas permeability of DS1 to DS20.

Sample ID	Surface area (m^2/g)[#]	Average[%] pore throat diameter d_{pt} (μm)*	Gas Permeability κ (mD)[#]
DS1	3.59 ± 0.02	1.06 ± 0.02	261 ± 69
DS2	2.28 ± 0.02	1.13 ± 0.02	98 ± 22
DS5	4.86 ± 0.02	1.16 ± 0.02	105 ± 54
DS10	5.95 ± 0.01	0.76 ± 0.02	44 ± 11
DS20	7.64 ± 0.12	0.77 ± 0.01	32 ± 21

[%] based on Gaussian distribution * standard error over 250 counts [#] standard deviation

Gas permeability was used to characterise the interconnectivity of these polymer foams. In general, gas permeability is limited by the smallest pore throat in a series of interconnected pores.[76] **DS1** has the highest gas permeability, which suggests that it has the largest limiting pore throat diameters of all polyHIPEs prepared (Table 3-1). Gas permeability decreases by about 60% from **DS1** to **DS2** as the limiting pore throat size decreases. Since **DS2** and **DS5** have very similar pore throat size distributions, they are likely to have approximately the same limiting pore throat diameter and hence similar gas permeability. Gas permeability drops by a further 60% in **DS10** as the proportion of small pores increases dramatically (Table 3-1), decreasing the limiting pore throat diameter. Since **DS10** and **DS20** also have an almost identical pore throat size distribution (and average pore throat value), the limiting pore throat diameter for the two samples are likely to be the same, accounting for the similar gas permeability measured.

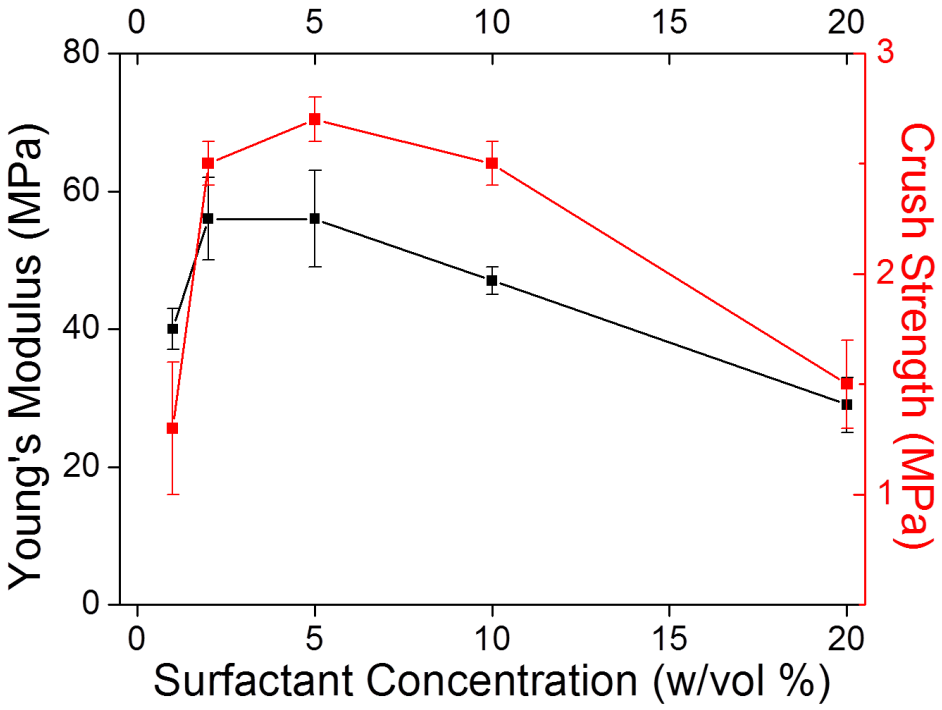

Figure 3-7: Summary of Young's modulus and crush strength of (hierarchial) poly(styrene-co-divinylbenzene)HIPEs.

From earlier work, it is known that the pore and pore throat size distribution play an important role in determining the overall ability to resist longitudinal compressive forces.[113] In this study, since the densities and porosities of **DS1** to **DS20** remain constant, the influence of pore size hierarchy on the overall mechanical properties of the polyHIPEs can be further validated.

DS1 has the highest interconnectivity, determined by analysing the gas permeability, which as mentioned earlier, is related to the size of the limiting pore throat diameter and a factor that affects the homogeneity of the pore walls and greatly affects the load bearing ability of the macroporous polymer.[117] This explains why **DS1** has the lowest crush strength and Young's modulus amongst all hierarchical polyHIPEs (Figure 3-7). Compared to **DS1**, **DS2** had almost twice the crush strength and the Young's modulus increased by 40% (Figure 3-7) as **DS2** had lower interconnectivity

compared to **DS1**. The packing arrangement of pores in **DS2** is also more effective at withstanding compressive loads. As the surfactant concentration increased in the HIPE templates from which **DS2** to **DS5** were synthesised, the polyHIPEs still had the same interconnectivity but **DS5** had a distinctive bimodal pore size distribution in contrast to the monomodal pore size distribution observed for **DS2**. The pore hierarchy of **DS5** appears to be an optimal balance between large and small pores, improving the load transfer mechanism of the porous microstructure under compression. As interconnectivity decreases from **DS5** to **DS10**, the Young's modulus of **DS10** decreased by about 16% and the crush strength dropped to the same strength as **DS2**. This is a result of the less apparent pore hierarchy observed in **DS10**. **DS20** exhibited a further 40% drop in crush strength and Young's modulus compared to **DS10**, despite having the lowest interconnectivity. This indicates that the reduced average pore size and the absence of pore hierarchy (distinctive monomodal pore size distribution) has a profound effect on the mechanical integrity of **DS20** as it is the macroporous polymer with the lowest mechanical properties in this series. It is also clear that the influence of pore hierarchy on the mechanical properties surpasses that of the pore throat size distribution in this system of macroporous polymers. It is worth mentioning here that the mechanical properties of various macroporous materials are known and might indeed by better but is not relevant to prove our concept of hierarchy for this study.

A simulation study was designed to determine if a hierarchical arrangement of pores could indeed result in increased mechanical properties of porous materials. The first step was to create 2D porous microstructures based on experimentally determined pore size distributions (Figure 3-5) using a 'circle packing algorithm'. 'Snapshots' of representative geometries are displayed in Figure 3-8**.**

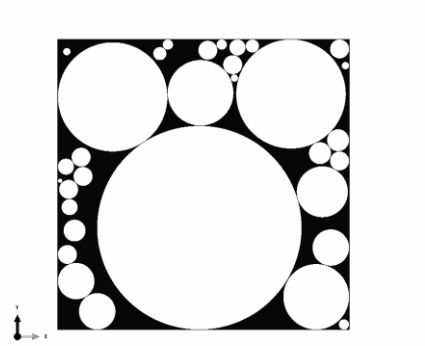

Geometry 1 (modelled after **DS1**)

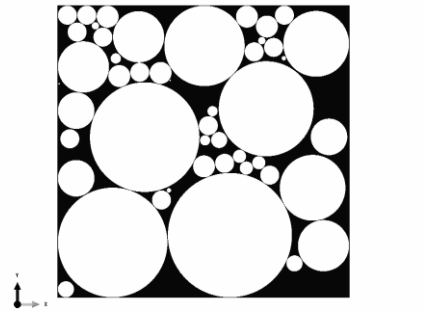

Geometry 2 (modelled after **DS2**)

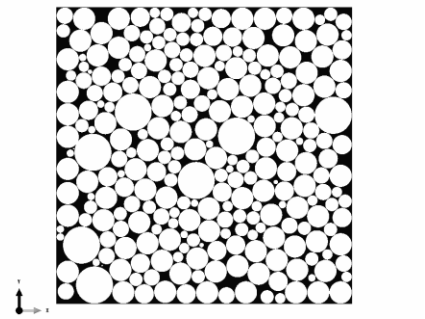

Geometry 3 (modelled after **DS5**)

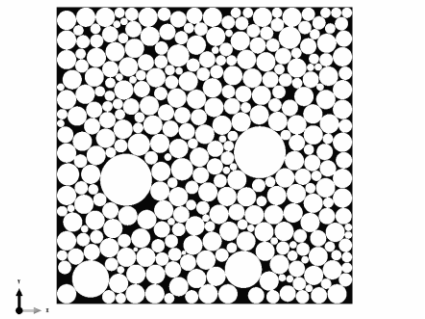

Geometry 4 (modelled after **DS10**)

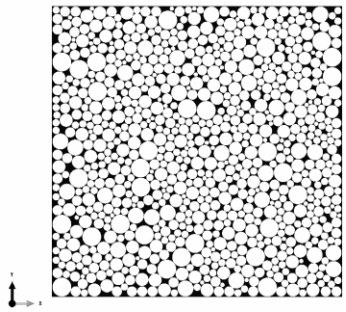

Geometry 5 (modelled after **DS20**)

Figure 3-8: Porous geometries generated to describe DS1 to DS20 (each side of the square corresponds to 100 µm)

To generate output data demonstrating the effect of pore hierarchy on the mechanical properties of these porous polymers, simulated geometries based on pore size distributions measured for **DS1** to **DS20** were fed into a Python-scripted model which generated reaction loads using FEM. There are some assumptions and limitations of the model that should be considered when analysing the results. Firstly, a 2D computational model was assumed, which although may not seem realistic, however it is believed to be an efficient and acceptable method to provide qualitative comparisons with our measured data. Also, for this complex system of equations to converge, maximum porosities were limited to 80 ± 1%, which is slightly lower than porosities measured from actual samples (Table 3-1). Furthermore, these 2D microstructures were designed to only account for the pore arrangement (hierarchical vs. non-hierarchical) and do not yet consider the effect of pore throats on the overall mechanical properties. Bearing these abovementioned assumptions and limitations of the model in mind, a qualitative approach was used to interpret the data generated. Reaction loads (output) were used to calculate Young's moduli, which were then normalised with the Young's modulus of the bulk polymer (3.2 GPa) to obtain

representative relationships) which effectively demonstrate any dependency of the pore geometry's elastic response on changes in porous morphology.

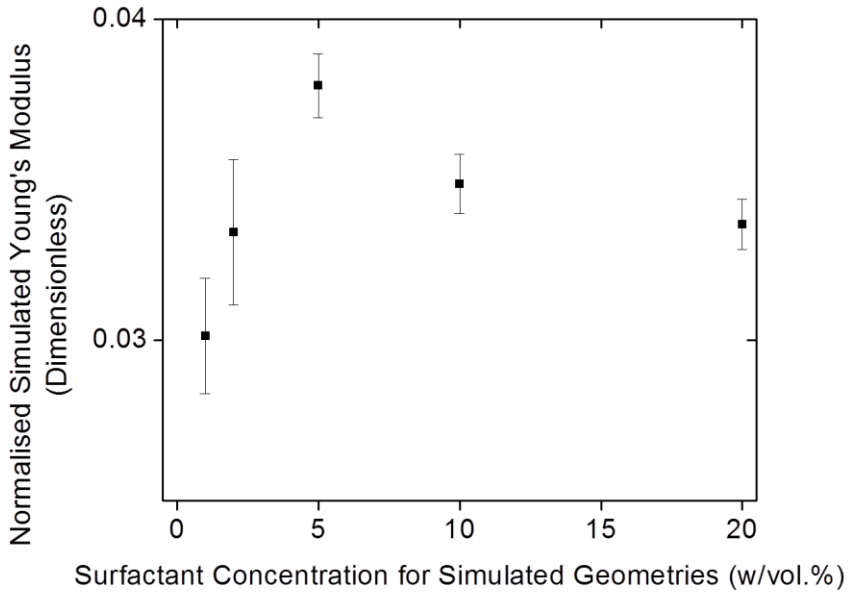

Figure 3-9: Qualitative comparison between normalised Young's moduli obtained from compressing 2D porous geometries (Geometries 1 to 5) generated to represent HIPE templates with varying concentrations of surfactant (DS1 to DS20).

The mean and standard error of 20 simulated Young's moduli per sample are displayed in Figure 3-9. Geometry 3 (**DS5**) has the highest computed (20% variation from the lowest value) Young's modulus compared to the rest of the geometries. This proves that a significant improvement of elastic properties is observed by introducing hierarchy into the pore structure of porous materials with constant porosity. Therefore, this preliminary simulation study shows that the hierarchical pore structure of **DS5** (Geometry 3) does indeed provide favourable mechanical properties; it had the highest Young's modulus out of all the polyHIPEs prepared, a result which is in line with our experimental observations.

3.5 Conclusions

Inspired by hierarchical porous structures in nature, hierarchical polyHIPEs were synthesised from surfactant stabilised emulsion templates. Hierarchical polyHIPEs are defined as having a multimodal pore size distribution, arranged in an optimal packing configuration. This hierarchical arrangement of pores is comparable to the role of lattice girders positioned specifically to provide structural hierarchy in building construction. The girders facilitate the transfer of load to the foundation while keeping the overall building light. Highly porous and lightweight hierarchical polyHIPEs were found to be permeable yet mechanically stronger than conventional, polyHIPEs with a monomodal pore size distribution but the same porosity. Using simulated 2D porous geometries modelled after hierarchical and non-hierarchical polyHIPEs prepared in this study, their corresponding elastic behaviour was predicted qualitatively using FEM. Small compressive displacements were applied to individual units making up the entire porous geometry and the resulting reaction load was analysed. This preliminary simulation study showed a clear beneficial influence of pore hierarchy on the Young's modulus of macroporous polymers, encouraging further investigation to determine a more accurate predictive tool that could elucidate any load transfer mechanics responsible for the improvement. Lessons learnt from our study will aid future, 3D simulations that could allow us to study the load transfer mechanisms of both hierarchical and non-hierarchical porous structures, explaining in greater detail the dependency of pore hierarchy on the mechanical properties of porous materials.

4 Macroporous Polymers with Hierarchical Pore Structure from Emulsion Templates Stabilised by Both Particles and Surfactants

4.1 Summary

Natural porous materials, such as wood, bamboo and spongy bone consist of individual structural units, which are hierarchically arranged to optimise mechanical properties such as strength and toughness. This was the inspiration to create synthetic macroporous polymers with enhanced compressive strength at a fixed porosity, by creating a hierarchical pore arrangement using emulsion templating. It was shown that hierarchical poly(merised) High Internal Phase Emulsions (HIPE) can be synthesised from HIPEs stabilised simultaneously by particles and a surfactant. In these HIPEs, surfactant stabilised and particle stabilised water droplets coexist. Upon polymerisation of the minority oil phase, macroporous polymers with a hierarchical pore structure are produced. The polymer foams reported in this chapter have characteristics of both, poly-Pickering-HIPEs with predominantly large closed pores and conventional polyHIPEs, commonly with interconnected small open pores. An improvement of the mechanical properties of reported hierarchically structured macroporous polymers at equal porosity was observed. This was attributed to a more efficient packing of pores in a configuration that improves mechanical strength despite the presence of interconnecting pore throats. Moreover, the permeability of the hierarchically structured polyHIPEs exceeds those measured for conventional polyHIPEs made surfactant only stabilised HIPEs.

4.2 Introduction

Porous materials found in nature such as wood, bamboo and spongy bone consist of individual structural units, which are hierarchically arranged to optimise mechanical properties such as strength and toughness.[10, 127] It is our aim to enhance the physical properties, such as the compressive strength of synthetic polymer foams by creating a hierarchical pore arrangement, inspired by what is observed in nature. Since emulsion templating is an effective way to produce synthetic polymer foams with tailored properties, it is a viable method to produce hierarchically arranged macroporous polymer, an area that remains unexplored.

High internal phase emulsions (HIPEs) are concentrated mixtures of liquid droplets dispersed in another liquid medium, defined by a minimum droplet volume fraction of 74 vol-%.[80] HIPEs are commonly stabilised by surfactants although particles can also be used.[45] Water in oil (w/o) HIPEs, which consist of monomers and crosslinkers [19] as continuous phase and an electrolyte solution as internal phase, can be polymerised. The emulsion structure at the gel point of polymerization is a template for the pore structure of the resultant macroporous polymer, the so-called polyHIPE, after the internal phase is removed. Typically, a surfactant stabilised HIPE results in a conventional polyHIPE after polymerization and has pore sizes between 1 and 20 µm [116] interconnected by pore throats, which are around 20-50% of the pore diameter.[80] PolyHIPEs have porosities up to 95% [81-83] and are permeable to gases and wetting liquids [76] since they are highly interconnected. In contrast to conventional polyHIPEs, so called poly-Pickering-HIPEs, which are obtained from particle stabilised emulsion templates, have larger closed-cell pores ranging from 200 to 700 µm.[52]

There have been attempts to make hierarchical polyHIPEs, which can be summarised into a few main strategies, one of which is to create conventional polyHIPEs, with rougher, textured pore walls, increasing its overall surface area. This is done by adjusting the level of the crosslinker divinylbenzene or adding inert porogens such as toluene and petroleum ether.[116] Zhang et al. synthesised porous emulsion-templated polymer/silica composite beads and then calcined them to produce the desired degree of hierarchy in pore size with by forming both meso- and macro-pores.[90] Carn et al. [93] created hierarchical porosity by synthesising inorganic monoliths using an emulsion template at the macroscale and micellular templates at the mesoscale, while Schwab et al. [94] swelled a polyHIPE precursor and then generated microporosity via hypercrosslinking of the polymers, massively increasing the specific surface area of the macroporous polymer. To synthesise interconnected porous silica materials with macro- and nano-pore dimensions, Li et al. used silica-stabilised HIPE droplets and microgel particles to stabilise emulsion templates, producing hierarchical materials with high surface areas.[39, 91] Although hierarchical nano-, micro- and meso-porous polyHIPEs have high surface areas due to the presence of very small pores in the walls of the polymer foam, they are considerably weaker than conventional polyHIPEs synthesised from surfactant-stabilised emulsion templates.

Based on the enhanced properties of the naturally occurring hierarchical macroporous polymers,[10] it is believed that the use of emulsion templates to generate macro-scale hierarchy in polyHIPEs could result in enhanced mechanical strength. We, therefore, focus on the creation of macroporous polymers with hierarchical pore structures by combining open and closed pore structures found in conventional polyHIPEs and poly-Pickering-HIPEs, respectively. Evidence exists for synthetically produced hierarchical macroporous polymers to have improved mechanical

performance, just like their naturally occurring counterparts,[10] improving their viability as a material in practical applications where mechanical strength and interconnectivity are important,[128] such as tissue engineering scaffolds, solid support for reactions, adsorbents and electrodes.

4.3 Experimental

4.3.1 Preparation of HIPEs and PolyHIPEs

Oleic acid modified titania particles were first dispersed in a 7:5 mixture of styrene (Sigma Aldrich Gillingham, UK) and PEGDMA (Cognis, Southampton UK) using a homogenizer (Kinematica Luzern, CH) at 15000 rpm for 10 min to make up the monomer phase. Free-radical polymerization was initiated by 1 mol% (with respect to monomers) of α-α'-azobisisobutyronitrile (AIBN, Camida, Belgium). To this suspension, the surfactant Hypermer B246SF (Uniqema Wirral, UK) dissolved in styrene and the aqueous internal phase of 0.27 M $CaCl_2.2H_2O$ (Sigma Aldrich Gillingham, UK) were both added simultaneously drop-wise under gentle stirring at 500 rpm. Resulting HIPEs were free-flowing and could be easily transferred to standing Falcon™ tubes to be polymerised at 70°C for 24 h. After polymerization, the resulting solid macroporous monoliths were cut from the tubes and purified by Soxhlet extraction to remove the parasitic surfactant. Macroporous polymers were then first dried in a convection oven at 110˚C for 24 h then in vacuum at 110˚C until a constant weight was reached.

4.3.2 Characterisation of PolyHIPEs

SEM images of Au-coated macroporous polymers were taken with a Hitachi Science Systems, S-3400N VP SEM. The macroporous polymers were embedded in epoxy resin (Araldite 2020), cured and sliced using a Reichert Jung Ultramicrotome into

about 60 nm thick sections. These sections were placed on a holey copper grid and TEM images taken using the JEOL 2000 TEM operating at 200 kV. Skeletal density was measured using a helium pycnometer (Accupyc 1330, Micrometric Ltd., Dunstable, UK) and the foam density and porosity of the macroporous polymer were measured using a foam density analyser (Geopyc 1360, Micrometrics Ltd., Dunstable UK). Gas permeability was measured with a home-built permeability apparatus using the pressure rise technique.[76] Mechanical properties were measured according to BS ISO 844 using Lloyds EZ50 (Lloyds Instruments, Fareham, UK). The Young's modulus was determined from the initial linear slope of the stress-strain plot.[118]

4.4 Results and Discussion

In order to create hierarchical macroporous polymers, Pickering stabilised emulsions and surfactant stabilised emulsions were combined by using particulate emulsifiers and a traditional surfactant simultaneously, a novel method of preparing hierarchical macroporous polymer foams which has not been reported before.

To understand the influence of each emulsifier on the resultant emulsion templated hierarchical macroporous polymers, either the surfactant concentration (**M2** to **M5**) or the particulate concentration (**M3**, **M6** and **M7**) was varied but the volumes of all other components (monomers and aqueous phase) were kept constant. Titania particles modified with 3.5 ± 0.1 wt% oleic acid [52] were used as particulate emulsifiers and, therefore, dispersed in a 7:5 mixture (by volume) of styrene and poly-ethylene glycol dimethylacrylate (PEGDMA). Styrene is a commonly used monomer in polyHIPE preparation, while PEGDMA is a flexible crosslinker used to reduce the brittleness of the resulting polymer.[45] The non-ionic polymeric surfactant

Hypermer B246SF was used as a traditional molecular emulsifier. However, it was not dissolved in the monomer phase but added at the same time as the aqueous phase (77 vol% 0.27M $CaCl_2 \cdot 2H_2O$) into the monomer phase. This emulsion preparation technique results in significant differences in the structural morphology and physical properties of the resultant macroporous polymers which are unique when compared to conventional polyHIPEs and poly-Pickering-HIPEs as well as a previously reported study from the same group.[52] Furthermore, a solely particle stabilised Pickering HIPE containing 0.8 w/v% particles with respect to continuous phase was prepared as control (**M1**). The particle and surfactant concentrations of the emulsion templates used to prepare the polyHIPEs are summarised in Table 4-1.

The foam densities and porosities of the control poly-Pickering-HIPE **M1** and the hierarchical macroporous polymers **M2** to **M7** are identical within error at 0.25 ± 0.02 g/cm^3 and 79 %, respectively, since all the emulsion templates contained the same internal phase volume. The skeletal densities of samples in Series 1 (**M1** – **M5**), where only the surfactant concentrations within the emulsion templates were varied, are constant at 1.145 g/cm^3 since the polymer composition is the same. Within Series 2, (**M3**, **M6** – **M7**), the surfactant concentration was kept constant at 4.2 w/v % (with respect to the continuous phase) but the particle concentration was increased from 0.8 to 4.2 w/v% (with respect to the continuous phase). This causes the skeletal density to increase from 1.143 g/cm^3 (**M3**) to 1.193 g/cm^3 (**M7**) as titania particles contribute to the density of the polymer matrix.

Table 4-1: Summary of the porosity (P), skeletal density (ρ_{SD}), gas permeability (k), crush strength (σ) and Young's modulus (E) of macroporous polymers synthesised from emulsion templates stabilised simultaneously by various particle (c_p) and surfactant concentrations (c_s):

Macroporous Polymer	c_p [w/v%][a]	c_s [w/v%][b]	P [%]	ρ_{SD} [g/cm^3]	k [D]	σ [MPa]	E [MPa]
M1	0.8	0.0	78±1	1.144±0.001	0	1.7±0.1	12±2
M2	0.8	0.8	79±1	1.149±0.007	0.67±0.14	3.6±0.1	27±2
M3	0.8	4.2	78±1	1.143±0.004	1.16±0.63	2.9±0.1	22±2
M4	0.8	8.4	79±1	1.151±0.008	0.97±0.51	3.0±0.1	23±2
M5	0.8	17	79±1	1.137±0.004	0.13±0.04	0.9±0.1	5±2
M6	2.5	4.2	78±1	1.175±0.009	0.81±0.29	3.6±0.4	19±2
M7	4.2	4.2	79±1	1.193±0.004	1.16±0.49	3.2±0.4	21±2

Percentage of particles [a] and surfactant [b] with respect to continuous phase. Highlighted rows **M3**, **M6** – **M7** summarise the properties of macroporous polymers from emulsion templates increasing particle concentration at constant surfactant concentration.

Table 4-2: Summary of x_1, x_{T1} and N_1, which are the average pore size, average pore throat size and number of pore throats in the smaller pores typical for conventional polyHIPEs and x_2, x_{T2} and N_2 which are the average pore size, average pore throat size and number of pore throats per bigger pore typical for poly-Pickering HIPEs.

Macroporous Polymer	x_1 [µm]	x_{T1} [µm]	N_1	x_2 [µm]	x_{T2} [µm]	N_2
M1	0	0	0	297±21	0	0
M2	17±1	4.3±0.2	2.1±0.2	399±17	0.9±0.1	2.0±0.8
M3	13±1	5.1±0.5	8.4±1.0	395±28	1.4±0.5	3.2±0.4
M4	17±1	5.8±0.7	15.8±1.4	304±18	1.3±0.3	2.8±0.4
M5	13±1	3.0±0.4	16.8±1.3	0	0	0
M6	29±4	8.7±1.3	4.7±1.7	207±10	5.1±1.4	3.4±0.8
M7	32±6	8.9±1.1	4.5±1.2	161±7	6.4±1.7	3.4±0.5

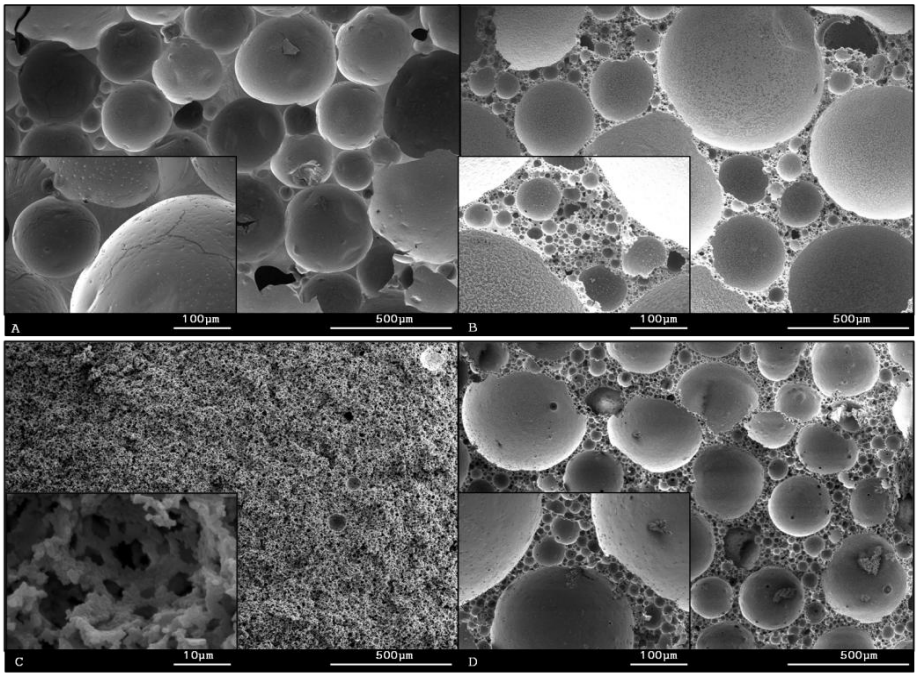

Figure 4-1: SEM of hierarchical macroporous polymers. A: Closed-cell poly-Pickering-HIPE M1. B: M3 with hierarchical structure consisting of distinctly open and predominantly closed-cell pores. C: M5 with conventional polyHIPE structure of small pores and numerous interconnecting pore throats. D: M6 with hierarchical structure consisting of distinctly open and predominantly closed-cell pores. Note that M3 is representative for M2 – M4 and M6 is the representative image for M6 – M7.

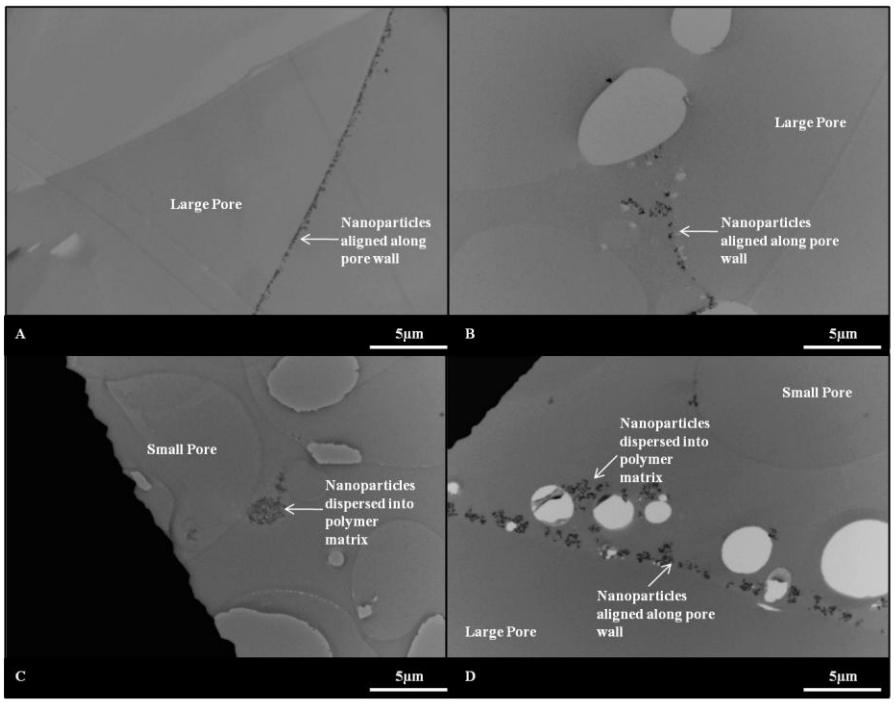

Figure 4-2: TEM of sections taken from hierarchical macroporous polymers. A: M1, B: M3, C: M5, D: M6.

Statistical analysis was carried out on SEM images of all macroporous polymers to obtain average pore and pore throat sizes, which are summarised in Table 4-2. Control **M1** prepared from a solely particle-stabilised emulsion template has a typical impermeable poly-Pickering-HIPE morphology (Figure 4-1A) consisting of large, closed cell pores with pore sizes broadly distributed around 297 μm (Table 4-2); none of the pores are interconnected via pore throats. The TEM image of control poly-Pickering-HIPE M1 (Figure 4-2A) shows a layer of particles situated near the boundary of a large pore and no particles can be seen inside the pore walls, demonstrating that particles adsorbed at the oil-water interface of Pickering emulsion droplets, which when polymerised, form the large, closed cell pores.

The addition of varying amounts of surfactant as co-emulsifier to the emulsion templates of **M2 - M4** leads to the formation of a hierarchical pore structure as can be seen in Figure 4-1B. The morphology of **M2 - M4** is characterized by large, predominantly closed cell pores (> 100 μm) typical for poly-Pickering-HIPEs, which are surrounded by highly interconnected small pores (< 20 μm), characteristic for conventional polyHIPEs. Since the microstructure of the emulsion templated macroporous polymer reflects the structure of the emulsion at its gel point [129] It was concluded that particle and surfactant-stabilised water droplets co-existed in the emulsion template, which upon polymerization of the continuous phase gave rise to macroporous polymers with hierarchically arranged pores. In the TEM image of **M3** (Figure 4-2B) one can see a section of a large pore whose walls are partially covered by particles, some dispersed particles within the polymer matrix forming the pore walls. However, there are also small pores which do not contain any particles. This indicates particle and surfactant stabilised droplets coexisted in the corresponding emulsion template. It is worth noting that surfactant also adsorbs onto the particles,

changing its wetting properties, causing some particles to migrate into the polymer matrix as observed.

The smaller of the hierarchically arranged pores have pore sizes of about 15 µm and are interconnected via pore throats; the number of pore throats per pore as well as the pore throat size increases with increasing amount of surfactant added to the emulsion template (Table 4-2 x_1, x_{T1}, N_1). It is worth noting that although the large poly-Pickering-HIPE-type pores observed for **M2** to **M4** appear to be predominantly closed-cell, they do in fact have on average 2.7 pore throats per pore (N_2), which are about 1.2 µm (x_{T2}) in diameter. This is due to the dense packing of small surfactant-stabilised emulsion droplets around large particle stabilised droplets in the templates, which leads to the thinning of the monomer phase films in the area of close contact between neighbouring surfactant and particle stabilised droplets Although the mechanism of pore throat formation is not fully understood, sufficiently thin films between neighbouring droplets and the presence of surfactant are the key requirements.[130] Therefore, pore throats form in **M2 - M4** upon polymerisation of the emulsion templates or purification/drying of the resulting macroporous polymers. **M2** has the lowest permeability at 0.67 D as it has the smallest x_{T1} and x_{T2} and the least amount of pore throats per pore. The increase in permeability to 1.16 D for **M3** is due to the increase in the pore throat sizes (x_{T1} and x_{T2}) as well as the number of pore throats per pore (N_1 and N_2) caused by the increasing amount of surfactant in the emulsion template. However, the permeability decreases to 0.97 D for **M4** although the pore throat size and especially the number of pore throats per small pore increases significantly. It is a well-known fact that it is not the average pore throat size that limits permeability, but the smallest pore throat size of an alignment of pores which interconnect the sample from one end to the other.[76] Since the pore size

of the large pores (x_2) for **M4** is smaller than for **M2** and **M3**, there are a larger number of small, interconnected pores typical for conventional polyHIPEs packed into the same volume of material. Therefore, there is a higher likelihood that the limiting pore throat diameter in a series of interconnected pores in **M4** is significantly smaller than the average pore throat size (x_{T1}), which causes the reduction in gas permeability. However it is also possible that there are a larger number of closed pores and therefore fewer interconnected pathways throughout the sample. At a surfactant concentration of 17 w/v% with respect to continuous phase, the surfactant becomes the dominating emulsifier and the hierarchical pore structure is lost in **M5** (Figure 4-1C). Its structure now resembles that of a conventional polyHIPE. [116] A TEM image of M5 (Figure 4-2C) verifies that there were no particle-stabilised interfaces in the emulsion template; instead, the particles were dispersed within the organic phase and, therefore, can now be found within the polymer matrix of the wall.

Small pores of about 13 μm are highly interconnected by about 16.8 pore throats per pore, which have an average diameter of about 3 μm. **M5** also has the lowest gas permeability at 0.13 D, indicating that not only its average pore throat size but more importantly its flow limiting pore throat size is the smallest among **M2** – **M5**.

Macroporous polymers **M3, M6 - M7** (Series 2) were prepared from emulsion templates with increasing particle concentration but a constant surfactant concentration of 4.2 w/v% with respect to the continuous phase. Increasing the particle concentration minimizes limited coalescence of particle-stabilised water droplets,[42, 131] allowing for smaller droplet sizes. This leads to a significant reduction of the poly-Pickering-HIPE-type pore size (x_2, Figure 4-1D). Surprisingly, however, the size of smaller conventional-polyHIPE-type pores (x_1) seems to increase with

increasing particle concentration while their degree of interconnectivity ($\mathbf{N_1}$) decreases. This indicates that it becomes more and more difficult to distinguish between very small poly-Pickering-HIPE-type pore and conventional-polyHIPE-type pores.

The TEM image of M6 (Figure 4-2D) shows an alignment of particle aggregates at the former w/o interface now forming the surface of a large pore. This confirms that the large droplets have been predominantly stabilised by particles. Similar to M3, a small amount of particles is also found dispersed in the polymer matrix, as a result of the changes in the wettability of the particles due to surfactant adsorption.

The gas permeability of **M3** and **M7** is with 1.16 D identical showing that the flow limiting pore throat size is relatively constant, despite an increase in average pore throat size (x_{T1}, x_{T2}) and decrease in number of pore throats per small pore (N_1) with increasing particle concentration. However, the flow limiting pore throat size of **M6** must be significantly smaller since its gas permeability is dramatically reduced compared to **M3** and **M7**.

The mechanical properties of **M1 - M7** are summarised in Table 4-1. In general, it was observed that the hierarchically structured macroporous polymers **M2 - M4**, **M6** and **M7** had higher crush strengths and Young's moduli than both, the closed-cell **M1** and conventional polyHIPE **M5**, despite the constant porosity. This is due to the efficient packing of liquid droplets in the emulsion templates which resulted in a more efficient arrangement of pores in the macroporous polymers after polymerization. **M5** had the lowest crush strength and Young's modulus and was also the most brittle, placing it in the same range as polyHIPEs synthesised from purely surfactant stabilised emulsion templates.[76, 118] The low mechanical strength of

M5 compared to **M1** is due to the high degree of interconnectivity resulting from the large number of pore throats per pore.

Within the set of hierarchically structured macroporous polymers **M2** outperforms **M3**, **M4**, **M6** and **M7**; **M2** has with 3.6 MPa and 27 MPa the highest crush strength and Young's modulus, respectively. However, it also has the lowest gas permeability indicating that it is the least interconnected sample. The increase in surfactant (**M3**, **M4**) as well as particle concentration (**M6**, **M7**) within the emulsion templates induced significant structural changes in the resulting macroporous polymers, which generally improved their interconnectivity and, therefore, their gas permeability but reduced their mechanical performance; the Young's moduli of **M3**, **M4**, **M6** and **M7** decreased by approximately 22% compared to **M2**. Furthermore, a 17% reduction in crush strength can be observed for **M3** and **M4** compared to **M2**. However, the crush strengths of **M6** and **M7** are similar to that of **M2**. This indicates that the increased concentration of particles, which reinforce the polymer matrix, negate some of the loss of mechanical integrity caused by the increasing number and size of pore throats.

4.5 Conclusions

Inspired by hierarchical porous structures in nature such as wood and spongy bone, which have enhanced physical characteristics due to their hierarchical macroporous structure, hierarchical macroporous polymers were synthesised using particles and surfactant as emulsifiers simultaneously. Our macroporous polymers display a hierarchical pore structure as they have characteristics of both, poly-Pickering-HIPEs (predominantly closed pores) and conventional polyHIPEs (interconnected open pores). By studying the location of particles within the macroporous polymer foams using TEM, it can be inferred that the hierarchical pore morphology observed is

indeed a result of predominantly particle-stabilised emulsion droplets and surfactant-stabilised droplets co-existing with one another in the emulsion template.

An improvement in the mechanical properties of our macroporous polymers was observed, due to a more efficient packing of pores in a configuration that improves mechanical strength despite the presence of interconnecting pore throats, making this material attractive for applications where both mechanical strength and interconnectivity are important.

5 Air in Water-in-oil Emulsion Templates: Developing Highly Porous Greener Hierarchical Macroporous Nanocomposite Foams

5.1 Summary

Highly porous, bio-based macroporous polymers were produced using a novel take to the traditional emulsion templating technique. A bio-based monomer, acrylated epoxidised soyabean oil (AESO), was used to prepare water-in-oil (w/o) emulsions with an internal phase volume of 50% stabilised by 3 w/vol.% of a particulate emulsifier. The emulsions were thermally polymerised to produce macroporous polymers with a maximum porosity of 55%. To increase the porosity further, the emulsion templates were mechanically frothed to incorporate air bubbles, producing what are called air in w/o templates. By varying the composition of the continuous phase, the emulsion viscosity was modified, which in turn influenced its ability to incorporate and stabilise air bubbles produced during the frothing process. Both emulsion droplets and air bubbles acted as 'templates' for the final porous structure. This resulted in highly porous bio-based macroporous polymers with a hierarchical pore arrangement after polymerisation. It was found that mechanically frothing w/o emulsions containing an internal phase volume ratio of 50% using a 1:1 ratio of AESO and trimethylbenzene (TMB) as a diluent in the continuous phase resulted in a final porosity of 81%. Scanning electron micrographs, viscoelastic properties as well as thermal degradation temperatures of these hierarchical porous structures were analysed and discussed.

5.2 Introduction

Highly porous macroporous polymers are sought after for their distinctive properties, including low densities and lightweight. They are often identified by unique internal architectures of pores packed into a solid polymer matrix, bestowing properties that make them an important class of materials for many consumer goods and engineering applications. Currently, macroporous polymers are produced using physical or chemical blowing agents,[6, 132] solvent casting and particle leaching,[98] thermally induced phase separation (TIPS)[6, 133-136] and using supercritical carbon dioxide foaming.[100, 137, 138] Depending on the number, size and interconnectivity of the pores, porous polymers can be used as absorbents,[139] catalyst supports,[3] scaffolds for tissue engineering[108] and as sandwich core for building and construction materials.[140] In recent years, the need for sustainable development has motivated a transition to 'greener' polymers produced using renewable monomers and/or processing techniques that are environmentally friendlier.[141-143] Non-biodegradable polymer foams, traditionally associated with numerous recycling issues, have created a negative environmental backlash.[144] This is the driving force for the choice of a bio-based monomer and processing methods used in this study.

The bio-based monomer chosen for this study was acrylated, epoxidised soyabean oil (AESO), synthesised by an epoxidation reaction between acrylic acid and the naturally occurring triglycerides found in soyabean oil.[145, 146] The acrylated, epoxidised triglycerides in AESO provided sites for crosslinking during polymerisation, resulting in highly-crosslinked polymers that have and tensile modulus of 0.4 GPa and tensile strength of 4.1 MPa as previously reported.[147] Some researchers have explored the potential of AESO to produce polymer foams. Guo et al.[19, 20] first reported on the formation of rigid soyabean oil based polyurethane

foams synthesised using polyolys derived from soyabean oils, which became a popular route for the production of polymer foams using other vegetable oils. [148, 149] [148, 149] [146, 14722, 23,145, 146] Bonnaillie et al.[150] reported on the use of a carbon dioxide pressurising foaming process using AESO as a component as another route to synthesise bio-based polymer foams.

Alternatives methods used to produce bio-based foams using emulsion and 'air' templating techniques were introduced by our group recently. The first was described by Blaker et al.[111] where water-in-oil (w/o) emulsions were prepared by dispersing varying amounts of aqueous phase in AESO, stabilised by hydrophobised bacterial cellulose fibrils. The bacterial cellulose acted as a 'green' Pickering emulsifier for the w/o emulsion template. Using a free radical initiator and UV stimulus, the emulsions were UV polymerised, retaining the droplet structure at the gel point of polymerisation, hence the process was termed 'emulsion templating'. 50 vol.% (internal phase) w/o emulsions were polymerised and vacuum dried to yield macroporous polymers with up to 76% porosity. Since the internal phase volume dictated the final porosity of the porous material, the authors attributed this unexpected increase in porosity to the trapping of air in the emulsion during the high energy, homogenisation process.[111] Another study by Lee et al.[151] described a solvent and surfactant free 'air templating' process. This involved mechanically frothing AESO with dissolved lauryl peroxide as a radical initiator followed by microwave curing to produce three-dimensional (3D) bio-based porous materials with a maximum porosity of 59%. It was found that adding bacterial cellulose to the air-AESO templates not only increased the stability index of the foams, it further improved the compressive properties of the final 'green' polymer nanocomposites formed by acting as nanoreinforcement.[151]

These two studies showed promising results for the production of bio-based porous materials using templating methods. However, the practical difficulty of producing air-in-AESO templates with internal phase volumes greater than 50 vol.% limited the production of highly porous polymer foams with clearly defined pore morphologies and high (>50%) porosities. In the case of water-in-AESO emulsion templates, increasing the internal phase volume to 70 vol.% resulted in phase inversion from water-in-AESO to AESO-in-water emulsions, which polymerised to porous structures consisting of fused polymer beads.[111] Increasing the concentration of hydrophobised bacterial cellulose (Pickering stabiliser) past 4 wt.% drastically increased the viscosity of the continuous phase. This high viscosity made it practically impossible to prepare emulsions with internal phase volumes higher than 50%.[111]

The synergy between the emulsion and air templating techniques was recognised and ued a combination of the two was used to synthesise highly porous foams in this study. More specifically, thick and viscous particle-stabilised water-in-AESO emulsions can be mechanically frothed to incorporate air bubbles. The use of a second phase such as water and/or air would increase the overall ‘internal’ phase volume of the template and thus the final porosity. Resulting macroporous polymers would be closed cell and hence expected to possess better dimensional stability, lower moisture absorption and better compressive strength compared to open celled materials. These are desirable properties for a variety of applications such as thermal and sound insulation, flotation devices and coatings as well as specialty materials for sandwich cores etc.[152]

5.3 Experimental

5.3.1 Materials

Acrylated epoxidised soyabean oil, AESO (8500 ppm monomethyl ether hydroquinone as an inhibitor), oleic acid (OA, ≥99%), trimethylbenzene (TMB, 98%), styrene, calcium chloride dehydrate and methanol were purchased from Sigma Aldrich (Kent, UK). Polyethylene glycol dimethylacrylate (PEGDMA, 330 $gmol^{-1}$) was kindly supplied by Cognis (Hampshire, UK). The free radical initiator α, α'-azobisisobutyronitrile (AIBN) was purchased from Camida (Tipperary, UK). Hydrophilic silica particles (Technical data sheet: 20 nm) were kindly supplied by Ortiwin-Rave Produkte + Dienstleistungen (Rhineland-Palatinate, Germany). Deionised water was used in all the experiments. All chemicals were used as received, without purification unless stated otherwise.

5.3.2 Preparation of Polymer Foams Using Emulsion Templates

In order to encourage the silica to adsorb at the oil-water interface during emulsification, the particles were modified with OA, using a method previously reported.[45] The OA-functionalised silica (3 wt.% with respect to continuous phase volume, OA content of 2.5±1.0 wt.% by TGA) was homogenised with the continuous phase consisting of varying amounts of AESO, TMB, Styrene and PEGDMA (composition summarised in Table 5-1) using a homogeniser (Kinematica, Luzern, CH) at 10,000 rpm in an ice bath for 10 min. The continuous phase mixture was then transferred to a glass reaction vessel and stirred continuously using a glass paddle rod connected to an overhead stirrer controlling the speed of emulsification. 1 mol-% AIBN (with respect to the monomers) was added to the vessel, followed by the drop-wise addition of 50% (with respect to total emulsion volume) 2.5 M

aqueous calcium chloride dihydrate solution (dispersed phase), continuously stirring at a constant rate of 500 rpm. After all the dispersed phase was added, the rate of stirring was increased to 2,000 rpm for 30 s. The resulting emulsions were transferred to individual Falcon™ tubes for polymerisation in a convection oven at 70°C for 24 h. After polymerisation, the solid samples were removed from the Falcon™ tubes and washed in DI water followed by methanol to remove, as much as possible, any residual monomers and TMB since the materials are closed cell. TMB appeared to have a plasticising effect on the porous materials, causing shrinkage if dried in vacuum at 70°C for 24 h, which is the typical drying procedure reported for macroporous polymers by our group[52, 111, 112]. In order to minimise shrinkage, freeze drying was carried out at a constant temperature of -196°C to remove water, methanol, TMB and unreacted co-monomers until a constant weight was achieved, or what is termed the modified freeze drying process.

5.3.3 Preparation of Polymer Foams by Mechanically Frothing Emulsion Templates from 5.3.2

Mechanical frothing of w/o MIPEs prepared was carried out using a hand mixer operating at maximum power output (100 W) for 5 min. Air was incorporated into the emulsions until they approximately doubled in volume using a technique previously described elsewhere.[151] The aerated emulsions were then transferred gently, so as not to lose any trapped air, into freestanding polypropylene centrifuge (Falcon®) tubes for polymerisation in a convection oven at 70°C for 24 h. After polymerisation, the solid samples were removed from the Falcon tubes and washed as previously described. To reduce shrinkage, the modified freeze drying method mentioned earlier was used as the final drying step.

5.3.4 Characterisation of Polymer Foams

5.3.4.1 Density and Porosity of Polymer Foams

Helium displacement pycnometry (Accupyc 1330, Micrometrics Ltd, Dunstable UK) was used to measure the skeletal density (ρ_s) of the polymer foams. Prior to the measurement, approximately 20 mg of polymer foam was crushed into a powder and dried in a vacuum oven at 120°C until weight constancy. Envelope densities (ρ_e) were determined by taking the ratio between the mass (m) and the volume (V) of cubical samples with known dimensions ($\rho_e = m/V$). The percentage porosities (P) were calculated using the following equation:

$$\boldsymbol{P = \left(1 - \frac{\rho_e}{\rho_s}\right) \times 100\%}$$

Equation 4

5.3.4.2 Structure and Morphology of Polymer Foams

The morphology of the macroporous polymers was characterised using variable pressure scanning electron microscopy (SEM, Hitachi High Technologies, S3400N VP SEM) using an accelerating voltage of 5 kV. Dried macroporous polymers were fractured to reveal the internal structures using a surgical blade. Each sample was mounted on individual aluminium stubs fixed with carbon adhesive stickers. The samples were then gold coated at 20 mA for 60s (Scan Coat Six SEM Sputter Coater, Edwards Ltd., Crawley, UK) to ensure electrical conductivity during imaging. Pore dimensions (at least 200 for each sample formulation) were analysed using the imaging software ImageJ (Version 1.46).

5.3.4.3 Thermogravimetric Analysis (TGA) of Polymer Foams

Thermal degradation of the polymer foams were characterised using TGA (TGA Q500, TA Instruments, UK). Approximately 20 mg of sample was heated from 25°C to 800°C under a flow of 40 mL/min nitrogen atmosphere at a heating rate of 10°C/min. the degradation temperature was defined as the temperature whereby the weight decreased by 50%.

5.3.4.4 Dynamic Mechanical Thermal Analysis (DMTA) of Polymer Foams

DMTA was used to determine the viscoelastic properties of the polymer foams in compression mode. Five specimens of each polymer foam formulation were cut to $5 \times 5 \times 5$ mm^3 pieces and subjected to small cyclical deformations at a frequency of 1 Hz. The temperature was increased at a rate of 4°C/min from -90°C to 200°C. The storage (E') and loss moduli (E'') were computed from the viscoelastic response measured from each polymer sample. The loss factor tan δ was calculated from the ratio between the two ($\tan\delta = E'/E''$).

5.4 Results and Discussion

To prepare the emulsions, 3 wt.% of a particulate emulsifier, functionalised silica prepared using a previously reported method[112] (with respect to the continuous phase volume) and 1 mol.% free-radical initiator (with respect to monomers) were dispersed in the monomer solution, forming the continuous phase. To this, a maximum internal phase volume of 50% with respect to total emulsion volume was added drop wise under stirring to produce homogenous medium internal phase emulsion (MIPE) templates, which were thermally polymerised in a convection oven at 70°C. A MIPE with 100% (by volume) of AESO as the continuous phase was first prepared as a control sample (sample number 0). The high viscosity of pure AESO

increased the rate of emulsion destabilisation during polymerisation. This resulted in phase separation and the formation of a thin, sticky polyAESO coating around the porous polymer after polymerisation. After drying at 120 °C in a convection oven, the sample shrank severely and developed large cracks (Figure A0-3), making it unsuitable for characterisation. To synthesise stable emulsion templates, trimethylbenzene (TMB) was chosen as a diluent to decrease the viscosity of the continuous phase for emulsification (Sample **A1**). To promote cross-linking and avoid the large cracks observed in pure polyAESO foams (seen in control Sample 0), styrene and polyethylene glycol dimethylacrylate (PEGDMA) were chosen for copolymerisation with AESO. The concentration of AESO, TMB, styrene and PEGDMA were then varied (Sample **A2** and Sample **A3**) to determine the effect of varying the composition and hence the viscosity of the continuous phase on the pore morphology of the final porous product. The composition of the emulsion templates prepared are summarised in Table 5-1. These AESO-based emulsion templated foams were observed to shrink when dried in a convection oven at 120°C (Figure A0-5), which is the drying protocol typically used and reported previously.[52, 111, 112] Therefore, a modified freeze-drying method was developed to dry the samples with minimal shrinkage. This involved freeze-drying the sample under vacuum, maintained at a low temperature of -196°C using liquid nitrogen.

A maximum of 50% internal phase emulsions were used as phase separation was observed when the internal phase volume was increased beyond 50% for emulsions having the same particulate emulsifier concentration (in the continuous phase volume). Phase separation or inversion is quite typically observed for Pickering emulsions stabilised by dilute particulate emulsifier concentrations at or near these concentrations.[40]

To formulate air in water-in-oil emulsion templates, emulsions used to produce samples **A1** to **A3** were mechanically frothed using an electrical hand-held mixer, incorporating air until the total volume was approximately doubled (visually). The resulting air in water-in-oil templates were then polymerised to produce the samples **A1*** to **A3***, respectively, in Series II. Macroporous polymers were then dried under vacuum via the modified freeze drying process.

Table 5-1: Summary of composition of emulsion templates used, including the concentration of emulsifying particles (C_p) before (Series I) and after (Series II) mechanical frothing

Series	Sample	Aqueous Internal phase (vol.%^)	Continuous phase (50 vol.%^)				C_p (w/vol.%)
			AESO (vol.%@)	TMB (vol.%@)	ST (vol.%@)	PEGDMA (vol.%@)	
N/A	**0**	50	100	0	0	0	3
I	**A1**	50	50	50	0	0	3
	A2	50	40	40	10	10	3
	A3	50	30	30	20	20	3
II	**A1***	50	50	50	0	0	3
	A2*	50	40	40	10	10	3
	A3*	50	30	30	20	20	3

^ with respect to total emulsion volume, @ with respect to volume of continuous phase

5.4.1.1 Skeletal Densities and Porosities of Macroporous Polymer Foams

Skeletal densities, summarised in Table 5-2, were constant within and also between Series I and II (e.g. **A1** with **A1***, **A2** with **A2*** etc.). Envelope densities appeared constant when comparing samples **A3** with **A3***, but a noticeable reduction in envelope density was seen in **A2*** (reduced by 22% from **A2**) and **A1*** (reduced by 60% from **A1**). As skeletal and envelope densities are related to porosity using Equation 4, this decrease in envelope density in turn resulted in the increase in porosity for **A2*** and **A1*** compared to **A2** and **A1**, respectively (Table 5-2).

Table 5-2: Summary of porosity (P), skeletal density (ρ_S) and envelope density (ρ_E) measured before (Series I) and after (Series II) mechanical frothing.

Series	Sample	$P^{\&}$ (%)	$\rho_S{}^{\#}$ (g/cm^3)	$\rho_E{}^{\&}$ (g/cm^3)
N/A	**0**	-	-	-
I	**A1**	54±1	1.14±0.01	0.53±0.01
	A2	52±2	1.14±0.01	0.54±0.02
	A3	55±1	1.13±0.01	0.51±0.01
II	**A1***	81±1	1.14±0.01	0.21±0.01
	A2*	63±1	1.13±0.01	0.42±0.01
	A3*	57±1	1.13±0.01	0.48±0.02

[&]standard deviation for 5 measurements, [#]standard deviation for 10 measurements

Generally, it was observed that the porosity of the mechanically frothed emulsions increased with increasing AESO concentration (**A1***>**A2***>**A3***). It was hypothesised that this upward trend in porosity was related to the viscosity of the emulsions before mechanical frothing. This hypothesis holds, assuming that the rate of emulsion destabilisation is much slower than the rate of destabilisation of air bubbles trapped during the frothing process. The viscosity of the continuous phase affected the emulsion's ability to stabilise air bubbles. When more air bubbles are formed and stabilised by the viscous surrounding emulsion phase, it increased the

ultimate internal phase volume consisting of both emulsion droplets and air bubbles. A higher emulsion viscosity reduces the rate at which air bubbles rise through the emulsion by decreasing the rate of drainage from the liquid film between bubbles due to gravity and capillary forces.[153] Therefore, the rate of smaller bubbles coalescing into larger bubbles over the course of polymerisation is lowered. Since the emulsion template for **A1** was observed to be the most viscous, it had the slowest rate of bubble coalescence compared to the other emulsion templates when mechanically frothed. This resulted in the greatest reduction in envelope density and consequently highest porosity of 81% observed for **A1***.

Another stabilisation mechanism of bubbles in dispersions is the reduction of interfacial tension due to the adsorption of particulate stabilisers at the air/oil and air/water interfaces.[154] However, since all the emulsions were prepared with 3 w/vol.% of particles, any reduction in interfacial forces due to particle adsorption at the oil-air interface was considered to be the same across all the emulsions in the series. Furthermore, the stabilisation of oil-air interfaces requires extremely hydrophobic particles,[141] which is not a characteristic of the oleic-acid functionalised silica used in this study. Therefore, it is unlikely that the particulate emulsifiers contribute significantly to the stability of the foam.

5.4.1.2 Pore Morphology of Polymer Foams

The SEM images of macroporous polymers prepared from emulsion templates before and after mechanical frothing are displayed in Figure 5-1. By comparing Series I (**A1** to **A3**), there is a clear influence of the continuous phase composition on the final morphology of the macroporous polymers, keeping the internal phase volume, emulsifier concentration and emulsification parameters, such as the stirring

time and rate constant. Comparing between Series I and II (Samples **A1** with **A1***, **A2** with **A2*** etc.), it is apparent that the action of mechanical frothing changed the pore size distribution and pore arrangement of the resulting macroporous polymers (Figure 5-1). In **A1**, a multi-modal pore size distribution was observed as smaller pores in the range of 5 – 20 μm were packed between larger pores having diameters in the range of 100 – 200 μm. After mechanical frothing (**A1***), the range of large pores decreased to 50 – 100 μm and a significant increase in the number of smaller pores in the range of 2 – 20 μm packed between the larger pores was seen, which is what is termed a hierarchical pore structure (defined as a multimodal pore size distribution packed in an efficient arrangement as described in a previous study by our group[113]). **A2** had almost no pores in the range of 5 – 20 μm in the polymer walls separating the large pores, which were as large as 500 μm. Comparing **A2** with **A2***, a much greater number of smaller pores in the range of 5 – 20 μm were found in the polymer walls separating larger pores in the range of 300 – 500 μm after mechanical frothing. In **A3,** pores in the range of 5 – 20 μm were packed in between larger pores in the range of 200 – 300 μm. After mechanical frothing, the pore size distribution shifts downwards as the range of the larger pores decreased to 100 – 300 μm for **A3*** and the number of small pores in the range of 5 – 20 μm packed in between the large pores increased.

When emulsions are mechanically frothed, the system becomes complex as foams and emulsions coexist in the same formulation. The pore arrangement after mechanical frothing could, therefore, be a result of a combination of (i) the inevitable breakup of emulsion droplets due to the energy input during frothing or (ii) coalescence and/or sedimentation of emulsion droplets and air bubbles concurrently.

Evidence also exists for the stabilising effects from the accumulation or adsorption of emulsion droplets at the surface of air bubbles trapped in viscous emulsions.[155] Although the exact mechanism describing how this works is not clear yet,[156] this could mean the smaller pores (2 – 20 μm) found accumulated near the larger pores (between 100 and 500 μm) seen in all the mechanically frothed samples could be a result of trapped air bubbles stabilised by smaller emulsion droplets.

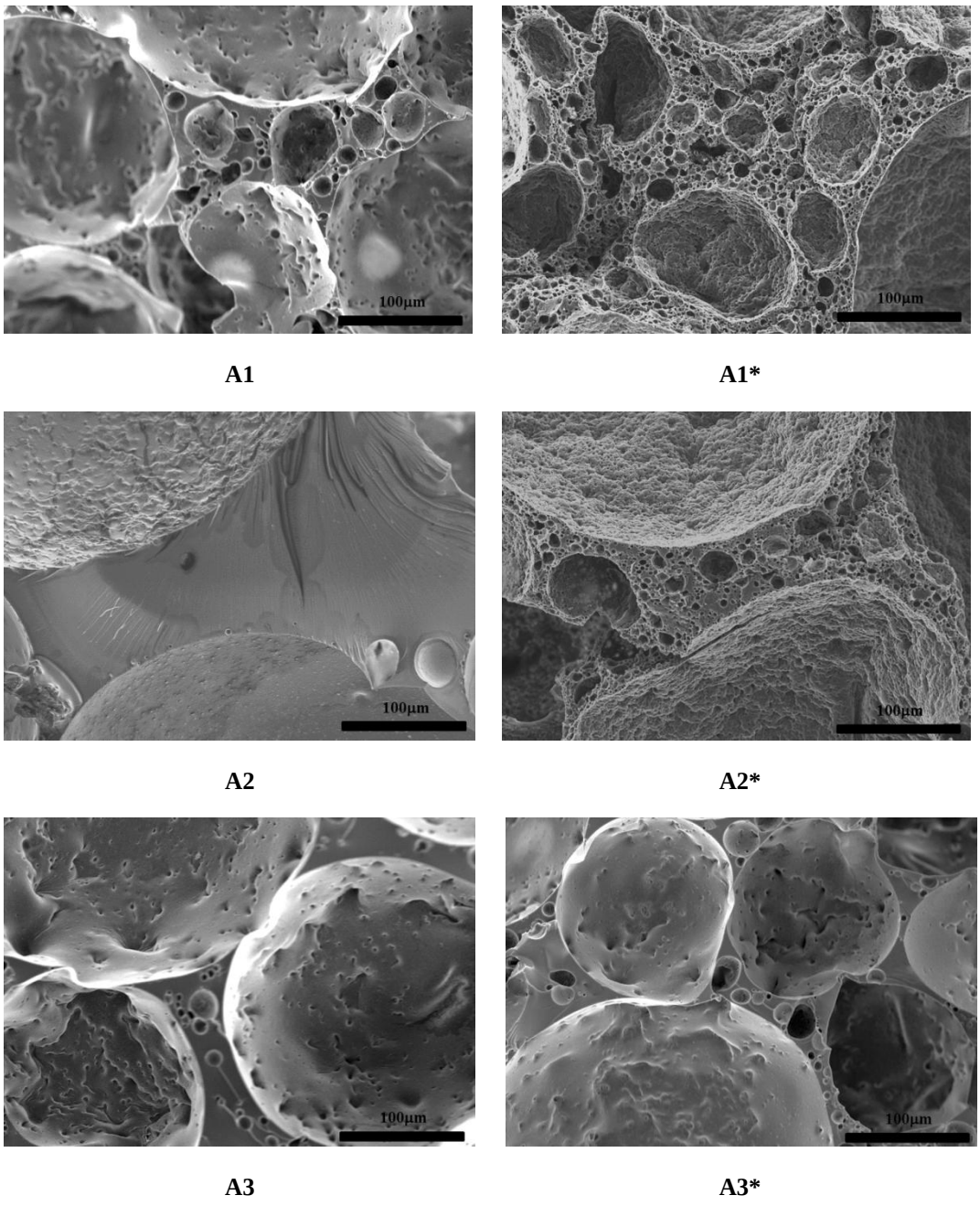

Figure 5-1: Representative SEMs of Series I and II from emulsion templated porous materials before (left) and after (right) mechanical frothing.

5.4.1.3 Viscoelastic Properties of Polymer Foams

DMTA was used to investigate the viscoelastic behaviour of the polymer foams. Uniformly cut and dried samples were heated from -90°C to 200°C, keeping the heating rate and frequency of vibration in compression mode constant at 4°C/min and 1 Hz, respectively. Representative curves showing the temperature dependence of the storage moduli and damping behaviour (tanδ) of samples **A1** to **A3** are displayed in Figure 5-2.

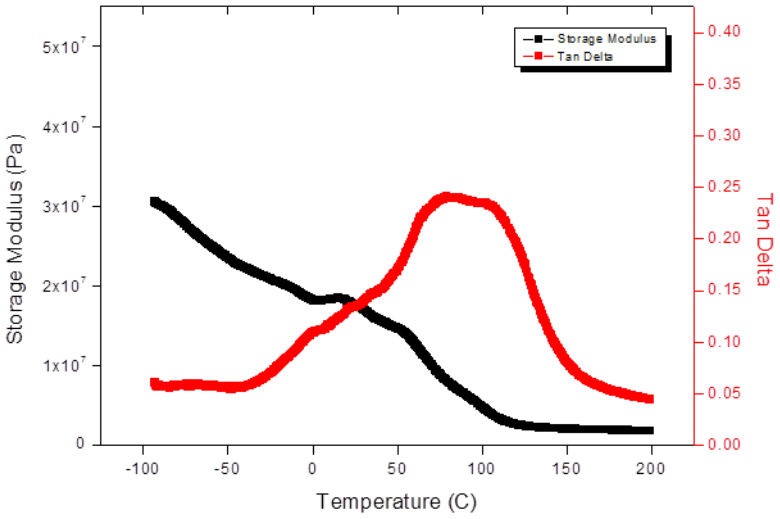

A1

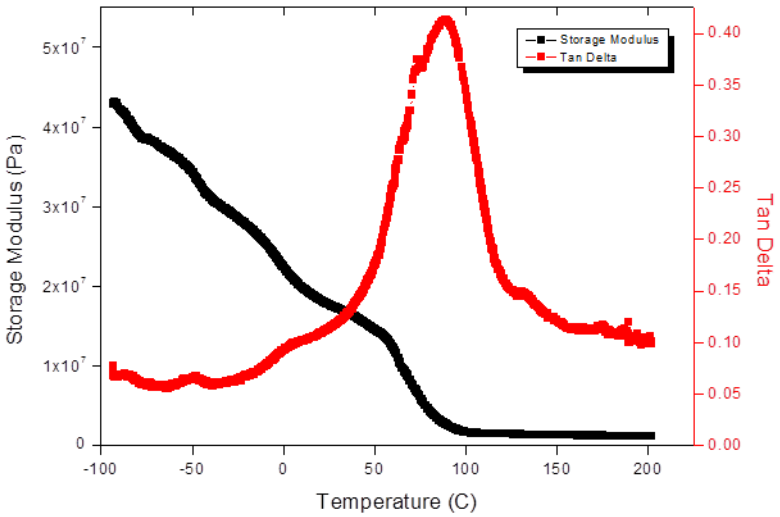

A2

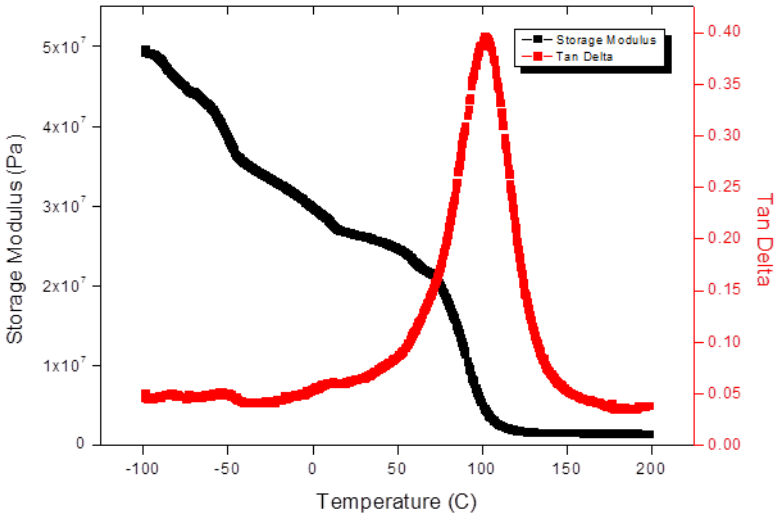

A3

Figure 5-2: Representative curves of the storage modulus (black) and tanδ (red) with respect to temperature of A1 (top) to A3 (bottom) subjected to oscillations at a constant frequency of 1 Hz.

The polymers appears to weaken with increasing temperature for all three samples, seen from the gradual decrease in storage moduli. This is possibly due to the relaxing of thermal stresses in the polymer samples as temperature increases. Differences in the temperature at which a peak in the tanδ curve was observed for the three samples

show the effects of varying the formulation composition and the amount of plasticiser on the damping behaviour of the polymer foams. **A3** had the highest tanδ peak in the series, at 105°C, suggesting the lowest amount of plasticiser present in the polymer foams. From **A2** to **A1**, the tanδ peak decreased to 92°C and 89°C, respectively, which suggests an increasing amount of plasticiser trapped in the polymer foam which consequently lowered the transition temperature. The range of transition temperatures recorded for **A1** to **A3** are generally higher than the glass transition temperature of pure polyAESO previously reported[95] (Figure A0-4) due to the differences in polymer composition.

This explained the noticeable shrinkage when the polymerised samples were subjected to the typical drying protocol using a convection oven (Figure A0-5).[52, 111, 112] While being heated to a high temperature of 120°C, the polymer foams softened and started relaxing in response to thermal stresses, which resulted in shrinkage. Therefore, it was necessary to keep drying temperatures below the temperature at which a peak in the tanδ was observe, which was achieved by using the modified freeze drying process, minimising shrinkage during the course of drying.

5.4.1.4 Thermal Degradation Behaviour of Polymer Foams

The thermal degradation behaviour was determined by using Thermogravimetric Analysis (TGA). Representative curves of weight loss as function of temperature for **A1** to **A3** are shown in Figure 5-3.

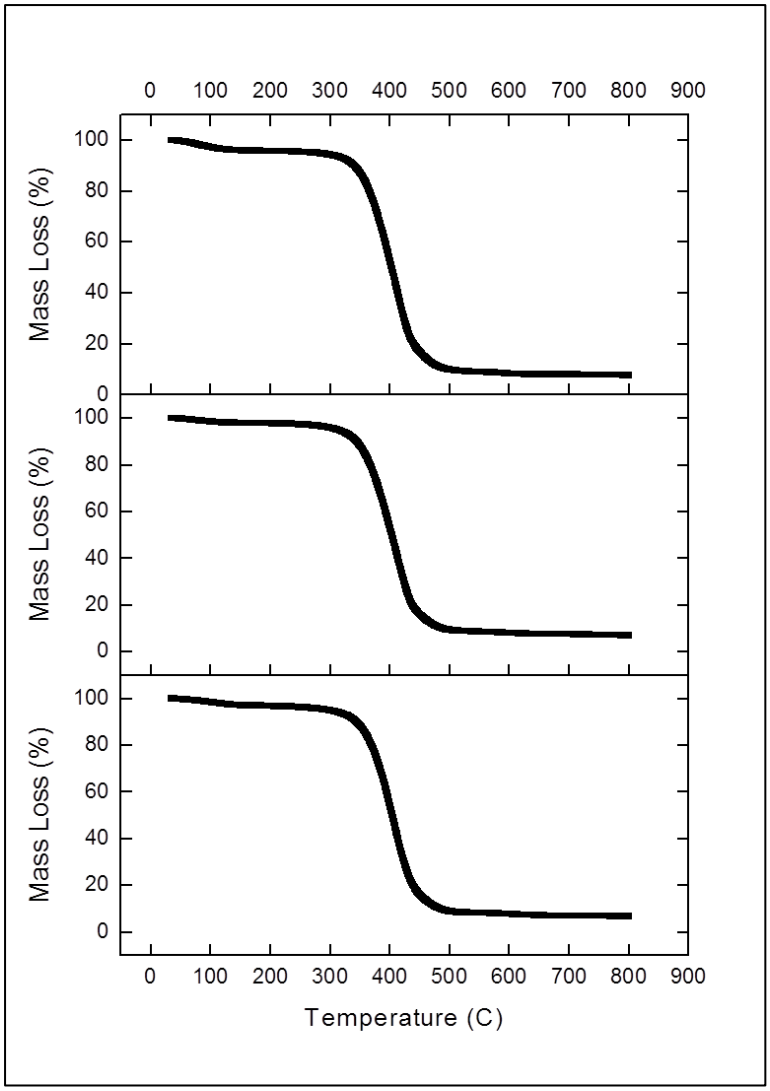

Figure 5-3: Representative graphs for the mass loss (%) with increasing temperature for A1 (top) to A3 (bottom) in nitrogen.

All polymer foams underwent single step degradation in nitrogen. Between 0°C and 300°C, residual water and TMB still trapped in the closed cell materials were removed. As the temperatures increased further past 330°C, a drastic decrease in mass was observed, which is indicative of polymer degradation via random chain scission.[157] Volatilisation and removal of the degraded by-products resulted in the decrease in sample mass between 330°C and 500°C. Since the same degradation temperature of approximately 405°C was observed for all three samples, it can be said that varying the composition of AESO did not have a significant effect on the

overall thermal degradation behaviour. The residual mass content were 6.5 wt.%, 7 wt.% and 7.5 wt.%, respectively, possibly due to the increasing carbon content remaining in the nanocomposite foams after pyrolysis.

5.5 Conclusions

A unique templating process was used to synthesise highly porous macroporous polymer foams using a bio-based monomer (AESO) blended with a diluent (TMB) and co-monomers (styrene and PEGDMA). AESO-based emulsion templates were then mechanically frothed, introducing air bubbles into w/o medium internal phase (ratio) emulsions (MIPEs). Increasing the concentration of AESO in the continuous phase increased the viscosity of the continuous emulsion phase. This in turn influenced the ability of the emulsion to entrap and stabilise air bubbles, increasing the overall internal phase volume, in this case, an aqueous phase and air. Thus, resulting in an increase in the final porosity of the polymer foam obtained after polymerisation. A modified freeze-drying process was used to dry the porous materials after polymerisation to minimise foam shrinkage. A comparison of SEM images of the macroporous polymers before and after mechanical frothing showed noticeable changes in the porous morphology. After mechanical frothing of the emulsion templates, a greater frequency of small pores in the range of 2 – 20 μm and much higher porosities for template systems of up to 81% by frothing 50% internal phase w/o MIPEs were observed. The temperature at which a peak in the tanδ was observed decreased with increasing AESO and TMB content of the organic phase of the template.

6 Nanocomposite Macroporous Polymers and Beads Synthesised from Emulsion Templates Stabilised by Chemically Modified Graphene

6.1 Summary

Chemically Modified Graphene (CMG) has been studied extensively as a nanoreinforcement for nanocomposites, a conductive nanofiller and more recently as an emulsion stabiliser. This work links these multiple functionalities to develop 3D nanocomposite structures (in the form of macroporous polymers and beads) via emulsion templating. High internal phase emulsions with an internal phase volume fractions exceeding 74 vol.% were prepared using CMG in the form of reduced Graphene Oxide (rGO). rGO proved to be an efficient emulsion stabiliser, since very low concentrations of 0.2 mg/ml (with respect to oil phase) were required to stabilise water-in-oil High Internal Phase Emulsions. After polymerisation of the monomer (oil) phase, highly porous macroporous polymers with tunable microstructures were obtained. Stiffness increased by an order of magnitude by increasing the rGO concentration in the emulsion templates from 0.4 mg/ml to 0.8 mg/ml. Moreover, the macroporous polymers exhibited an extremely low rGO percolation threshold, showing electrical conductivity at 0.006 vol.% (related to the total volume of nanocomposites) compared to 0.1 vol.% for dense nanocomposites previously reported. This provided evidence for the efficient arrangement of the rGO creating a conducting network within the macroporous polymer nanocomposite. Resulting CMG based nanocomposites retained the useful properties of two-dimensional CMG, yet displayed unique structure-property relationships in the three-dimensional form.

This is a potentially viable method to manufacture conductive macroporous polymer nanocomposites by incorporating two-dimensional materials.

6.2 Introduction

Graphene, a two-dimensional (2D) flake formed by a monolayer of sp^2 carbon atoms packed into a honeycomb lattice, has attracted much scientific attention during the last years due to its exciting properties including high elasticity and stiffness and extremely high electron mobility and thermal conductivity.[158-163] However, the usual synthesis methods for pure graphene, such as chemical vapor deposition, are impractical for the synthesis of the large quantities required to produce three-dimensional (3D) materials such as macroporous materials or composites. In contrast, chemically modified graphene (CMG) namely graphene oxide (GO) and reduced graphene oxide (rGO) can be fabricated in bulk quantities through the chemical exfoliation of graphite.[164, 165] GO, the direct product of the exfoliation process, is an insulator due to the sp^3 C-O bonds but many of the C-C sp^2 bonds are restored by chemical or thermal reduction of the functional groups leading to a semiconductor state.[163, 166, 167] The resulting rGO offers similar electrical, thermal and mechanical properties to pristine graphene.[166]

The processing of CMG allows the controlled formation of covalently bonded oxygen functionalities on its surface, such as hydroxyls and epoxides on the basal plane and carboxyl groups at flake edges. These functionalities enable the surface chemistry of CMG to be widely tuneable, enabling its decoration with metal-oxide/sulphides nano-particles,[168, 169] facilitating its incorporation into different polymeric matrices and improving the adhesion to polymers in nanocomposites.[161, 170, 171]

Due to the hydrophilic ionisable groups on the basal plane edges and the hydrophobic unoxidised graphitic nano-islands within the basal plane, CMG exhibits hydrophilic and hydrophobic regions in an edge to centre configuration, making it surface active.[62, 172, 173] It has been shown that CMG adsorbs at the air/water and oil/water interface leading to the formation of large-scale 2D assemblies and stabilising o/w emulsions respectively.[62, 173, 174,175]

Initial attempts have been made to incorporate 2D CMG into 3D structures for application as advanced materials.[161, 176-179] However, since CMG is also surface active, it can multi-task as a particulate emulsifier and a nanoreinforcement to fabricate 3D, functional macroporous polymers via an up-and-coming technique called emulsion templating. This is an exciting concept that has not yet been explored until now.

Emulsion templating is a versatile method to synthesise macroporous composite materials with tuneable pore structures.[38, 44, 52, 180-190] Macroporous polymers have unique properties that cannot be achieved by a dense material with the same composition. These include increased surface area and low foam density. The addition of CMG into macroporous polymers is expected to enhance its mechanical, thermal and electrical properties.[191-194] In conventional emulsion templating to produce polymer foams, a dispersed aqueous phase, often containing an electrolyte, is emulsified within an oil phase consisting of monomers and crosslinkers, such as styrene and divinylbenzene (DVB), a suitable initiator and emulsifier(s). This forms a water-in-oil (w/o) emulsion. Since the continuous oil phase polymerises around each dispersed water droplet, the individually dispersed water droplets act at the gel point of the polymerisation as a template for the final macroporous structure – hence the name emulsion templating.[19]

W/o emulsions with a internal phase volume greater than 74 vol.% are termed High Internal Phase (ratio) Emulsions (HIPEs). After HIPEs are polymerised and dried to remove the water phase, very porous polymers known as poly(merised)HIPEs, are produced.[36] PolyHIPEs are lightweight, have a low foam density and low thermal conductivity. Since the emulsion templates are liquid, they can be injected or molded into any desired shape or cast into thin membranes, facilitating the applicability of the materials after polymerisation.

Depending on the emulsifier used, the morphology of the synthesised macroporous polymers differs. Macroporous polymers synthesised from surfactant stabilised HIPEs are recognizable by their high degree of pore interconnectivity. Pores have diameters ranging from 5 – 100 μm with interconnecting pore throats that have diameters ranging from 20-50% of the pore size, connecting each individual pore. The high surfactant concentration used to produce HIPEs is a major cost factor and if not removed properly from resultant polyHIPEs, has been shown to reduce the mechanical properties.[195]

Particles can also stabilise emulsions by adsorption at liquid-liquid interfaces.[196, 197] They tend to adsorb almost irreversibly (with very high associated energy) at oil-water interfaces resulting in very stable emulsions. Emulsions stabilised by particles are termed Pickering HIPEs and after polymerisation, poly-Pickering-HIPEs. A range of different modified inorganic and organic particles including silica, titania, carbon nanotubes (CNT) and nanocellulose have been used as particulate stabilisers in emulsions.[185, 198, 199] In contrast to polyHIPEs, poly-Pickering-HIPEs are close-celled (not interconnected by pore throats). This unique property makes these moldable macroporous polymers interesting for many applications, ranging from thermal or acoustic insulation, packaging to specialty applications in composites, in

which currently high performance closed cell polymer foams, such as Rohacell® and Divinycell, are being used in sandwich composite structures. Moreover, the particles dispersed within the polymer matrix also act as reinforcement, improving the mechanical properties of poly-Pickering-HIPEs when compared to conventional polyHIPEs.[190]

In this work the surface activity of CMG made it possible to stabilise emulsions to produce beads and macroporous polymers via the emulsion templating technique. Our approach is to adjust the hydrophobicity/hydrophilicity of CMG through controlled thermal reduction in order to decrease its basal plane wettability by water, making the preparation of w/o emulsions possible. The structure of the resulting polyHIPEs and its influence on the mechanical and electrical properties were also analysed.

6.3 Experimental

6.3.1 Processing of Chemically Modified Graphene (CMG) Flakes

CMG suspensions were obtained by the exfoliation of graphite using the modified Hummers method.[200] The resulting liquid was transferred into 85 ml PC centrifuge tubes (Nalgene) and purified by centrifugation at 9000-10000 rpm, removal of the supernatant and addition of deionized water. This process was repeated at least 15 times. Non-exfoliated particles were then removed by centrifugation at lower speeds (1000-3000 rpm). The efficiency of the process was monitored via optical microscopy.

GO flakes were obtained by freeze-drying GO suspensions (Freezone 4.5, Labconco Corporation) for 48 h below 0.1 mbar. rGO flakes were produced by thermally reducing GO at 800ºC in a 10%H_2/90%Ar atmosphere in a tubular oven (Carbolite

Furnances). For this purpose 60-90 mg GO flakes were placed in an alumina boat forming a compact layer of material. The crucible was inserted in the middle of a quartz tube, which was then placed into the tubular oven. This thermal reduction procedure was used to obtain more hydrophobic and electrically conductive flakes.

6.3.2 Preparation of Nanocomposites Beads and Macroporous Polymers

The general methodology developed for the fabrication of GO-polystyrene-divinylbenzene (GO-P(S-co-DVB)) beads and rGO-P(S-co-DVB) macroporous polymers is illustrated in Figure 6-1.

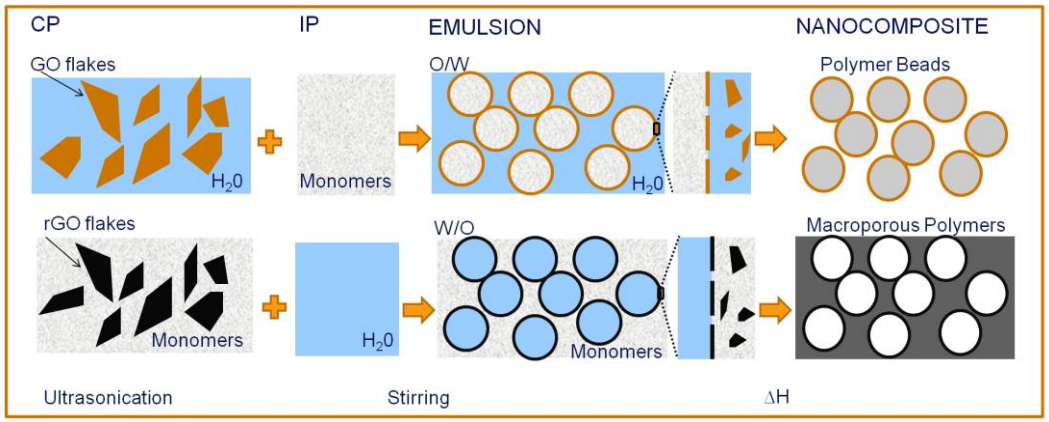

Figure 6-1: Schematic summarizing the fabrication procedure for nanocomposite beads and macroporous polymers.

To prepare beads, o/w emulsions stabilised with 0.4 mg/ml GO with respect to the water phase were prepared by first homogenising GO in deionized water (Kinematica Luzern, CH) in an ice bath. A 1:1 by volume mixture of styrene and divinylbenzene (St:DVB) (40 vol.% with respect to total emulsion volume) was then slowly added to the aqueous phase and emulsified using a vortex mixer (Genie 2 ™, Scientific Industries, USA) until an emulsion was obtained. The free-radical initiator α,α'-azoisobutyronitrile (AIBN, Camida, Tipperary, Ireland) (1 mol-%) was added to the freshly prepared emulsions. The emulsions were then transferred into 15 ml polypropylene SuperClear™ centrifuge tubes (VWR UK), which were sealed and

placed into a convection oven at 70°C for 24 h for polymerisation. After polymerisation, the beads were separated by filtration and washed with deionized water before drying in a vacuum oven at 110°C in between two pieces of filter paper until constant weight.

To fabricate macroporous polymers, rGO-stabilised w/o emulsions were prepared by homogenising rGO at concentrations ranging from 0.1 to 5 mg/ml with respect to organic phase in a 1:1 (by volume) mixture of St:DVB in an ice bath using an ultrasonic tip for 30 min to an hour until aggregates were no longer visible with the naked eye. As controls, 25 mg/ml of oleic acid modified titania prepared using a method previously reported,[62] was dispersed in the same 1:1 (by volume) mixture of St:DVB using a homogeniser (Kinematica Luzern, CH) at 15000 rpm for 10 min (control 1) while 200 mg/ml of the nonionic polymeric surfactant Hypermer 2296 (Uniqema Wirral, UK), was dissolved in the same monomer mixture by shaking (control 2). AIBN (Camida, Tipperary, Ireland) (1 mol-%) was added to all the freshly prepared suspensions. This was followed by the slow, drop-wise addition of 75 vol.% with respect to total emulsion volume of 5g/L $CaCl_2$ $2H_2O$ aqueous solution under continuous stirring using a vortex mixer (note that 80 vol.% of the same aqueous phase was used to prepare the controls). Finally the stirring rate was increased until an emulsion was formed. In the case of the two control samples, the aqueous solutions were added using experimental setups reported previously.[44, 76] All emulsions were then transferred into 15 ml polypropylene SuperClear™ centrifuge tubes, which were sealed and polymerised in the same way as before to obtain macroporous P(S-co-DVB). The macroporous polymer nanocomposites were removed from the centrifuge tubes and dried in a vacuum oven at 110°C until constant weight.

6.3.3 Characterisation of Nanocomposite Beads and Macroporous Polymers

Scanning Electron Microscopy (LEO Gemini 1525 and JEOL JSM 5610 LV) was used for the microstructural analysis of the nanocomposites macroporous polymers and beads. The macroporous polymers were fractured to reveal the internal surfaces. Pore sizes were measured using the linear intercept method with the software Linear Intercept (TU Darmstadt). A minimum of 150 pores were measured for each sample in order to calculate the characteristic pore sizes (d_{90}, d_{50} and d_{10}) from the cumulative pore size distribution curves.

The skeletal densities ρ_s of the nanocomposites were measured using He displacement pycnometry (Accupyc 1330, Micrometrics Ltd, Dunstable UK) by placing approximately 20 mg of powdered macroporous nanocomposite into a vessel of known volume. The envelope densities ρ_e were calculated from the measured mass m and volume V of cubes of macroporous nanocomposites ($\rho_e=m/V$). The percentage porosity P was calculated using Equation 6-1:

$$P = \left(1 - \frac{\rho_e}{\rho_s}\right) \times 100\%$$

Equation 6-1

Dynamic mechanical properties of the macroporous polymer nanocomposite were investigated using dynamic mechanical analysis (DMA 8000 MA, USA). Specimens were cut to 5×5×5 mm^3 cubes and a controlled strain was applied at a constant frequency of 1 Hz while keeping the temperature constant at 30°C. The storage modulus or stiffness was computed from the amount each specimen deformed.

Uniaxial compressive tests were performed (Lloyds EZ50, Lloyds Instruments Ltd., Fareham, UK) at room temperature following the industrial standard BS ISO 844. The samples were cut into cylinders with a diameter to height ratio of 1 using a

bench saw (Titan SF8R Screwfix). These cylinders were then machined until the edges were parallel. The bottom and top part of each sample was filled with a thin layer of liquid paraffin wax at 60°C and connected to a glass slide. This preparation methodology ensured that the load was homogeneously transferred onto the macroporous nanocomposites during compression. The compression platens were sprayed with Teflon (Rocol, Swllington Leeds UK) prior to each measurement and each specimen was loaded at a crosshead speed of 1 mm/min until a maximum displacement of about 50% was reached or until the specimen fractured abruptly down the centre, whichever occurred first. The Young's modulus was obtained from the slope of the linear portion of the stress-strain curve. The crush strength was calculated from the maximum strength at the end of the initial linear elastic region.

To measure electrical conductivity, macroporous polymer nanocomposites were cut into disks of 13 mm diameter and 5 mm thickness and the upper and bottom surfaces coated with silver paint (Ernest F. Fullam inc). The electrical resistance R of the macroporous polymers was measured using the 2-point method with a digital multimeter (KM-320). The resistivity ρ was calculated taking into account the cross sectional area A and the sample thickness t according to Equation 6-2. The conductivity was then calculated as the inverse of resistivity.

$$\rho = R \times \frac{A}{t}$$

Equation 6-2

6.4 Results and Discussion

Although the focus of this study was the preparation of macroporous polymer nanocomposites from emulsion templates stabilised by the reduced form of GO (rGO), it is valuable to include a sample demonstrating the versatility of GO as

emulsifier for o/w emulsions. A concentration of 0.4 mg/ml was used to prepare homogeneous o/w emulsions with an internal phase (monomers) volume of 40%. The emulsions were then polymerised, washed and dried to yield polymer beads with diameters ranging from 200 – 300 μm (Figure 6-2, left). Using high resolution SEM, GO flakes covering the outer surface of each bead (Figure 6-2, right) were observed. This provides evidence that GO flakes, though initially well-dispersed in the aqueous phase, adsorbed at the o/w interface to lower the interfacial tension, stabilising the emulsion throughout polymerisation. The physical characteristics of these beads are tuneable by changing various parameters such as GO concentration, hence optimising this system; however, this was not the focus of this study and was reserved for future work.

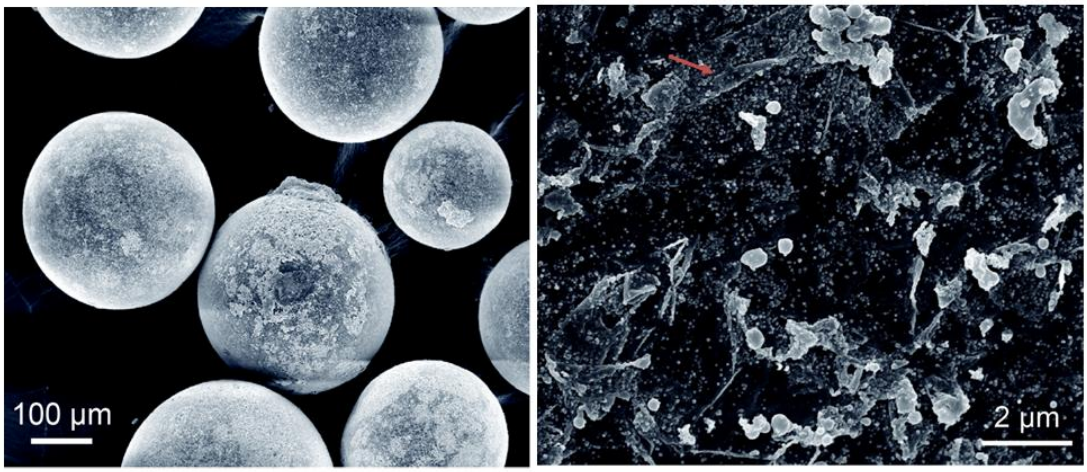

Figure 6-2: SEM of GO-P(S-co-DVB) nanocomposites beads synthesised by polymerising o/w emulsions containing 40 vol.% of internal phase (monomers) dispersed in 0.4 mg/ml GO suspensions. Well-dispersed GO flakes, clearly seen on the surface of the beads, are indicated with an arrow.

The following discussion will focus on the preparation and characterisation of highly porous macroporous polymer nanocomposites by polymerisation of HIPE templates stabilised by the reduced form of GO (rGO). The rGO concentration required to emulsify 75 vol.% water in the organic phase was found to be as low as 0.1 mg/ml (with respect to the organic phase). HIPEs stabilised by such a low rGO

concentration were initially homogeneous but underwent fast droplet coalescence and consequently phase separation, before polymerisation could be completed. This was evident from the separate 'layers' observed when the emulsion was left on the bench at room temperature for about 30 s after preparation (Figure 6-3(a) left). Thus was impossible to produce polyHIPE monoliths required for further characterisation. A close up of the emulsion revealed the extent of droplet coalescence (Figure 6-3(a) right). In comparison to HIPEs stabilised by 0.1 mg/ml rGO, HIPEs prepared with 0.2 mg/ml rGO dispersions remained stable on the bench at room temperature and during the course of polymerisation. Once this 'lower limit' was established, emulsion templates with increasing rGO concentrations (from 0.4 to 5 mg/ml) were prepared to determine its influence on the microstructure and properties of resultant macroporous polymer nanocomposites. The photo of an emulsion stabilised by 1.2 mg/ml of rGO is shown in Figure 6-3(b). A close-up photo shows individual water droplets surrounded by a black-coloured liquid layer containing rGO flakes (Figure 6-3(b) right) in contrast to separate phases previously observed for the HIPEs stabilised with 0.1 mg/ml rGO (Figure 6-3(a)).

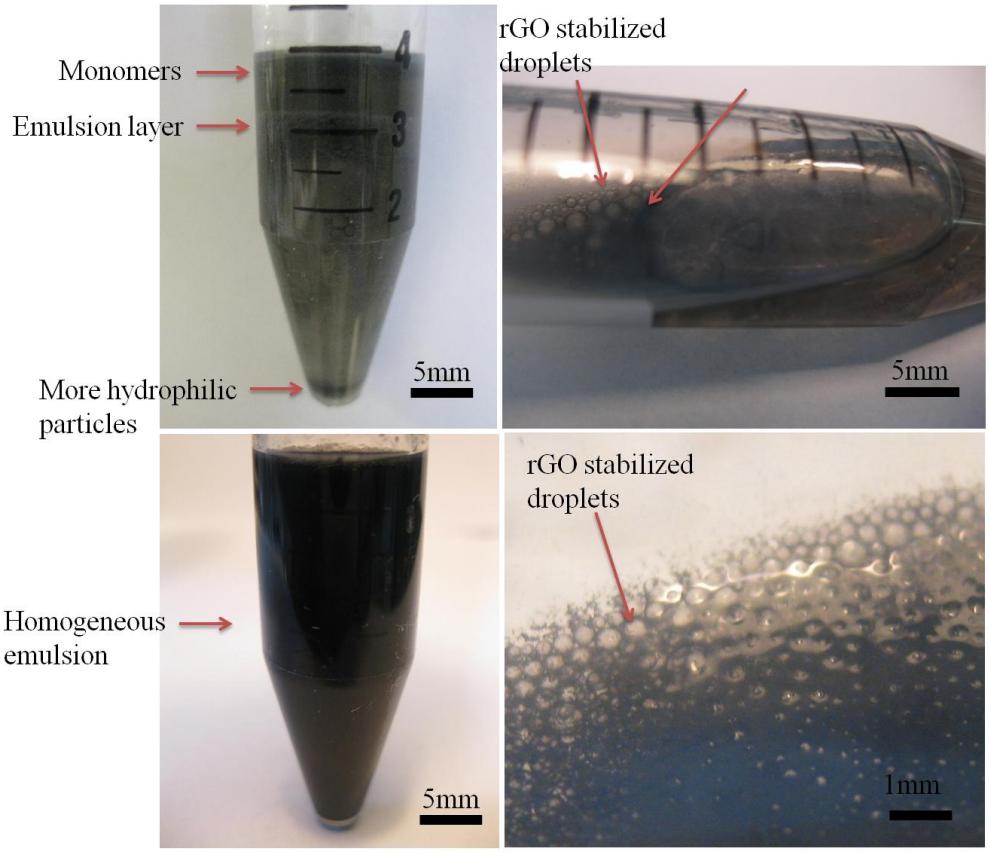

Figure 6-3: Comparing rGO stabilised HIPEs at different concentrations. HIPEs stabilised by 0.1 mg/ml rGO dispersed in the organic phase (top) showed rapid droplet coalescence within 30 s of preparation while HIPEs prepared with 1.2 mg/ml rGO dispersed in the organic phase (bottom) remained stable for at least 30 days on the bench, representative of the behaviour shown by all other HIPEs prepared in this series.

Polymerising the rGO stabilised HIPE templates followed by washing and drying resulted in highly porous rGO-P(S-co-DVB) macroporous polymer nanocomposites. All porosities measured (Table 6-1) were higher than the internal phase volume fraction used to prepare the emulsions (75 vol.%). This was attributed to a combination of the inevitable loss of organic phase via evaporation during dispersion and transfer of the viscous continuous phase between containers as well as the effect of emulsion sedimentation. Skeletal densities (Table 6-1) were constant within error since the very small amounts of rGO added did not significantly change the overall nanocomposite mass. RGO0.2 had the lowest envelope density and consequently the

highest porosity at 86%. Porosity decreased from 86% to 84% as the rGO concentration used to stabilise HIPEs was increased to 0.8 mg/ml due to a reduced rate of emulsion sedimentation. The porosity continued to decrease to 82% for rGO1.2 and remained constant from rGO1.2 to rGO5 as the rate of emulsion sedimentation stabilised.

Table 6-1: Summary of porosity and densities of macroporous rGO-P(S-co-DVB) nanocomposites and control samples 1 and 2. The emulsifier was dispersed in a 1:1 St:DVB solution (25 vol.%) with 1 mol% AIBN and emulsified with 5 g/L of aqueous electrolyte (75 vol.% for rGO and 80 vol.% for the controls). All emulsifier concentrations quoted are with respect to the organic monomer volume.

Specimen name	Emulsifier	Emulsifier concentration (mg/ml)*	Porosity (%)	Skeletal Density (g/cm^3)	Envelope Density (g/cm^3)
rGO 0.2	rGO	0.2	86.0±0.3	1.081±0.007	0.1513±0.0005
rGO 0.4	rGO	0.4	85.5±0.2	1.076±0.007	0.1568±0.0005
rGO 0.8	rGO	0.8	83.8±0.3	1.073±0.003	0.1738±0.0002
rGO 1.2	rGO	1.2	81.7±0.3	1.080±0.009	0.1967±0.0004
rGO 1.6	rGO	1.6	82.7±0.3	1.080±0.007	0.1866±0.0002
rGO 2	rGO	2	81.7±0.2	1.073±0.004	0.1976±0.0007
rGO 2.4	rGO	2.4	83.0±0.3	1.083±0.007	0.1823±0.0007
rGO 5	rGO	5	82.0±0.3	1.081±0.004	0.1946±0.0004
poly-Pickering HIPE 'Control 1'	Titania	25	85±2	1.12±0.02	0.246±0.010
polyHIPE 'Control 2'	Hypermer 2296	200	84±1	1.10±0.03	0.180±0.010

*Calculated with respect to monomer volume.

High resolution SEM was used to elucidate the microstructures of macroporous rGO-P(S-co-DVB) nanocomposites. A representative image of rGO 1.2 is shown Figure 6-4. The pore structure was mainly closed-cell, typical for poly-Pickering-HIPEs.[52, 112] A few pore throats were present across the porous structure alongside areas in the pores that had an obviously thinner polymer wall (seen from the difference in colour contrast on SEM images). This was seen in macroporous polymers made from very concentrated emulsions since the internal phase droplets

were separated by very thin liquid films, which become even thinner during polymerisation.[79]

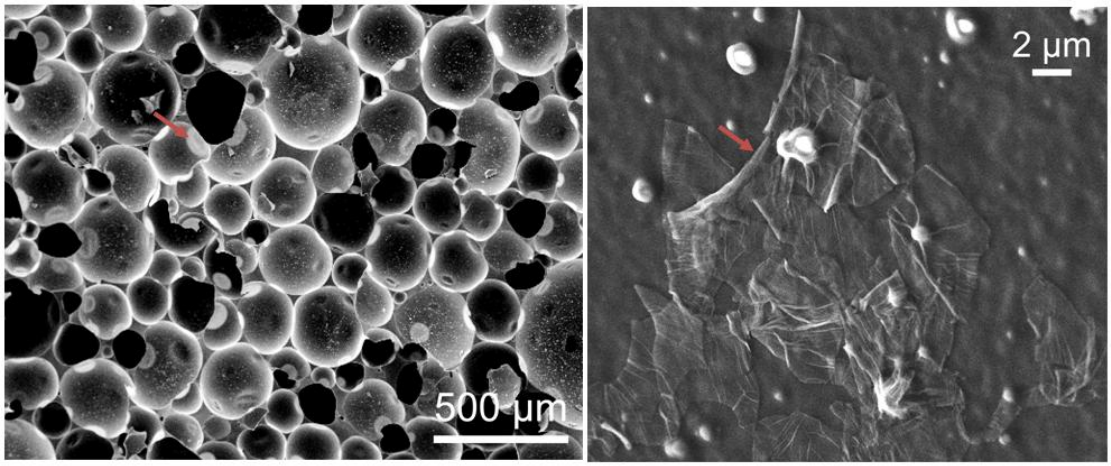

Figure 6-4: SEM of macroporous rGO-P(S-co-DVB) nanocomposite synthesised by the polymerisation of 75 vol.% w/o HIPEs stabilised by 1.2 mg/ml rGO. The nanocomposite macroporous polymer pore throats and the well-dispersed rGO flakes covering the internal surface of the macroporous polymer are indicated with an arrow.

Higher magnification of the pore walls revealed some rGO flakes covering a section of a pore (Figure 6-4, right). Since the emulsion structure was 'frozen' at the gel point of polymerisation, it indicated that rGO did indeed segregate to the w/o interface. The ultrasonication process used to prepare the organic phase for emulsification was effective in dispersing rGO flakes (as no large agglomerates were observed) while maintaining the flake integrity. However, the image suggests that the surface of the pores were not completely covered by a monolayer of rGO flakes. Rather, there were gaps in between noticeable rGO flakes. Any observable flakes were partially folded or adsorbed on the interface as aggregates in a 'pack ice' like manner, stacked on top of one another, a configuration, which was sufficient to stabilise HIPEs.

SEM images were analysed to obtain pore size distributions of the macroporous rGO-P(S-co-DVB) nanocomposite as a function of rGO content, shown in Figure 6-5.

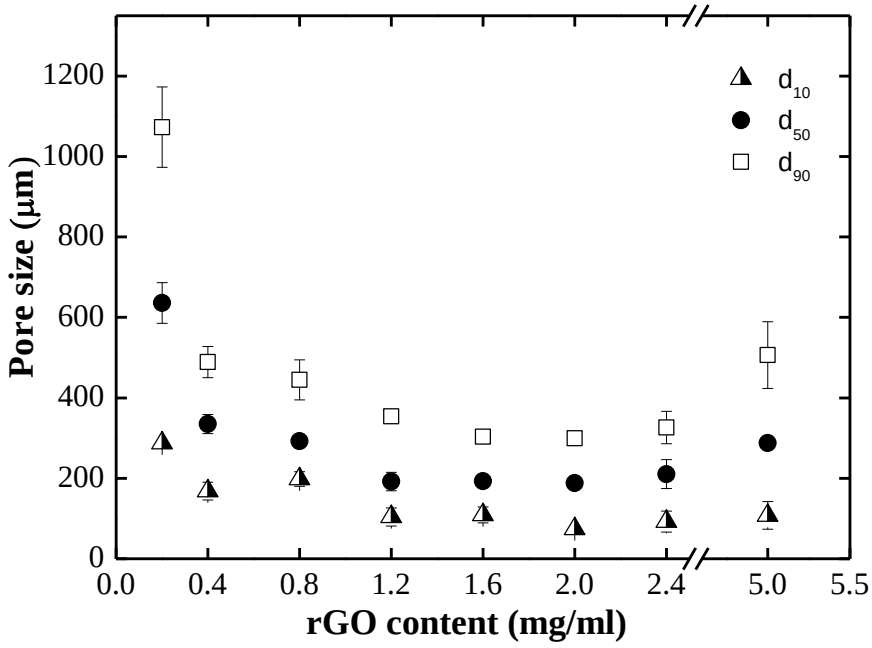

Figure 6-5: Average pore sizes of macroporous rGO-P(S-co-DVB) nanocomposites as function of rGO content. d_{10}, d_{50} and d_{90} correspond to the pore diameter at a cumulative size percentage of 10, 50 and 90% (number distribution), respectively.

Macroporous polymer nanocomposite rGO0.2 presented the largest average pore size at 636 μm with the broadest pore size distribution. This was due to a much faster rate of droplet coalescence experienced by HIPEs stabilised by such a low concentration of rGO flakes. The pore size distributions became narrower and the average pore size smaller as the rGO concentration increased since more rGO was available to cover the surface of smaller droplets, slowing down the rate of droplet coalescence. A minimum average pore size of 192 μm was reached for rGO1.2 and stayed constant as the rGO concentration used to stabilise HIPEs increased until 2 mg/ml (rGO2). When the rGO concentration in HIPEs was increased further to 5 mg/ml (rGO5), the pore size distributions became broader (Figure 6-5). At concentrations as high as 2.4 to 5 mg/ml, the amount of energy supplied during ultrasonication was no longer sufficient to completely disperse rGO in the organic phase. As a result, flakes tended to agglomerate, reducing their effectiveness to stabilise small droplets.

A combination of compression testing and dynamic mechanical analysis (DMA) was used to determine the mechanical properties of the macroporous polymer nanocomposites. Results from these mechanical tests serve to explain the influence of rGO concentration and pore morphology on the crush strength, Young's modulus and storage modulus of the macroporous polymer nanocomposites. As control samples, conventional poly-Pickering-HIPEs prepared by the polymerisation of emulsion templates stabilised by a particulate emulsifier (control 1) and a surfactant (control 2), prepared using an emulsion system consisting of water (80%) in a 1:1 (by volume) mixture of St to DVB (20%) were chosen. This resulted in controls with porosities in the same range as those of the rGO samples reported herein. Porosities, skeletal and envelope densities of the control samples are summarised in Table 6-1. The crush strength and the Young's modulus were determined from stress-strain profiles obtained from compression testing and summarised in Figure 6-6.

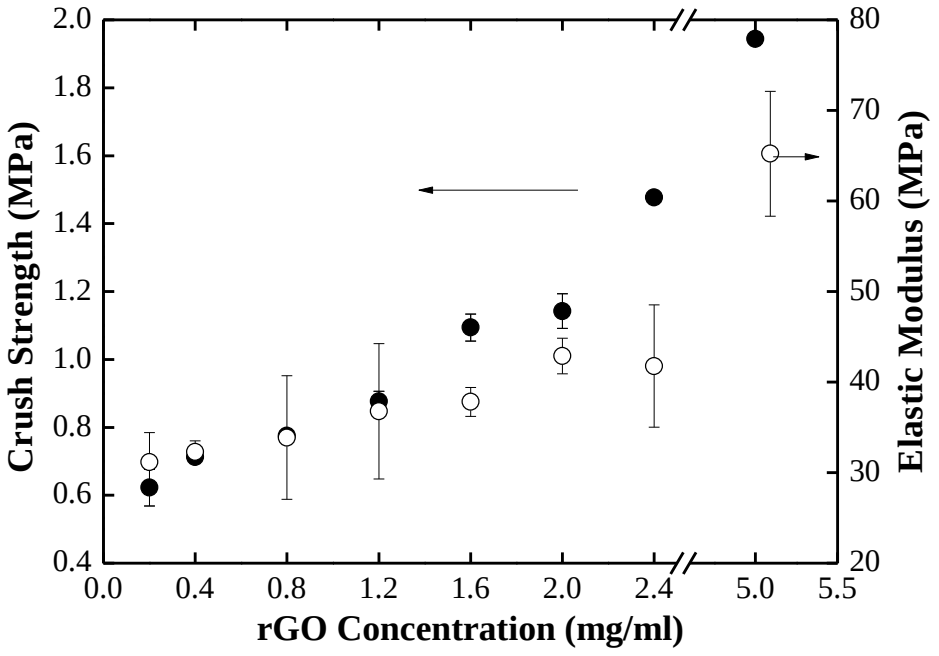

Figure 6-6: Crush strength and Young's modulus of macroporous rGO-P(S-co-DVB) nanocomposites as function of rGO concentration in the organic phase.

Both crush strength and Young's modulus showed a general increase with increasing rGO concentration. As the concentration of rGO dispersed in the polymer matrix increased, the wrinkly and creased rGO flakes mechanically interlocked with themselves and other flakes within the polymer matrix in a favourable configuration, creating a secondary structure which improved the load transfer of the entire macroporous polymer during compression, resulting in the generally increasing trend. The crush strength of the macroporous polymer nanocomposites prepared from HIPEs stabilised by 0.2 mg/ml (rGO0.2) and 1.2 mg/ml (rGO1.2) increased by 41%. The reason for this improvement was a combination of the decrease in porosity (Table 6-1) and average pore size (Figure 6-5) in addition to the reinforcing effect of rGO. Increasing the rGO concentration in HIPEs from 1.2 mg/ml to 2 mg/ml (rGO1.2 to rGO2) resulted in a further increase of the crush strength of the produced macroporous polymer nanocomposites by 30%. Since the average pore size plateaued at 190 μm (Figure 6-5) and porosity remained constant, this provided evidence for the significant, reinforcing effect of rGO. The pore size distribution broadened (Figure 6-5) while porosity remained constant in the polyHIPEs produced from HIPEs stabilised by rGO concentrations ranging from 2 mg/ml to 5 mg/ml (rGO2 to rGO5) (Table 6-1). In this range, the crush strength increased the most, by 70%. Besides the reinforcing effect of rGO for rGO2 to rGO5, the broadly distributed pore sizes in a hierarchical pore arrangement (Figure 6-7) led to the improvement in crush strength observed. It has previously been shown that when there is a combination of larger and smaller pores for structures with the same porosity, the hierarchical arrangement enhances the mechanical properties as it is believed to improve the load transfer mechanism during compression.[113]

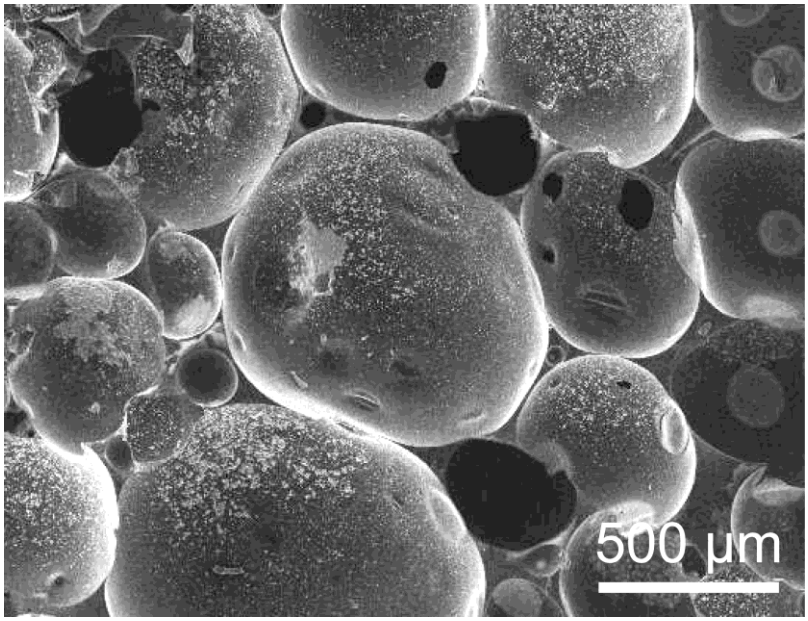

Figure 6-7: SEM of macroporous rGO-P(S-co-DVB) nanocomposite synthesised by the polymerisation of 75 vol.% w/o HIPEs stabilised by 5 mg/ml rGO.

Control 1, a poly-Pickering-HIPE synthesised from a w/o HIPE stabilised by oleic acid modified titania, had a crush strength of 3.2 ± 0.8 MPa, 65% higher than the maximum achieved by rGO5. This came as no surprise as a much higher concentration (by one magnitude) of emulsifying particles imparted also a significant reinforcing effect on the polymer matrix, which manifested itself in a higher crush strength. However when compared with rGO5, the Young's modulus of control 1 is still 68% lower at 21 ± 3 MPa despite possessing a similar porosity. Control 2, a conventional polyHIPE obtained by the polymerisation of a HIPE stabilised using 200 mg/ml of a non-ionic polymeric surfactant (Hypermer 2296), had a 55% lower Young's modulus at 29 ± 4 MPa and 23% lower crush strength at 1.5 ± 0.2 MPa compared to that of rGO5,[201] Moreover, any surfactant remaining in the polyHIPE is likely to act as a plasticizer and the presence of interconnecting pore throats also weakened the overall porous structure.[113] As such, rGO was not only a more efficient emulsifier at lower concentrations, it also resulted in better Young's moduli and crush strengths of poly-Pickering-HIPEs (in the case of control 2) when compared to

porous materials prepared via conventional emulsion templating using particle stabilised and surfactant stabilised emulsions.

Generally, the storage modulus was seen to show the same trend as the crush strength and storage modulus with increasing rGO concentration (Figure 6-8). Due to the extremely brittle nature of samples prepared with 0.2 mg/ml stabilised HIPEs (rGO0.2), it was difficult to cut and measure the storage modulus accurately and so the data was excluded. However, it was interesting to note that doubling the rGO concentration in HIPE templates from 0.4 mg/ml to 0.8 mg/ml already resulted in an order of magnitude increase in the storage modulus. An increase in rGO concentration from 0.8 mg/ml to 5 mg/ml (rGO0.8 to rGO5) further doubled the stiffness. This was a result of a combination of the reinforcing effect of increased rGO in the polymer matrix as well as the positive influence of pore size and arrangement on the storage modulus. In comparison, both controls 1 and 2 had significantly lower storage moduli; 77% lower at 11 ± 9 MPa for control 1 and 66% lower at 16 ± 3 MPa for control 2 compared to the maximum storage modulus recorded amongst the poly-Pickering-HIPEs prepared from rGO stabilised HIPEs (47 ± 3 MPa for rGO5).

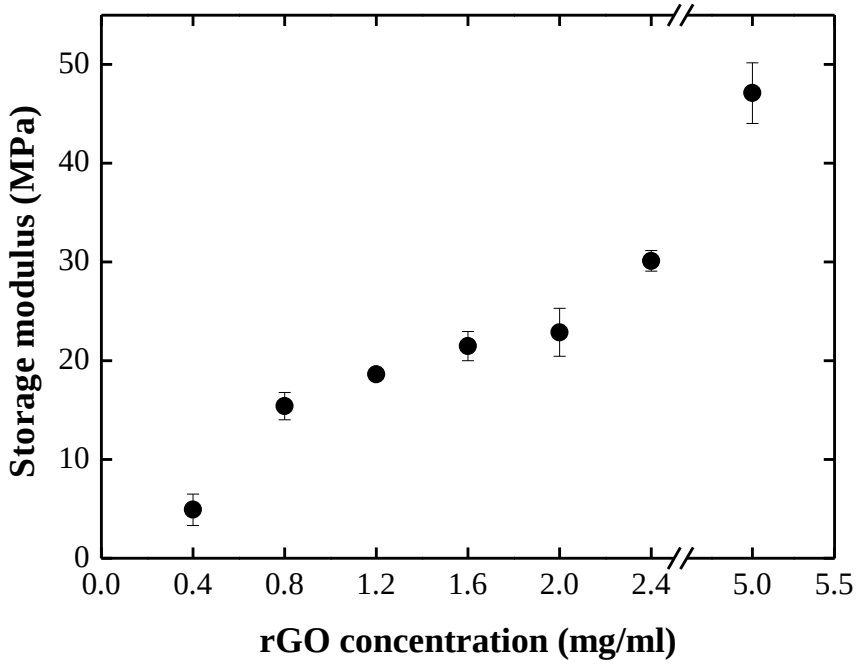

Figure 6-8: Storage modulus of macroporous rGO-P(S-co-DVB) nanocomposites as function of rGO concentration (with regards to organic phase) obtained from dynamic mechanical analysis at constant temperature of 30°C.

Since CMG has a very low, reported percolation threshold of 0.1 vol.%,[161] it is a highly efficient nanofiller to prepare conductive, dense composites. However, there are no previous reports on the percolation behaviour of CMG in macroporous materials. The electrical conductivity of macroporous nanocomposite with varying concentrations of rGO are displayed in Figure 6-9 to determine the percolation threshold.

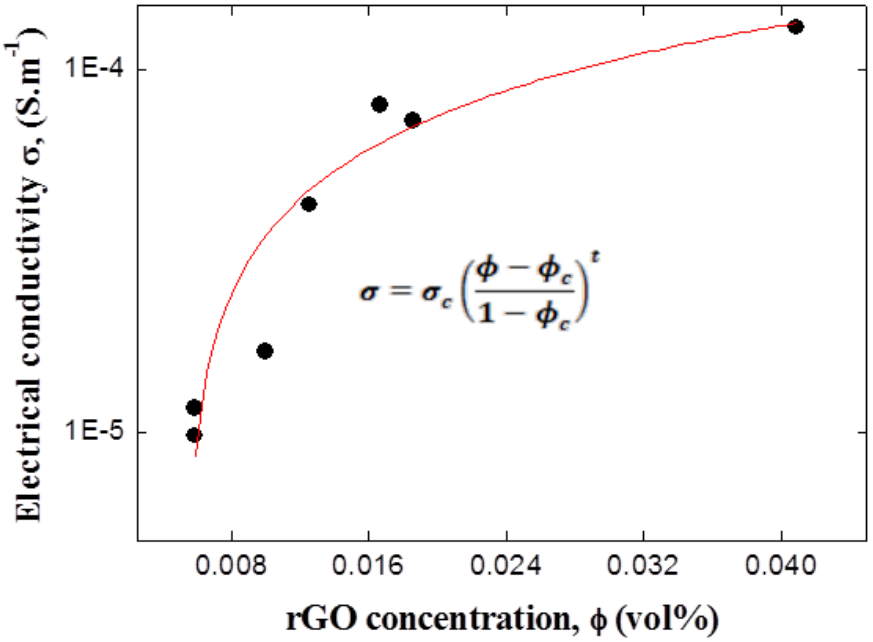

Figure 6-9: Conductivity of macroporous rGO-P(S-co-DVB) nanocomposites σ as a function of rGO volume fraction ϕ_c (with respect to the total volume of the macroporous nanocomposites). The solid line is the fit of experimental data to the conductivity equation (inserted equation in Figure 6-9),[202] where σ_c is the conductivity of the filler, ϕ_c is the percolation threshold and t percolation exponent. The fitted parameters are: ϕ_c=0.005 vol.%, σ_c=0.020, t=0.7. rGO volume fraction in the macroporous polymers (vol.%) are calculated using the value of 2.2 g/cm^3 as the density of rGO.[161]

PolyHIPEs rGO0.2 and rGO0.4 were non-conductive, i.e. insulators, rGO 0.8 (corresponding to a filler content of 0.006 vol.% rGO in the macroporous nanocomposite) presented an antistatic response with a conductivity of 1.2 10^{-5} Sm^{-1}. Further increasing the concentration of rGO led to a gradual increase of electrical conductivity up to 1.3 10^{-4} Sm^{-1} for the sample with the highest rGO concentration studied here (rGO5, with 0.0041 vol.% rGO).

The percolation threshold ϕ_c extracted from a fitting of the measured conductivity data to the conductivity equation is 0.005 vol.%. Since these conductive macroporous materials are highly sought after for many industrial applications,[170, 203-206] the percolation behaviour of macroporous rGO-P(S-co-DVB) nanocomposites

were studied and compared with dense CMG polystyrene nanocomposites previously reported.[161] It was observed that the macroporous materials developed in this study had a percolation threshold which was two orders of magnitude lower. This was potentially due to the efficient assembly of rGO flakes into a network during the emulsion templating process. Since rGO aligned at the o/w interface during emulsification, an 'ordered' segregation of flakes to the o/w interface was favoured. This created a 'shell' of connected rGO flakes, which froze into position during the polymerisation. In addition, the presence of interconnected rGO flakes dispersed in a suitable orientation within the polymer matrix further facilitated the formation of a continuous, conductive network at much lower concentrations compared to dense nanocomposites.

6.5 Conclusions

The multi-functionality of graphene oxide flakes both as an emulsifier and a conductive nanoreinforcement was utilised for the formulation of emulsion templated nanocomposite beads and macroporous polymers. By using very hydrophilic GO (synthesised using a modified Hummers method) as the emulsifier, o/w emulsions were prepared with a pure monomer oil phase dispersed in 0.4 mg/ml GO aqueous suspensions. After polymerisation and vacuum drying, nanocomposite beads with diameter size ranging from 200-300 μm were obtained. However, the true challenge was to tune the hydrophobicity of GO in order to produce w/o HIPEs that would act as a template for the synthesis of macroporous polymers. It was found that rGO, produced by controlled thermal reduction of GO, allowed the successful preparation of rGO-stabilised w/o HIPEs. These HIPEs remained stable over the course of polymerisation at 70°C for 24 h without phase separating. Following polymerisation and vacuum drying, highly porous closed cell macroporous polymers

with interesting properties were produced. The mechanical interlocking of the rGO flakes in the polymer matrix created structural networks which were able to provide increased mechanical resistance to compression. The developed materials showed an impressive increase in the storage modulus by an order of magnitude just by doubling the amount of rGO in HIPE templates from 0.4 to 0.8 mg/ml. The maximum Young's and storage moduli determined for poly-rGO-stabilised-HIPEs were also significantly higher compared to those for control samples prepared particulate and surfactant stabilised HIPEs.

Despite the low rGO loading of the macroporous materials produced, they had an extremely low percolation threshold of 0.005 vol% compared to dense nanocomposites previously studied, providing evidence of the efficient arrangement of rGO within the polymer matrix to aid emulsification yet maintain a conducting network of flakes. This is a potentially viable method to manufacture closed-cell macroporous polymer nanocomposites with conductive properties attractive for a range of specialty applications, avoiding the use of large concentrations of expensive surfactants.

7 Conclusions and Suggestions for Future Work

7.1 Summary of Findings

Emulsion templating, a versatile method to produce bespoke porous materials, was explored as a viable way to synthesise hierarchical macroporous polymers in this thesis. The main aim of this work was to produce hierarchical macroporous polymers inspired by those found in nature such as hardwood and bone, using the emulsion templating technique. The type of hierarchical porous materials produced was further classified into two types. Firstly, the production of materials displaying hierarchy at the macroporous level, which was achieved by optimising current protocols for emulsion templating, described in Chapter 3, the use of a mixed particle and surfactant emulsifier system in Chapter 4 and by mechanically frothing bio-based emulsion templates in Chapter 5. The second type of hierarchical porous materials displayed hierarchy at the particle network level. This was described by the interconnected conductive particulate network of rGO flakes found in the macroporous nanocomposites in Chapter 6. Characterisation of the macroporous polymers produced using the approaches mentioned above were reported and discussed in comparison with non-hierarchical macroporous polymers to demonstrate the effectiveness of hierarchy on the physical properties of the final porous material. The findings are summarised as follows:

7.1.1 Hierarchical PolyHIPEs Synthesised from Surfactant-Stabilised Emulsion Templates

By optimising selected emulsification parameters such as stirring rate and emulsifier concentration, hierarchical, opened-cell macroporous polymers with multi-modal pore size distributions packed in an efficient arrangement were produced. Just as

lattice girders in buildings support its main frame, the hierarchical arrangement of pores was believed to provide additional structural integrity to the porous materials, facilitating the transfer of load and improving its overall mechanical properties. Hierarchical polyHIPEs produced from HIPEs containing a 1:1 mixture of styrene and DVB in the continuous phase stabilised by 5 vol.% surfactant (Hypermer 2296) showed a 93% improvement in Young's moduli compared to conventional polyHIPEs produced from HIPEs stabilised by 20 vol.% of surfactant with the same porosity of 84%. A 2D simulation study using FEM showed qualitatively that the geometry with a hierarchical arrangement had a higher Young's modulus during compression, validating the experimentally obtained results. The study showed that the macroporous polymers with hierarchically arranged pores did indeed display better mechanical properties.

7.1.2 Macroporous Polymers with Hierarchical Pore Structure from Emulsion Templates Stabilised by Both Particles and Surfactants

A mixed surfactant and particle emulsifier system was used to prepare high internal phase w/o emulsions, composed of a continuous phase containing the monomer styrene and flexible crosslinker PEGDMA. The surfactant (Hypermer B246SF) was added simultaneously to the continuous phase containing dispersed particles (titania particles modified with 3.5 ± 0.1 wt% oleic acid), producing a mixture of large and small emulsion droplets which polymerised into a hierarchical macroporous structure. Characteristics of both poly-Pickering-HIPEs (predominantly closed pores) and conventional polyHIPEs (interconnected open pores) could be seen in SEM images of the hierarchical macroporous polymers. TEM of very thin sections of the macroporous polymers located the particles in the polymer matrix. From this, it was inferred that the hierarchical pore structure was a result of predominantly particle-

stabilised emulsion droplets and surfactant-stabilised droplets that co-existed with one another at the gel point of polymerisation. It was found that within the series of hierarchical macroporous polymers with the same porosity of 79%, samples prepared with 0.8 w/vol.% of surfactants and 0.8 w/vol.% of particles (both with respect to the monomer volume) had the highest crush strength and Young's modulus, at 3.6 MPa and 27 MPa respectively despite a high gas permeability of 0.67 D. This measured value of crush strength and Young's modulus was 3-4 times higher compared to conventional surfactant stabilised structures which also had a comparatively lower permeability of 0.13 D. This noticeable improvement in mechanical properties despite a higher gas permeability and pore throat interconnectivity was attributed to efficient packing of pores in a hierarchical configuration. Thus, macroporous hierarchy was shown to enhance mechanical strength while maintaining a higher gas permeability, making this material attractive for applications where both mechanical strength and interconnectivity are important.

7.1.3 Air in Water-in-oil Emulsion Templates: Developing Highly Porous Greener Hierarchical Macroporous Nanocomposite Foams

A viscous w/o 50% medium internal phase emulsion system was prepared using a titania stabilised Pickering emulsion template composed of a continuous phase containing varying volumes of bio-based AESO monomer, TMB (diluent), styrene and PEGDMA (cross-linkers). The emulsion templates were mechanically frothed using a hand-held electric mixer to incorporate air bubbles into the emulsion template. Both emulsion droplets and air bubbles acted as 'templates' for the final porous structure. After polymerisation, bio-based macroporous polymers with a high porosity of 81%, displaying a hierarchical pore arrangement were produced. These materials showed higher porosity than typical polyMIPEs prepared using Pickering

emulsion templates stabilised by the same 3 w/vol.% of particles, due to the hierarchical packing of macro-pores. The microstructures of these highly porous materials both before and after mechanical frothing shed insight on the stabilisation mechanisms that occurred during the mechanical frothing of emulsions. This included the importance of continuous phase viscosity on the emulsion stability as well as its ability to trap air bubbles created during the mechanical frothing process. The temperature at which a peak in the tanδ was observed was also seen to increase with decreasing AESO concentration, from 89°C (50% AESO) to 105°C (30% AESO).

7.1.4 Nanocomposite Macroporous Polymers and Beads Synthesised from Emulsion Templates Stabilised by Chemically Modified Graphene

Nanocomposite beads and solid foams were produced using emulsion templates stabilised by a network of 2D graphene oxide flakes acting both as particulate emulsifiers as well as conductive nano-reinforcements. By first using hydrophilic GO (synthesised using a modified Hummers method) as an emulsifier, o/w emulsions were prepared with 0.4 mg/ml GO-aqueous suspensions emulsified with a styrene-DVB containing continuous phase. After polymerisation and vacuum drying, nanocomposite beads with diameter size ranging from 200-300 μm were obtained. RGO, produced by controlled thermal reduction of GO, was used to prepare rGO-stabilised w/o HIPEs which were polymerised to form highly porous closed cell macroporous polymers. An increase in the storage modulus by an order of magnitude was achieved just by increasing the amount of rGO in the HIPE templates from 0.4 to 0.8 mg/ml. The maximum Young's modulus and crush strength determined for poly-rGO-stabilised-HIPEs (5 mg/ml of rGO) was significantly higher by 55% and 23% respectively compared to those for control samples with the same porosity,

prepared using conventional surfactant stabilised HIPEs (200 mg/ml Hypermer 2296). Macroporous materials produced also showed a low percolation threshold of 0.005 vol% compared to dense nanocomposites previously studied. This provided evidence of the efficient arrangement of rGO and presence of a hierarchical network of flakes within the polymer matrix.

7.2 Future work

7.2.1 Optimising Hierarchical PolyHIPEs Synthesised from Surfactant-Stabilised Emulsion Templates

- *Test hierarchical hypothesis on alternative monomer systems*

  Optimising emulsification parameters such as the concentration of surfactant and emulsification time showed a profound effect on the droplet structure of the emulsion templates (as seen in Chapter 3). It was possible to demonstrate improvements in mechanical properties due to the presence of a hierarchical structure. However, mechanical properties were still limited by the inherent properties (brittleness) of highly crosslinked polystyrene-co-DVB. A next step would be to optimise the crosslink density or test alternative monomer systems which will yield to materials with better mechanical properties. Possible options for the continuous phase include PEGDMA or even tough resin systems such Bisphenol A.

- *Develop the current 2D mathematical model*

  In Chapter 3, a 2D computational model was assumed, which provided qualitative comparisons with our measured data. This would serve as a springboard for further efforts directed at building 3D models which would not only account for the pore arrangement (hierarchical vs. non-hierarchical) but also the effects of pore throats on the overall mechanical properties of

simulated macroporous polymers. Furthermore, a range of values were input to the current 2D model to generate results. To improve the model, it is suggested that the bulk modulus and crush strength of crosslinked polystyrene-co-DVB films are measured and used input values. This will generate a more realistic, quantitative model for future purposes.

7.2.2 Further Characterisation of Hierarchical Macroporous Polymers from Emulsion Templates Stabilised by Particles and Surfactants

- *Dependency of emulsion structure on particle-surfactant interactions*

  It was found that by adding surfactants simultaneously to a particle-containing continuous phase resulted in the particle arrangement as shown in Figure 4-2 in Chapter 4. Further research could be directed at understanding how particles are arranged at the oil-water interface based on the order at which the surfactant is added. Other factors such as the time allowed for emulsification could also play a part on the final emulsion droplet arrangement and hence final pore arrangement. To take this a step further, the components of the monomer phase could also be varied and its effect on the particle-surfactant interaction studied as a part of this investigation. This would be useful to understand the particle-surfactant interactions occurring during emulsification and its effect on the formation of hierarchical structures.

- *Determination of liquid permeability of macroporous polymers*

  The work in Chapter 4 highlighted the gas permeability of hierarchical macroporous polymers produced. The size of the flow limiting pore throat was inferred from a combination of the gas permeability measurements as well as the pore throat size distribution. It is suggested that the flow limiting

pore throats are quantified and compared using the integrated apparatus for mercury penetration permeability, previously reported by Manley et al.[76]

7.2.3 Developing Highly Porous Hierarchical Macroporous Nanocomposites by Mechanically Frothing Viscous Emulsions

- *Determination of emulsion rheology*

  Although the focus was on the characterisation of the macroporous polymers, the viscosity of the emulsion templates used to prepare the macroporous polymers in Chapter 5 was observed to have a noticeable effect on emulsion stability and the emulsions ability to trap air bubbles. A more detailed study of the emulsion rheology (viscosity, shear modulus and yield stress) would be of interest to quantify the effect of emulsion rheology on the final droplet hierarchy.

- *Investigating the feasibility of alternative bio-based monomers*

  In Chapter 5, AESO was found to display a peak in the tanδ curve close to room temperature, which resulted in issues with shrinkage and cracking during the post-polymerisation purification process. To minimise these problems, the existing drying protocol was modified from the use of a convection oven at 120°C to a freeze-drying technique, which was maintained at -196°C. The size of the container used for freeze-drying limited the size of the samples that could be dried completely. This drying protocol is also not economical when considering the scaled-up production of these materials. Thus, research efforts should be directed at seeking alternative bio-based monomer(s) with a higher T_g (yet compatible polarity and viscosity) to overcome these challenges.

7.2.4 Graphene Oxide Hierarchical Macroporous Nanocomposites

- *Exploring further GO Properties*

  During the course of the work described in Chapter 6, it was discovered that the surface properties of GO was sensitive to environmental factors such as temperature, exposure to light and atmosphere, which affected the hydrophobicity of GO and hence its emulsifying properties. Thus, it would be interesting to investigate the changes in GO surface active properties with respect to some of the environmental factors state above, such as reduction temperature and controlled exposure to light (UV rays). An investigative study on the changes in interfacial tension (measured using pendant drop analysis or Du Noüy ring) could be carried out to quantify these effects. Following which macroporous nanocomposites could be produced using GO flakes with varying surface functionalities and its effect on the pore size distribution, conductivity, and mechanical properties etc., studied in a systematic way.

- *Visualising the arrangement of GO in polymer matrix*

- In addition to the SEM images presented in Chapter 6, the visualisation of the hierarchical arrangement of GO within the polymer matrix could be further explored by TEM. In particular, the use of electron diffraction to determine the presence of graphene oxide at or near the pore walls. This could provide an understanding of the arrangement of GO across the polymer matrix.

  The above mentioned works will be undertaken as part of a collaborative study on ‘Graphene three-dimensional networks’ with Professor Kang Li from the Department of Chemical Engineering, Imperial College London, in a follow-on project funded by the EPSRC.

Bibliography

1. IUPAC, *IUPAC Manual of Symbols and Terminology for Physicochemical Quantities and Units*, Butterworths, London, **1972**.

2. C. Zhao, E. Danish, N. R. Cameron and R. Kataky, *Journal of Materials Chemistry*, **2007**, *17*, 2446-2453.

3. M. Ottens, G. Leene, A. A. C. M. Beenackers, N. Cameron and D. C. Sherrington, *Industrial and Engineering Chemistry Research*, **1999**, *39*, 259-266.

4. E. M. Christenson, W. Soofi, J. L. Holm, N. R. Cameron and A. G. Mikos, *Biomacromolecules*, **2007**, *8*, 3806-3814.

5. L. D. Harris, B.-S. Kim and D. J. Mooney, *Journal of biomedical materials research*, **1998**, *42*, 396-402.

6. Y. S. Nam, J. J. Yoon and T. G. Park, *Journal of biomedical materials research*, **2000**, *53*, 1-7.

7. M.-T. Liang and C.-M. Wang, *Industrial and Engineering Chemistry Research*, **2000**, *39*, 4622-4626.

8. N. Cameron and D. Sherrington, *High Internal Phase Emulsions (HIPEs) — Structure, Properties and Use in Polymer Preparation*, Springer Berlin / Heidelberg, **1996**.

9. G. Lu, G. Q. Lu and Z. M. Xiao, *Journal of Porous Materials*, **1999**, *6*, 359-368.

10. R. Lakes, *Nature*, **1993**, *361*, 511-515.

11. C. H. Turner, *Osteoporosis International*, **2002**, *13*, 97-104.

12. K. Rezwan, Q. Z. Chen, J. J. Blaker and A. R. Boccaccini, *Biomaterials*, **2006**, *27*, 3413-3431.

13. A. C. Wiedenhoeft and R. B. Miller, *Handbook of Wood Chemistry and Wood Composites* CRC Press, **2005**.

14. E. N. Jaynes, *Encyclopedia of Emulsion Technology*, Marcel Dekker, New York **1985**.

15. H. Karbstein, Ph.D. Thesis, University of Karlsruhe, **1994**.

16. A. Bismarck, personal communication, **2009**.

17. M. P. Aronson and M. F. Petko, *Journal of Colloid and Interface Science*, **1993**, *159*, 134-149.

18. W. D. Bancroft, *The Journal of Physical Chemistry*, **1913**, *17*, 501-519.

19. K. J. Lissant, *Journal of Cosmetic Chemists*, **1970**, *21*, 141 - 154.

20. H. M. Princen, *Journal of Colloid and Interface Science*, **1985**, *105*, 150-171.

21. H. M. Princen and A. D. Kiss, *Journal of Colloid and Interface Science*, **1989**, *128*, 176-187.

22. R. A. Mugele and H. D. Evans, *Industrial and Engineering Chemistry*, **1951**, *43*, 1317-1324.

23. P. González-Tello, F. Camacho, J. M. Vicaria and P. A. González, *Powder Technology*, **2008**, *186*, 278-281.

24. E. Jurado, V. Bravo, F. Camacho, J. M. Vicaria and A. Fernández-Arteaga, *Colloids and Surfaces A: Physicochemical and Engineering Aspects*, **2007**, *295*, 91-98.

25. A. Sood and S. K. Awasthi, *Journal of Applied Polymer Science*, **2003**, *88*, 3058-3065.

26. K. G. Hollingsworth and M. L. Johns, *Journal of Colloid and Interface Science*, **2003**, *258*, 383-389.

27. R. J. Carnachan, M. Bokhari, S. A. Przyborski and N. R. Cameron, *Soft Matter*, **2006**, *2*, 608-616.

28. D. D. Eley, M. J. Hey and J. D. Symonds, *Colloids and surfaces*, **1988**, *32*, 87-101.

29. H. Zhang and A. I. Cooper, *Soft Matter*, **2005**, *1*, 107-113.

30. A. Mandal, A. Samanta, A. Bera and K. Ojha, *Industrial and Engineering Chemistry Research*, **2010**, *49*, 12756-12761.

31. J. N. Phillips, *Transactions of the Faraday Society*, **1955**, *51*, 561-569.

32. P. Walstra, *Chemical Engineering Science*, **1993**, *48*, 333-349.

33. W. C. Griffin, *Journal of the Society of Cosmetic Chemists*, *1*, 311-326.

34. L. L. Schramm, *Emulsions, Foams and Suspensions: Fundamentals and Applications*, Wiley-VCH **2005**.

35. E. Ruckenstein, *Langmuir*, **1996**, *12*, 6351-6353.

36. S. U. Pickering, *Journal of the Chemical Society, Transactions*, **1907**, *91*, 2001-2021.

37. W. Ramsden, *Physiologische Abtheilung*, **1903**, 5170-5534

38. V. O. Ikem, A. Menner, T. S. Horozov and A. Bismarck, *Advanced Materials*, **2010**, *22*, 3588-3592.

39. J. Frelichowska, M.-A. Bolzinger, J. Pelletier, J.-P. Valour and Y. Chevalier, *International Journal of Pharmaceutics*, **2009**, *371*, 56-63.

40. B. P. Binks, *Current Opinion in Colloid and Interface Science*, **2002**, *7*, 21-41.

41. T. N. Hunter, R. J. Pugh, G. V. Franks and G. J. Jameson, *Advances in Colloid and Interface Science*, **2008**, *137*, 57-81.

42. R. Aveyard, B. P. Binks and J. H. Clint, *Advances in Colloid and Interface Science*, **2003**, *100-102*, 503-546.

43. B. P. Binks and S. O. Lumsdon, *Physical Chemistry Chemical Physics*, **1999**, *1*, 3007-3016.

44. V. O. Ikem, A. Menner and A. Bismarck, *Langmuir*, **2010**, *26*, 8836-8841.

45. A. Menner, R. Verdejo, M. Shaffer and A. Bismarck, *Langmuir*, **2007**, *23*, 2398-2403.

46. N. P. Ashby and B. P. Binks, *Physical Chemistry Chemical Physics*, **2000**, *2*, 5640-5646.

47. B. P. Binks and S. O. Lumsdon, *Langmuir*, **2001**, *17*, 4540-4547.

48. A. Menner, R. Powell and A. Bismarck, *Soft Matter*, **2006**, *2*, 337-342.

49. E. F. Vansant, P. Van Der Voort and K. C. Vrancken, *Characterization and Chemical Modification of the Silica Surface*, Elsevier Science, **1995**.

50. E. Bourgeat-Lami, P. Espiard and A. Guyot, *Polymer*, **1995**, *36*, 4385-4389.

51. X. K. Ma, N. H. Lee, H. J. Oh, J. W. Kim, C. K. Rhee, K. S. Park and S. J. Kim, *Colloids and Surfaces A: Physicochemical and Engineering Aspects*, **2010**, *358*, 172-176.

52. V. O. Ikem, A. Menner and A. Bismarck, *Angewandte Chemie International Edition*, **2008**, *47*, 8277-8279.

53. G. Blyholder, C. Adhikar and A. Proctor, *Colloids and Surfaces A: Physicochemical and Engineering Aspects*, **1995**, *105*, 151-158.

54. P. M. Kruglyakov and A. F. Koretsky, *Doklady Akademii nauk SSSR*, **1971**, *197*, 1106.

55. D. Megias-Alguacil and L. J. Gauckler, *AIChE Journal*, **2009**, *55*, 1103-1109.

56. D. Megias-Alguacil and L. Gauckler, *Colloid and Polymer Science*, **2010**, *288*, 133-139.

57. T. Horozov, B. P. Binks and B. Binks, *Angewandte Chemie International Edition*, **2006**, *45*, 773-776.

58. E. Vignati, R. Piazza and T. P. Lockhart, *Langmuir*, **2003**, *19*, 6650-6656.

59. A. Drelich, F. Gomez, D. Clausse and I. Pezron, *Colloids and Surfaces A: Physicochemical and Engineering Aspects*, **2010**, *365*, 171-177.

60. S. Levine, B. D. Bowen and S. J. Partridge, *Colloids and surfaces*, **1989**, *38*, 325-343.

61. N. Glaser, D. J. Adams, A. Böker and G. Krausch, *Langmuir*, **2006**, *22*, 5227-5229.

62. J. Kim, L. J. Cote, F. Kim, W. Yuan, K. R. Shull and J. Huang, *Journal of the American Chemical Society*, **2010**, *132*, 8180-8186.

63. P. Mulqueen, *Advances in Colloid and Interface Science*, **2003**, *106*, 83-107.

64. H. Hassander, B. Johansson and B. Törnell, *Colloids and surfaces*, **1989**, *40*, 93-105.

65. B. P. Binks, J. A. Rodrigues and W. J. Frith, *Langmuir*, **2007**, *23*, 3626-3636.

66. B. P. Binks and J. A. Rodrigues, *Langmuir*, **2007**, *23*, 7436-7439.

67. J. Wang, F. Yang, J. Tan, G. Liu, J. Xu and D. Sun, *Langmuir*, **2009**, *26*, 5397-5404.

68. C. Vashisth, C. P. Whitby, D. Fornasiero and J. Ralston, *Journal of Colloid and Interface Science*, **2010**, *349*, 537-543.

69. N. Ghouchi Eskandar, S. Simovic and C. A. Prestidge, *Physical Chemistry Chemical Physics*, **2007**, *9*, 6426-6434.

70. C. P. Whitby, D. Fornasiero and J. Ralston, *Journal of Colloid and Interface Science*, **2008**, *323*, 410-419.

71. H. Zhang and A. I. Cooper, *Chemistry of materials*, **2002**, *14*, 4017-4020.

72. H. Zhang, G. C. Hardy, Y. Z. Khimyak, M. J. Rosseinsky and A. I. Cooper, *Chemistry of materials*, **2004**, *16*, 4245-4256.

73. N. C. Grant, A. I. Cooper and H. Zhang, *ACS Applied Materials and Interfaces*, **2010**, *2*, 1400-1406.

74. R. Butler, I. Hopkinson and A. I. Cooper, *Journal of the American Chemical Society*, **2003**, *125*, 14473-14481.

75. R. Wu, A. Menner and A. Bismarck, *Journal of Polymer Science Part A: Polymer Chemistry*, **2010**, *48*, 1979-1989.

76. S. S. Manley, N. Graeber, Z. Grof, A. Menner, G. F. Hewitt, F. Stepanek and A. Bismarck, *Soft Matter*, **2009**, *5*, 4780-4787.

77. D. Barby, Haq, Z., *Europe Pat.*, **1982**.

78. K. Kim, Bismarck, A., *eXPRESS Polymer Letters*, **2010**, *4*, 196.

79. A. Menner and A. Bismarck, *Macromolecular Symposia*, **2006**, *242*, 19-24.

80. N. Cameron and D. Sherrington, in *Biopolymers Liquid Crystalline Polymers Phase Emulsion*, Springer Berlin / Heidelberg, **1996**, vol. 126, pp. 163-214.

81. J. M. Williams, *Langmuir*, **1991**, *7*, 1370-1377.

82. J. M. Williams, A. J. Gray and M. H. Wilkerson, *Langmuir*, **1990**, *6*, 437-444.

83. J. M. Williams and D. A. Wrobleski, *Langmuir*, **1988**, *4*, 656-662.

84. A. Imhof and D. J. Pine, *Nature*, **1997**, *389*, 948-951.

85. P. Colver, *Chemistry of materials*, **2007**, *19*, 1537-1539.

86. Y. Zhu, S. Zhang, Y. Hua, J. Chen and C. P. Hu, *Polymer*, **2010**, *51*, 3612-3617.

87. S. Zhang, Y. Zhu, Y. Hua, C. Jegat, J. Chen and M. Taha, *Polymer*, **2011**, *52*, 4881-4890.

88. A. Vílchez, C. Rodríguez-Abreu, J. Esquena, A. Menner and A. Bismarck, *Langmuir*, **2011**, *27*, 13342-13352.

89. E. H. Mert, H. Yıldırım, A. T. Üzümcü and H. Kavas, *Reactive and Functional Polymers*, **2013**, *73*, 175-181.

90. H. Zhang and A. I. Cooper, *Industrial and Engineering Chemistry Research*, **2005**, *44*, 8707-8714.

91. Z. Li, X. Wei, T. Ming, J. Wang and T. Ngai, *Chemical Communications*, **2010**, *46*, 8767-8769.

92. A. F. Gross and A. P. Nowak, *Langmuir*, **2010**, *26*, 11378-11383.

93. F. Carn, A. Colin, M. F. Achard, H. Deleuze, E. Sellier, M. Birot and R. Backov, *Journal of Materials Chemistry*, **2004**, *14*, 1370-1376.

94. M. G. Schwab, I. Senkovska, M. Rose, M. Koch, J. Pahnke, G. Jonschker and S. Kaskel, *Advanced Engineering Materials*, **2008**, *10*, 1151-1155.

95. K.-Y. Lee, Wong, L.L.C., Blaker, J.J., Hodgkinson, J., Bismarck, A., *Green Chemistry*, **2011**, *13*, 3117-3123.

96. B. G. Barron and J. R. Dunlap, *United States Pat.*, Patent 3821130, **1973**.

97. A. Evans, J. Edward and A. J. Harris, WO 98/42775, **2000**.

98. Q. Cai, J. Yang, J. Bei and S. Wang, *Biomaterials*, **2002**, *23*, 4483-4492.

99. V. Kumar and N. P. Suh, *Polymer Engineering and Science*, **1990**, *30*, 1323-1329.

100. S. K. Goel and E. J. Beckman, *Polymer Engineering and Science*, **1994**, *34*, 1137-1147.

101. A. I. Cooper, *Journal of Materials Chemistry*, **2000**, *10*, 207-234.

102. F. Carn, A. Colin, M.-F. Achard, H. Deleuze, E. Sellier, M. Birot and R. Backov, *Journal of Materials Chemistry*, **2004**, *14*, 1370-1376.

103. H. Zhang, G. C. Hardy, M. J. Rosseinsky and A. I. Cooper, *Advanced Materials*, **2003**, *15*, 78-81.

104. A. Mercier, H. Deleuze and O. Mondain-Monval, *Reactive and Functional Polymers*, **2000**, *46*, 67-79.

105. G. Akay, E. Erhan and B. Keskinler, *Biotechnology and Bioengineering*, **2005**, *90*, 180-190.

106. M. Ottens, G. Leene, A. A. C. M. Beenackers, N. Cameron and D. C. Sherrington, *Industrial and Engineering Chemistry Research*, **2000**, *39*, 259-266.

107. Z. Bhumgara, *Filtration and Separation*, **1995**, *32*, 245-251.

108. W. Busby, N. R. Cameron and C. A. B. Jahoda, *Biomacromolecules*, **2001**, *2*, 154-164.

109. N. Shirshova and A. Bismarck, *Cement and Concrete Composites*, **2012**, *34*, 337-341.

110. N. Shirshova, A. Menner, G. P. Funkhouser and A. Bismarck, *Cement and Concrete Research*, **2011**, *41*, 443-450.

111. J. Blaker, K.-Y. Lee, X. Li, A. Menner and A. Bismarck, *Green Chemistry*, **2009**, *11*, 1321-1326.

112. A. Menner, R. Verdejo, M. Shaffer and A. Bismarck, *Langmuir*, **2007**, *23*, 2398-2403.

113. L. L. C. Wong, V.O. Ikem, A. Menner, A. Bismarck, *Macromolecular Rapid Communications*, **2011**, *32*, 1563-1568.

114. N. R. Cameron, D. C. Sherrington, L. Albiston and D. P. Gregory, *Colloid and Polymer Science*, **1996**, *274*, 592-595.

115. N. R. Cameron, *Polymer*, **2005**, *46*, 1439-1449.

116. P. Hainey, I. M. Huxham, B. Rowatt, D. C. Sherrington and L. Tetley, *Macromolecules*, **1991**, *24*, 117-121.

117. Y. Luo, A.-N. Wang and X. Gao, *Soft Matter*, **2012**, *8*, 1824-1830.

118. A. Menner, K. Haibach, R. Powell and A. Bismarck, *Polymer*, **2006**, *47*, 7628-7635.

119. K. Haibach, A. Menner, R. Powell and A. Bismarck, *Polymer*, **2006**, *47*, 4513-4519.

120. A. Menner, M. Salgueiro, M. S. P. Shaffer and A. Bismarck, *Journal of Polymer Science Part A: Polymer Chemistry*, **2008**, *46*, 5708-5714.

121. O. Lépine, M. Birot and H. Deleuze, *Journal of Polymer Science Part A: Polymer Chemistry*, **2007**, *45*, 4193-4203.

122. C. Youssef, R. Backov, M. Treguer, M. Birot and H. Deleuze, *Journal of Polymer Science Part A: Polymer Chemistry*, **2010**, *48*, 2942-2947.

123. S. Kovacic, K. Jerabek, P. Krajnc and C. Slugovc, *Polym. Chem.*, **2012**, *3*, 325-328.

124. G. S. Berman, *Structural Steel Design and Construction*, Greyhawk North America L.L.C., USA, **2011**.

125. J. P. Queslel and J. E. Mark, *Elasticity, Rubber-like*, John Wiley & Sons, Inc., **2002**.

126. J. A. Rinde, *Journal of Applied Polymer Science*, **1970**, *14*, 1913-1926.

127. M. F. A. L.J. Gibson, *Cellular Solids: Structure and Properties*, Cambridge University Press, **1999**.

128. M. Hartmann, *Angewandte Chemie International Edition*, **2004**, *43*, 5880-5882.

129. N. R. Cameron, D. C. Sherrington, L. Albiston and D. P. Gregory, *Colloid & Polymer Science*, **1996**, *274*, 592-595.

130. A. Menner, R. Powell and A. Bismarck, *Macromolecules*, **2006**, *39*, 2034-2035.

131. S. Arditty, C. P. Whitby, B. P. Binks, V. Schmitt and F. Leal-Calderon, *European Physical Journal E*, **2003**, *11*, 273-281.

132. M. Mihai, M. A. Huneault, B. D. Favis and H. Li, *Macromolecular Bioscience*, **2007**, *7*, 869-869.

133. J. J. Blaker, J. C. Knowles and R. M. Day, *Acta Biomaterialia*, **2008**, *4*, 264-272.

134. Y. S. Nam and T. G. Park, *Journal of biomedical materials research*, **1999**, *47*, 8-17.

135. J. J. Blaker, V. Maquet, R. Jérôme, A. R. Boccaccini and S. N. Nazhat, *Acta Biomaterialia*, **2005**, *1*, 643-652.

136. H. Ma, J. Hu and P. X. Ma, *Advanced Functional Materials*, **2010**, *20*, 2833-2841.

137. K. A. Arora, A. J. Lesser and T. J. MacCathy, *Macromolecules*, **1998**, *31*, 4614-4620.

138. S. P. Nalawade, F. Picchioni and L. Janssen, *Progress in Polymer Science*, **2006**, *31*, 19-43.

139. K. Unger, *Angewandte Chemie, International Edition in English*, **1972**, *11*, 267-278.

140. C. A. Steeves and N. A. Fleck, *International Journal of Mechanical Sciences*, **2004**, *46*, 585-608.

141. B. P. Binks and T. S. Horozov, *Colloidal Particles at Liquid Interfaces*, Cambridge University Press, **2006**.

142. J. M. Raquez, M. Deléglise, M. F. Lacrampe and P. Krawczak, *Progress in Polymer Science*, **2010**, *35*, 487-509.

143. G. Scott, *Polymer Degradation and Stability*, **2000**, *68*, 1-7.

144. G. Swift, *Accounts of Chemical Research*, **1993**, *26*, 105-110.

145. I. V. Steinberg, US 3450613, **1964**.

146. C. S. Nevin, US 3125592, **1964**.

147. K.-Y. Lee, K. K. C. Ho, K. Schlufter and A. Bismarck, *Composites Science and Technology*, **2012**, *72*, 1479-1486.

148. A. Guo, I. Javni and Z. Petrovic, *Journal of Applied Polymer Science*, **2000**, *77*, 467-473.

149. Z. S. Petrović, *Polymer Reviews*, **2008**, *48*, 109-155.

150. L. M. Bonnaillie and R. P. Wool, *Journal of Applied Polymer Science*, **2007**, *105*, 1042-1052.

151. K.-Y. Lee, Wong, L.L.C., Blaker, J.J., Hodgkinson, J., Bismarck, A., *Green Chemistry*, **2011**.

152. F. Svec and J. Frechet, *Science*, **1996**, *273*, 205.

153. A. Cervantes Martinez, E. Rio, G. Delon, A. Saint-Jalmes, D. Langevin and B. P. Binks, *Soft Matter*, **2008**, *4*, 1531-1535.

154. B. P. Binks and T. S. Horozov, *Angewandte Chemie International Edition*, **2005**, *44*, 3722-3725.

155. B. S. Murray, A. Cox, E. Dickinson, P. V. Nelson and Y. Wang, in *Food Colloids: Self-Assembly and Material Science*, The Royal Society of Chemistry, **2007**, pp. 369-382.

156. B. S. Murray, *Current Opinion in Colloid and Interface Science*, **2007**, *12*, 232-241.

157. D. Behera and A. K. Banthia, *Journal of Applied Polymer Science*, **2008**, *109*, 2583-2590.

158. A. K. Geim and K. S. Novoselov, *Nature Materials*, **2007**, *6*, 183-191.

159. K. S. Novoselov, A. K. Geim, S. V. Morozov, D. Jiang, Y. Zhang, S. V. Dubonos, I. V. Grigorieva and A. A. Firsov, *Science*, **2004**, *306*, 666-669.

160. X. Wang, L. Zhi and K. Mullen, *Nano Letters*, **2007**, *8*, 323-327.

161. S. Stankovich, D. A. Dikin, G. H. B. Dommett, K. M. Kohlhaas, E. J. Zimney, E. A. Stach, R. D. Piner, S. T. Nguyen and R. S. Ruoff, *Nature*, **2006**, *442*, 282-286.

162. S. Ghosh, I. Calizo, D. Teweldebrhan, E. P. Pokatilov, D. L. Nika, A. A. Balandin, W. Bao, F. Miao and C. N. Lau, *Applied Physics Letters*, **2008**, *92*.

163. C. Gómez-Navarro, R. T. Weitz, A. M. Bittner, M. Scolari, A. Mews, M. Burghard and K. Kern, *Nano Letters*, **2007**, *7*, 3499-3503.

164. G. Eda, G. Fanchini and M. Chhowalla, *Nature Nano*, **2008**, *3*, 270-274.

165. S. Stankovich, D. A. Dikin, R. D. Piner, K. A. Kohlhaas, A. Kleinhammes, Y. Jia, Y. Wu, S. T. Nguyen and R. S. Ruoff, *Carbon*, **2007**, *45*, 1558-1565.

166. C. Mattevi, G. Eda, S. Agnoli, S. Miller, K. A. Mkhoyan, O. Celik, D. Mastrogiovanni, G. Granozzi, E. Garfunkel and M. Chhowalla, *Advanced Functional Materials*, **2009**, *19*, 2577-2583.

167. A. Bagri, C. Mattevi, M. Acik, Y. J. Chabal, M. Chhowalla and V. B. Shenoy, *Nature Chemistry*, **2010**, *2*, 581-587.

168. H. Wang, L.-F. Cui, Y. Yang, H. Sanchez Casalongue, J. T. Robinson, Y. Liang, Y. Cui and H. Dai, *Journal of the American Chemical Society*, **2010**, *132*, 13978-13980.

169. Y. Li, H. Wang, L. Xie, Y. Liang, G. Hong and H. Dai, *Journal of the American Chemical Society*, **2011**, *133*, 7296-7299.

170. J. Liang, Y. Huang, L. Zhang, Y. Wang, Y. Ma, T. Guo and Y. Chen, *Advanced Functional Materials*, **2009**, *19*, 2297-2302.

171. G. Vleminckx, S. Bose, J. Leys, J. Vermant, M. Wübbenhorst, A. A. Abdala, C. Macosko and P. Moldenaers, *ACS Applied Materials and Interfaces*, **2011**, *3*, 3172-3180.

172. L. J. Cote, J. Kim, V. C. Tung, J. Y. Luo, F. Kim and J. X. Huang, *Pure and Applied Chemistry*, **2011**, *83*, 95-110.

173. F. Kim, L. J. Cote and J. X. Huang, *Advanced Materials*, **2010**, *22*, 1954-1958.

174. X. Song, Y. Yang, J. Liu and H. Zhao, *Langmuir*, **2010**, *27*, 1186-1191.

175. M. M. Gudarzi and F. Sharif, *Soft Matter*, **2011**, *7*, 3432-3440.

176. H. Kim, A. A. Abdala and C. W. Macosko, *Macromolecules*, **2010**, *43*, 6515-6530.

177. RamanathanT, A. A. Abdala, StankovichS, D. A. Dikin, M. Herrera Alonso, R. D. Piner, D. H. Adamson, H. C. Schniepp, ChenX, R. S. Ruoff, S. T. Nguyen, I. A. Aksay, R. K. Prud'Homme and L. C. Brinson, *Nature Nano*, **2008**, *3*, 327-331.

178. Y. Xu, W. Hong, H. Bai, C. Li and G. Shi, *Carbon*, **2009**, *47*, 3538-3543.

179. M. Steenackers, A. M. Gigler, N. Zhang, F. Deubel, M. Seifert, L. H. Hess, C. H. Y. X. Lim, K. P. Loh, J. A. Garrido, R. Jordan, M. Stutzmann and I. D. Sharp, *Journal of the American Chemical Society*, **2011**, *133*, 10490-10498.

180. I. Aranberri, B. Binks, J. Clint and P. Fletcher, *Journal of Porous Materials*, **2009**, *16*, 429-437.

181. S. Barg, E. G. de Moraes, D. Koch and G. Grathwohl, *Journal of the European Ceramic Society*, **2009**, *29*, 2439-2446.

182. I. Akartuna, A. R. Studart, E. Tervoort and L. J. Gauckler, *Advanced Materials*, **2008**, *20*, 4714.

183. S. Barg, M. D. M. Innocentini, R. V. Meloni, W. S. Chacon, H. Wang, D. Koch and G. Grathwohl, *Journal of Membrane Science*, **2011**, *383*, 35-43.

184. S. Barg, B. Binks, H. Wang, D. Koch and G. Grathwohl, *Journal of Porous Materials*, **2012**, *19*, 859-867.

185. A. Menner, R. Verdejo, M. Shaffer and A. Bismarck, *Langmuir*, **2007**, *23*, 2398-2403.

186. R. T. Wu, A. Menner and A. Bismarck, *Journal of Polymer Science Part a-Polymer Chemistry*, **2010**, *48*, 1979-1989.

187. A. Menner, V. Ikem, M. Salgueiro, M. S. P. Shaffer and A. Bismarck, *Chemical Communications*, **2007**, 4274-4276.

188. A. Vilchez, C. Rodriguez-Abreu, J. Esquena, A. Menner and A. Bismarck, *Langmuir*, **2011**, *27*, 13342-13352.

189. L. L. C. Wong, V. O. Ikem, A. Menner and A. Bismarck, *Macromolecular Rapid Communications*, **2011**, *32*, 1563-1568.

190. V. O. Ikem, A. Menner and A. Bismarck, *Soft Matter*, **2011**, *7*, 6571-6577.

191. H.-B. Zhang, Q. Yan, W.-G. Zheng, Z. He and Z.-Z. Yu, *ACS Applied Materials and Interfaces*, **2011**, *3*, 918-924.

192. Z. P. Chen, W. C. Ren, L. B. Gao, B. L. Liu, S. F. Pei and H. M. Cheng, *Nature Materials*, **2011**, *10*, 424-428.

193. R. Verdejo, F. Barroso-Bujans, M. A. Rodriguez-Perez, J. Antonio de Saja and M. A. Lopez-Manchado, *Journal of Materials Chemistry*, **2008**, *18*, 2221-2226.

194. J. L. Vickery, A. J. Patil and S. Mann, *Advanced Materials*, **2009**, *21*, 2180-2184.

195. N. R. Cameron and A. Barbetta, *Journal of Materials Chemistry*, **2000**, *10*, 2466-2471.

196. A. R. Studart, U. T. Gonzenbach, E. Tervoort and L. J. Gauckler, *Journal of the American Ceramic Society*, **2006** *89*, 1771-1789.

197. B. P. Binks, *Current opinion in colloid & interface science*, **2002**, *7*, 21-41.

198. Y. L. Yang and M. C. Gupta, *Nano Letters*, **2005**, *5*, 2131-2134.

199. M. Claire Hermant, B. Klumperman and C. E. Koning, *Chemical Communications*, **2009**, 2738-2740.

200. M. Hirata, T. Gotou, S. Horiuchi, M. Fujiwara and M. Ohba, *Carbon*, **2004**, *42*, 2929-2937.

201. L. L. C. Wong, P. B. Villafranca, A. Menner and A. Bismarck, *Submitted manuscript*, **2013**.

202. D. S. McLachlan, C. Chiteme, C. Park, K. E. Wise, S. E. Lowther, P. T. Lillehei, E. J. Siochi and J. S. Harrison, *Journal of Polymer Science Part B: Polymer Physics*, **2005**, *43*, 3273-3287.

203. F. Yavari, Z. Chen, A. V. Thomas, W. Ren, H.-M. Cheng and N. Koratkar, *Surface Science Reports*, **2011**, *1*.

204. D. Wan, C. Yang, T. Lin, Y. Tang, M. Zhou, Y. Zhong, F. Huang and J. Lin, *ACS Nano*, **2012**.

205. H. Wang, Y. Liang, T. Mirfakhrai, Z. Chen, H. Casalongue and H. Dai, *Nano Research*, **2011**, *4*, 729-736.

206. O. N. Ruiz, K. A. S. Fernando, B. Wang, N. A. Brown, P. G. Luo, N. D. McNamara, M. Vangsness, Y.-P. Sun and C. E. Bunker, *ACS Nano*, **2011**, *5*, 8100-8107.

Appendices

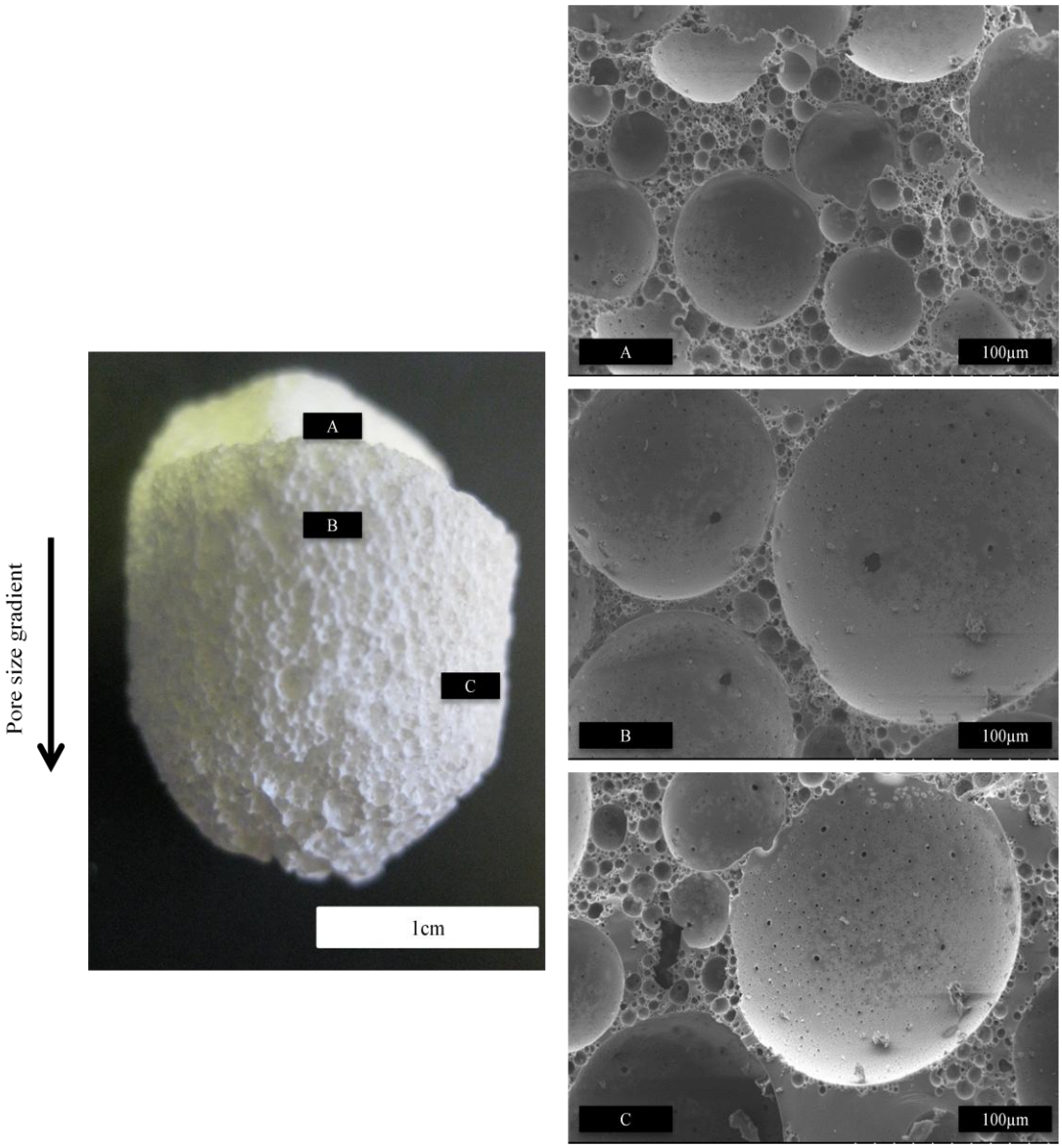

Figure A0-1: Left: Macroporous polymer prepared using 0.75 w/vol.% surfactant stabilised emulsion template with pore size gradient. Right: SEM showing different pore size distributions taken from corresponding areas of the macroporous polymer sample on the left, a result of sedimentation at the low surfactant concentration of 0.75 w/vol.%.

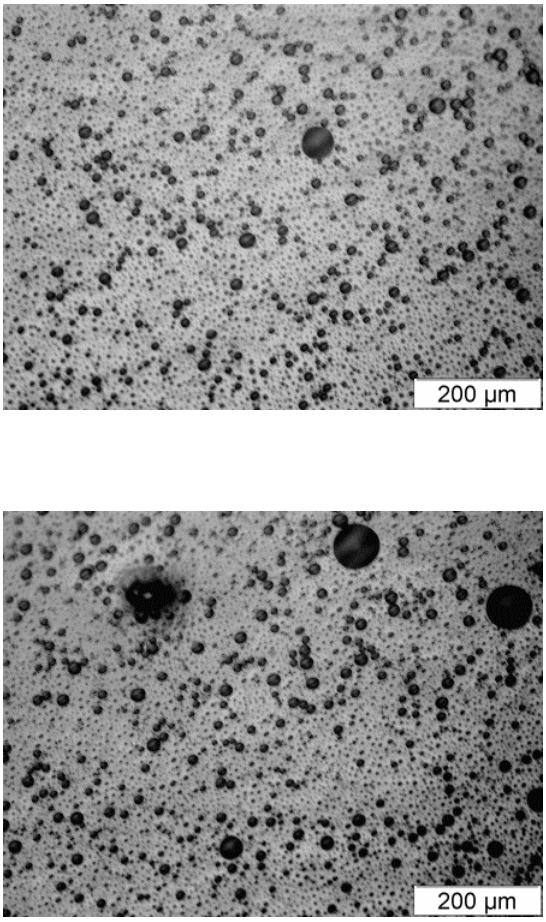

Figure A0-2: Optical micrograph of HIPE used to prepare DS5 (5 w/vol.% surfactant) fresh after emulsification (top) and a day later (bottom). The negligible change in droplet size in the emulsion after a day showed that the effects of droplet coalescence on the final hierarchical structure were small.

Table A0-1: Table summarising fitting parameters for pore throat distribution curves (Figure 3-6)

Sample	ω	A
DS1	0.42 ± 0.04	28.2 ± 1.6
DS2	0.38 ± 0.02	33.8 ± 2.3
DS5	0.38 ± 0.03	34.5 ± 1.9
DS10	0.25 ± 0.02	27.6 ± 2.5
DS20	0.27 ± 0.02	36.0 ± 1.6

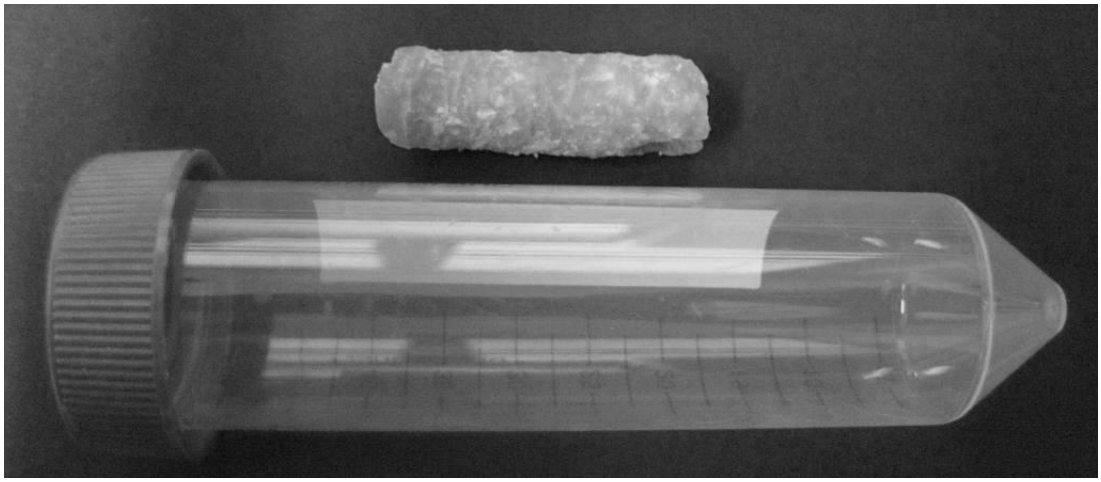

Figure A0-3: Image of control sample 0 (above) after drying using convection oven in relation to the size of the Falcon tube (below) used for polymerisation.

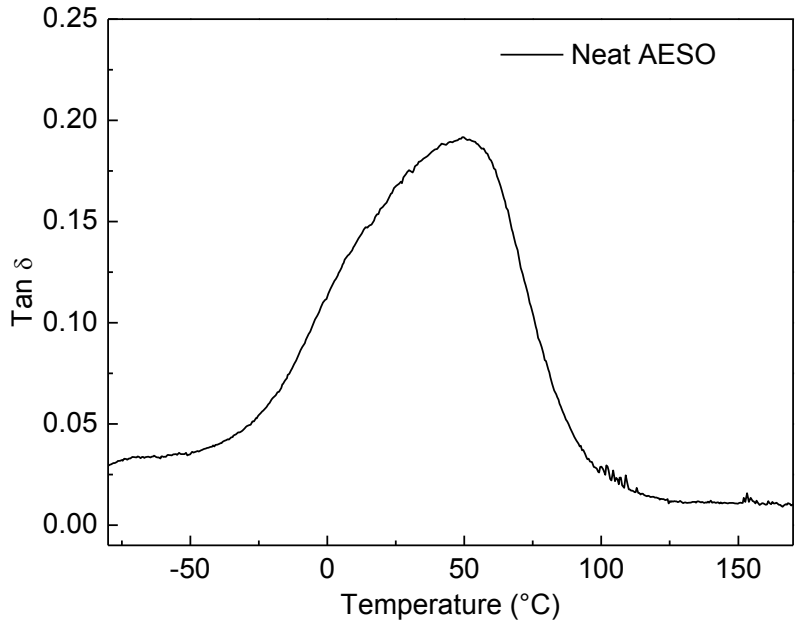

Figure A0-4: DMTA profile of pure polyAESO (bulk) showing a peak in tan δ at approximately 50°C

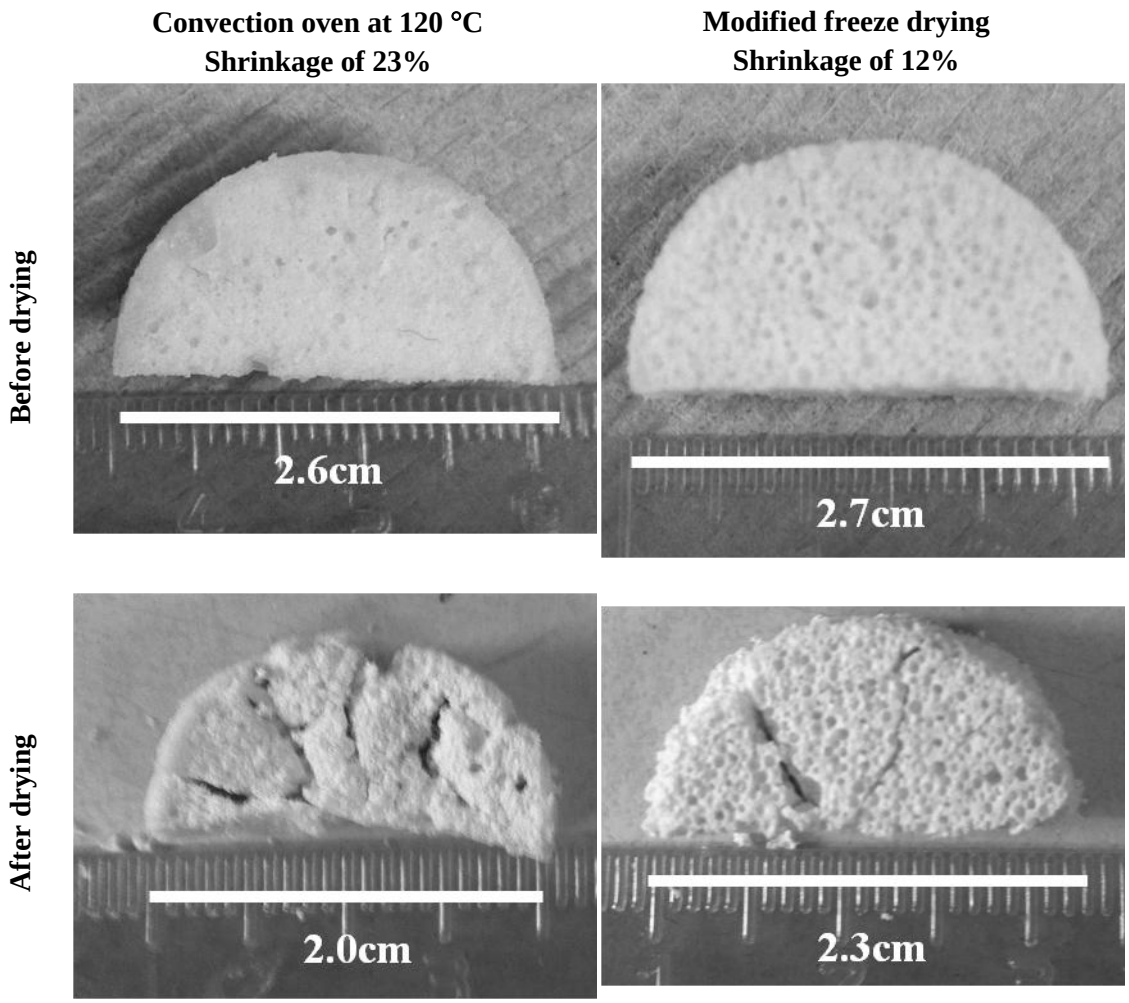

Figure A0-5: Photos of A3 before and after drying using convection oven (left top and bottom) v.s. modified freeze drying (right top and bottom). Shrinkage is halved and cracking is reduced by using a different drying protocol.

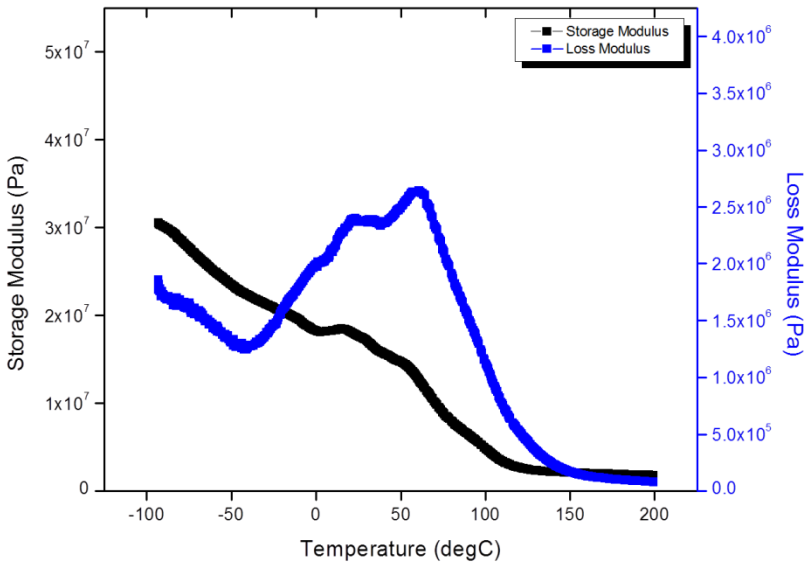
Storage Modulus
Loss Modulus
Storage Modulus (Pa)
Loss Modulus (Pa)
Temperature (degC)
5x10^7
4x10^7
3x10^7
2x10^7
1x10^7
0
4.0x10^6
3.5x10^6
3.0x10^6
2.5x10^6
2.0x10^6
1.5x10^6
1.0x10^6
5.0x10^5
0.0
-100
-50
0
50
100
150
200

A1

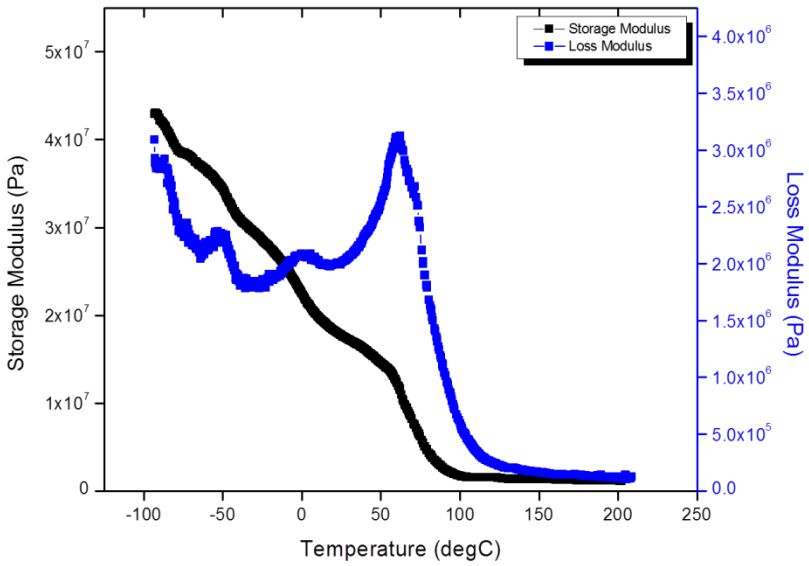
Storage Modulus
Loss Modulus
Storage Modulus (Pa)
Loss Modulus (Pa)
Temperature (degC)
5x10^7
4x10^7
3x10^7
2x10^7
1x10^7
0
4.0x10^6
3.5x10^6
3.0x10^6
2.5x10^6
2.0x10^6
1.5x10^6
1.0x10^6
5.0x10^5
0.0
-100
-50
0
50
100
150
200
250

A2

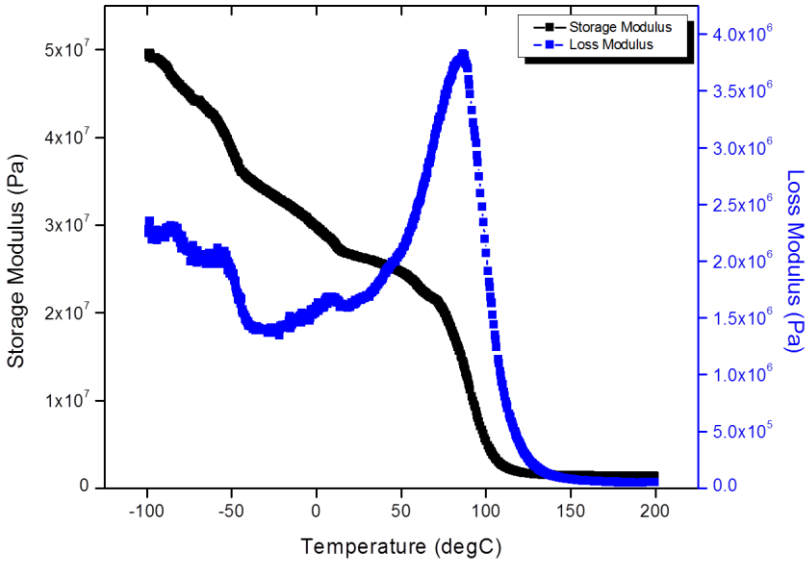

A3

Figure A0-6: Representative curves of the Dynamic Mechanical behaviour (Storage modulus and Tan Delta vs T) of A1 (top) to A3 (bottom) with respect to increasing temperature, subjected to constant frequency oscillations.